

N 62 54560

3

CASE FILE

COPY

CASE FILE

COPY

NATIONAL ADVISORY COMMITTEE
FOR AERONAUTICS

NACA TN 2560

TECHNICAL NOTE 2560

AN EXPERIMENTAL INVESTIGATION OF TRANSONIC FLOW PAST
TWO-DIMENSIONAL WEDGE AND CIRCULAR-ARC SECTIONS
USING A MACH-ZEHNDER INTERFEROMETER

By Arthur Earl Bryson, Jr.

California Institute of Technology



Washington

November 1951

NASA FILE COPY

loan expires on last
date stamped on back cover.
PLEASE RETURN TO

DIVISION OF RESEARCH INFORMATION
NATIONAL AERONAUTICS
AND SPACE ADMINISTRATION

Washington 25, D. C.

1

NATIONAL ADVISORY COMMITTEE FOR AERONAUTICS

TECHNICAL NOTE 2560

AN EXPERIMENTAL INVESTIGATION OF TRANSONIC FLOW PAST
TWO-DIMENSIONAL WEDGE AND CIRCULAR-ARC SECTIONS
USING A MACH-ZEHNDER INTERFEROMETER

By Arthur Earl Bryson, Jr.

SUMMARY

Interferometer measurements are given of the flow fields near two-dimensional wedge and circular-arc sections at zero angle of attack at high-subsonic and low-supersonic velocities. Both subsonic flow with local supersonic zone and supersonic flow with detached shock wave have been investigated. Pressure distributions and drag coefficients as functions of Mach number have been obtained. The wedge data are compared with the theoretical work on flow past wedge sections of Guderley and Yoshihara, Vincenti and Wagoner, and Cole.

It is shown that the local Mach number at any point on the surface of a finite three-dimensional body or an unswept two-dimensional body, moving through an infinite fluid, has a stationary value at Mach number 1 and, in fact, remains nearly constant for a range of speeds below and above Mach number 1. On the basis of this concept and the experimental data, pressure distributions and drag coefficients for the wedge and circular-arc sections are presented throughout the entire transonic range of velocities.

INTRODUCTION

Difficulties of Theory and Experiment in Transonic

Range of Velocities

The difficulties inherent in studying transonic flow are well-known. Theoretical analysis is made difficult by the nonlinearity of the differential equations of compressible fluid motion. This nonlinearity leads to a change-over in type of the differential equations from elliptic to hyperbolic when transition is made from subsonic to supersonic speeds. Since the essential feature of transonic flow is this mixed

subsonic-supersonic character, it is obvious that no linearization of the differential equations (at least in the physical plane) can adequately describe the flow.

Wind-tunnel studies in the transonic range are made difficult by the large lateral extent of the perturbation flow field around bodies in this range. This means that models which are small compared with the test section must be used. Even then there is still a range of speeds from just below $M_\infty = 1$ to just above $M_\infty = 1$ where the model and/or its support configuration are "choked," that is, where local supersonic zones embedded in the subsonic field extend from the model to the tunnel walls, or, in the supersonic case, where embedded subsonic zones extend to the tunnel walls, or shock waves, reflected from the walls, impinge on the model. Some progress has been made recently in modifying wind-tunnel test sections so as to minimize these effects, but, on the whole, the majority of good test data in the range very close to $M_\infty = 1$ has so far come from free-flight tests. Some good transonic data are available, however, from transonic-bump tests made in wind tunnels (reference 1). Using small models usually results in low Reynolds numbers so that difficulty is often experienced in extrapolating data to full-size Reynolds numbers; this seems to be particularly true of the transonic speed range since the effects of boundary-layer and shock-wave interactions seem to be quite large there (references 2 and 3).

In this paper it is shown that in many instances tests need not be made in the region very close to $M_\infty = 1$ since the flow in this range can be inferred from testing below and above this range and using an interpolation based on the fact that the local Mach number at any point on the surface of unswept two-dimensional bodies and finite three-dimensional bodies has a stationary value at $M_\infty = 1$.

Existence of Potential Transonic Flows

Guderley (reference 4) has made a detailed investigation of the possibility of smooth transonic flows (i.e., subsonic flows with an embedded supersonic zone in which no shock waves appear). He proposes that such smooth flows are exceptional, that they are discrete cases occurring for only particular body shapes at particular free-stream Mach numbers. Any perturbation of the shape with the Mach number held constant (or vice versa), Guderley claims, would result in a shock appearing in the flow. This bears an analogy to the well-known Busemann supersonic biplane which theoretically has no shocks (and hence no drag) at a discrete value of free-stream Mach number and angle of attack (reference 5, p. 154). Guderley's proposal is still controversial (e.g., see the paper of Sears who has made a critical survey of the work to date on the existence of transonic potential flows (reference 6)).

It is obvious that the potential flow must break down for a given body shape at some Mach number less than 1. The argument whether this breakdown occurs precisely when a supersonic region first appears on the body or at a slightly higher Mach number seems somewhat academic (although very interesting), since it is well-known experimentally that the drag-rise Mach number (i.e., the Mach number where noticeable shocks first appear) is very close to the critical Mach number (i.e., the Mach number at which sonic velocity first appears on the body) for most bodies without surface slope discontinuities.

Kuo (reference 7) proposes that supersonic compression is unstable to disturbances; that is, a supersonic region on a body in subsonic flow must end in a shock with no compression occurring in the supersonic flow ahead of the shock. There seems to be ample experimental evidence to show that this is not strictly true since, for example, the compression region of a λ -shock is clearly supersonic. However, the λ -shock configuration is believed to be a phenomenon associated with laminar-boundary-layer and shock-wave interaction; with turbulent boundary layer (a condition more closely approaching nonviscous flow) hardly any noticeable supersonic compression occurs before the shock ending the supersonic zone (see reference 8).

Choice of Models

Two-dimensional flow is much simpler to handle than axially symmetric flow both in theoretical work and in interferometry. Hence it was decided to study two-dimensional flows despite the well-known difficulties in approximating two-dimensional flow in a wind tunnel.

Because of the considerations mentioned previously it was decided to test very small models which would be of such a shape that viscous influences would not materially affect the flow over them. This led to the choice of half airfoils - wedges and circular-arc sections followed by straight sections. These models have favorable pressure gradients on their surfaces over most of the transonic range so that boundary-layer separation, if it does occur, will only occur because of shock-wave influence. Furthermore, such separation will occur downstream of the part of the body being studied and hence will not affect the measurements. Certain viscous effects will still be evident, however, for instance, the effective rounding off of the shoulders and leading edges of the wedge models.

Both theoretical advantages and practical need make the study of thin sections desirable. Consequently the semiwedge angles chosen were $4\frac{1}{2}^{\circ}$, $7\frac{1}{2}^{\circ}$, and 10° (a 26.6° wedge was also used in order to make a comparison with some available theoretical work on a wedge of this

angle). The circular-arc section chosen was essentially the front half of an 8.8-percent-thick biconvex circular-arc airfoil, followed by a straight section. Models of sections much thinner than this, with the same chord lengths used, run into structural difficulties and also the ratio of boundary-layer thickness to model thickness becomes large enough to cause considerable deviation from nonviscous flow.

Transonic-Flow Theory and Experiments

The investigations of Von Kármán, Busemann, Guderley, Frankl, and many others have contributed significantly to methods of approach which can be used to study transonic flow (references 9 to 14). The detailed numerical calculations for specific cases made by Maccoll and Codd, Emmons, Drougge, Drebinger, Guderley and Yoshihara, and Vincenti and Wagoner (references 15 to 21) have helped to dispel the idea of a "sonic barrier." Recently Cole at GALCIT has given an analysis of the flow past wedge sections at high-subsonic speeds (reference 22). By combining the results of Guderley and Yoshihara's, Vincenti and Wagoner's, and Cole's calculations, the flow past thin wedge sections can be given completely through the transonic range permitting a comparison with the present experiments. Some of the investigations mentioned above will be discussed in more detail further on in the present paper.

Available experiments in the transonic range on thin wedge sections are surprisingly few. Pack (reference 23) describes some interferometric experiments on 10° and 20° semiangle wedges made at Braunschweig. His subsonic data appear to be good but the flow in the supersonic interferograms appears to be very nonuniform and not very closely two-dimensional; only one supersonic Mach number was tested where detached shocks occurred. His conclusion that the p/p_∞ distributions on the surface of the 20° semiangle wedge are very much the same for $M_\infty = 0.803$ and $M_\infty = 1.40$ is interesting, but the statement that this agrees with the theoretical predictions of Maccoll and Codd is incorrect since they indicated that the p/p_0 distributions would be nearly the same.

Griffith at Princeton has just recently published the results of some very carefully done experiments on flow past wedge sections of semiangles of 7° , 10° , 20° , 30° , 45° , and 90° (and several other shapes) with detached shock waves (reference 24). These experiments were done in a shock tube and interferograms are presented of the flow fields. The experiments clearly show that the shape of the detached shock and its detachment distance from the sonic point on a wedge depend only on the body thickness and the Mach number (not the wedge angle) when the Mach number is well below the shock-attachment Mach number. This is in general agreement with Busemann's considerations in his paper on detached shock waves (reference 10).

Liepmann, Ashkenas, and Cole (reference 8) made some careful pressure measurements on the surfaces of 6- and 12-percent-thick biconvex circular-arc airfoils at zero angle of attack at high-subsonic speeds in connection with studies of shock-wave and boundary-layer interaction. Some of the results of their tests are combined here with corresponding low-supersonic test results from the present investigation to indicate the behavior of the pressure distribution on circular-arc airfoils at zero angle of attack through the entire transonic range.

Acknowledgment

While the present experimental investigation was in progress, a parallel theoretical study was being carried out by Mr. Walter G. Vincenti at the Ames Aeronautical Laboratory of the NACA. As pointed out in the introduction of reference 21, the two investigations were undertaken independently but the direct relationship of their subject matter made it desirable that they be reported similarly and it was therefore planned to present the results of both studies in a series of coordinated papers to be published by the NACA under a common general title. It has been decided, however, that the general title, "Transonic Flow past a Wedge Profile with Detached Bow Wave," does not completely describe the present report since high-subsonic-speed flows as well as low-supersonic-speed flows with detached bow wave were investigated and a circular-arc profile was tested as well as a wedge profile.

This work was conducted at the California Institute of Technology under the sponsorship and with the financial assistance of the National Advisory Committee for Aeronautics. Grateful acknowledgment is made to Dr. Hans Wolfgang Liepmann who supervised the research, to the members of the GALTIT Transonic Research Group, to Mr. Walter G. Vincenti of the NACA, and to Dr. J. D. Cole of GALTIT for helpful discussions and assistance in carrying out the experimental work. Some of the results of these experiments have already been reported in reference 25.

SYMBOLS

a	sound velocity
c	airfoil chord
C_D	pressure drag coefficient
\tilde{C}_D	reduced drag coefficient $\left(\frac{(\gamma + 1)^{1/3} C_D}{(t/c)^{5/3}} \right)$

C_p	pressure coefficient
\tilde{C}_p	reduced pressure coefficient $\left(\frac{(\gamma + 1)^{1/3} C_p}{(t/c)^{2/3}} \right)$
k	Gladstone-Dale constant
l	model span
M	Mach number
n	index of refraction
p	pressure
q	dynamic pressure
t/c	airfoil thickness ratio
u	horizontal component perturbation velocity (perturbation from a^*)
v	vertical component perturbation velocity
x, y	Cartesian coordinates, origin at leading edge of profile
\tilde{y}	reduced vertical distance $\left(\left[(\gamma + 1) t/c \right]^{1/3} y \right)$
α	angle of attack
γ	ratio of specific heats (1.4 for air)
θ	semiwedge angle
λ	wave length of monochromatic light used on interferometer
ξ	reduced Mach number
ρ	density

Subscripts and superscripts:

$()_\infty$	conditions in free stream
$()_0$	reservoir conditions

- ()_o reservoir conditions behind a shock wave
()^{*} conditions at sonic velocity

Symbols used without subscripts indicate local conditions.

APPARATUS AND METHODS

Wind Tunnel

The measurements were made in the GALCIT 4- by 10-inch transonic wind tunnel. For a description of the tunnel and the flexible nozzle employed see reference 26. The tunnel can be run at both subsonic and low-supersonic velocities with continuous Mach number variation through use of the flexible nozzle and a variable second-throat nozzle downstream of the test section.

Models

The models used were "half airfoils" followed by straight sections. Four of the models were wedges (semiangles 4.53° , 7.56° , 10.00° , and 26.57°) followed by straight sections and the fifth was half of a biconvex circular-arc airfoil (8.80 percent thick) followed by a straight section (see fig. 1). The distance from the leading edge to the point where the straight section began was of the order of $1/4$ inch for all five models. The models were made of tool steel and were very carefully machined and lapped so as to give exact cylindrical surfaces. Two pressure orifices on opposite sides of the airfoil were placed exactly the same distance from the leading edge to aid in setting the model to zero angle of attack by balancing these pressures on an alcohol U-tube. Because of the very short chord lengths vernier-protractor measurements of the opening angles of the leading edge were of doubtful accuracy, so the angles were measured by letting the leading edge split a beam of parallel light and measuring the position of the reflected spots on a wall in back of the model. In this manner the angles could be measured to $\pm 0.03^\circ$.

Interferometer

The interferometer used in this investigation is described in references 27 and 28. One of the main features of this interferometer is that both light beams are passed through the test section, one over the model and the other ahead of the model in the uniform flow field, that is, where the velocity is nearly the free-stream velocity. The

advantages of this are: (1) The fringe shifts are in relation to the free-stream density and (2) the effects of the side-wall boundary layers are approximately canceled out since both beams traverse nearly the same boundary layer at each side window. This leads to improved accuracy when the interferograms are evaluated on the basis of the absolute value of the fringe shift from no-flow conditions. For these tests finite-fringe interferograms were used and another method of evaluation was devised which is much simpler and more accurate than the above-mentioned technique. Infinite-fringe interferograms, while they give the constant-density contours immediately, are less accurate than the superimposed finite-fringe interferograms because any optical inaccuracies in the system cause the contour fringes to be distorted. These inaccuracies are calibrated out in the superimposed finite-fringe interferograms. Also there are times when one does not know whether the density increment between contours of an infinite-fringe interferogram is positive or negative; this trouble does not arise with the finite-fringe interferograms. A typical finite-fringe interferogram is shown in figure 2.

Method of Evaluation of Interferograms

The method of evaluation used here depends on two techniques:

- (a) Photographic superposition of disturbed and undisturbed interferograms and
- (b) fringe identification by a pressure measured on the model.

Direct photographic superposition of a "no-flow" finite-fringe interferogram on a "with-flow" finite-fringe interferogram gives rise to dashed shadowy lines (the dashes being where the dark fringes of one picture cross the light fringes of the other); see figure 3 for an example of this type of picture. These shadowy lines can easily be shown to be lines of constant density for two-dimensional flow and are the same contours as would be obtained on an infinite-fringe interferogram made with perfect optical surfaces. The increment in density between these shadowy lines is a constant dependent only on the span of the model and the wave length of the monochromatic light being used. This is easily shown since the difference in optical path lengths of the light rays between two adjacent constant-density contours must be 1 wave length of the light being used. For two-dimensional flow the difference in optical path length will simply be $l \Delta n$, where l is the span of the model and Δn is the difference in index of refraction between the two light paths. Thus

$$l \Delta n = \lambda \quad (1)$$

But the relation between index of refraction and density in a gas is given by

$$n - 1 = kp \quad (2)$$

where k is the Gladstone-Dale constant (a function of the light frequency and type of gas). Therefore

$$\Delta\rho = \frac{\lambda}{k\ell} \quad (3)$$

where $\Delta\rho$ is the difference in density between two adjacent constant-density contours. For these experiments

$$\lambda = 5461 \text{ \AA} \text{ (mercury green line)}$$

$$k = 0.1162 \text{ cubic foot per slug}$$

$$\ell = 3.50 \text{ inches}$$

so

$$\frac{\Delta\rho}{\rho_0} = 0.0250 \text{ per fringe shift}$$

where $\rho_0 = 0.00211$ slugs per cubic foot was the usual tunnel stagnation density.

The advantage of photographic superposition is not only in time saved but also in increased accuracy of evaluation. Any slight changes in fringe spacing or fringe orientation with respect to the "no-flow" interferogram which occur before the "with-flow" interferogram is taken can be almost exactly canceled out by causing the two superimposed interferograms to coincide exactly in a region where it is known that the flow was uniform, since in such regions there should be no isopycnic contours. This is particularly easy to do for supersonic flow if a portion of the flow field ahead of the nose shock wave is included in the interferogram. For subsonic flow care must be taken to include enough of the flow field ahead of the model in the interferogram to have some of the nearly undisturbed flow field for comparison; this was quite simple to do for the small, thin models used in these tests.

The actual superposition technique used here was first to make a print $\left(3\frac{1}{2}$ times enlarged) of the "with-flow" interferogram. This print was then placed under the enlarger and the "no-flow" interferogram negative was put into the enlarger. By changing the enlargement scale and moving the "with-flow" interferogram under the enlarger the fringes were made to coincide exactly in the regions of uniform flow. The constant-density contours could then be drawn in on the print. Alternatively the first print could be made on transparent paper (Anso Reprolith Ortho was used) and when the superposition was accomplished a

piece of photosensitive paper was slipped under the transparent print and a print of the two interferograms was obtained. This was the technique used for figure 3.

In order to identify the density values with the fringes a pressure tap was placed on the model in a region where the pressure gradient was expected to be large. From the pressure reading the density at the pressure tap was calculated using reservoir fluid properties (taking into account entropy changes through shock waves). The pressure tap will always lie between two fringe contours or on a contour, so that, by knowing the density increment between fringe contours, the values of the density on the adjacent contours can be obtained by interpolation. The whole interferogram is determined once the density is known on one contour (except for the shifts through shock waves).

Interferometer Sensitivity

It is interesting to note that the interferometric method has its greatest sensitivity in the transonic range. As pointed out previously, the density increment between two adjacent contour fringes is a constant

$$\Delta\rho = \frac{\lambda}{k\ell}$$

Now in any part of the flow field where the stagnation density is constant along a streamline,

$$\frac{\rho}{\rho_0} = \left(1 + \frac{\gamma - 1}{2} M^2\right)^{-\frac{1}{\gamma-1}} \quad (4)$$

so

$$\frac{d\rho}{\rho_0} = - \left(1 + \frac{\gamma - 1}{2} M^2\right)^{-\frac{\gamma}{\gamma-1}} M dM \quad (5)$$

Hence the increment in Mach number between adjacent contour fringes is given approximately by

$$\Delta M \approx \frac{\left(1 + \frac{\gamma - 1}{2} M^2\right)^{\frac{\gamma}{\gamma-1}}}{M} \frac{\lambda}{k\ell\rho_0} \quad (6)$$

since

$$\frac{\Delta\rho}{\rho_0} = \frac{\lambda}{k\lambda\rho_0}$$

This function has a minimum at $M = \sqrt{\frac{2}{\gamma + 1}}$ which is $M = 0.914$ for air ($\gamma = 1.4$). A graph of this function is shown in figure 4. Note that the Mach number increment per fringe for these tests, was always closely equal to 0.05.

Similarly, the expression for the increment in pressure coefficient between adjacent contour fringes is approximately

$$\Delta C_p \approx \frac{\left(1 + \frac{\gamma - 1}{2} M^2\right)^{-1}}{M_\infty^2 \left(1 + \frac{\gamma - 1}{2} M^2\right)^{\frac{\gamma}{\gamma - 1}}} \frac{\lambda}{k\lambda\rho_0} \quad (7)$$

For values of M close to M_∞ , this expression has a minimum at $M_\infty = \sqrt{\frac{2}{2 - \gamma}}$ which is 1.832 for air.

Side-Wall Boundary-Layer Effect on Approximating Two-Dimensional Flow

A close approximation to two-dimensional flow over the whole span of the model was required since the interferometer integrates the value of the density from wall to wall. In a nonviscous fluid, letting the model extend from wall to wall would theoretically give two-dimensional flow over the whole span. If the model did not span the whole tunnel, the flow would correspond to that past a model of infinite span with periodic gaps in it where the gaps were equal to twice the distance from the edge of the model to the wall. The effect of the side-wall boundary layers, for a model that does not span the tunnel, is roughly to decrease the size of this gap. Approximately, the gap size would be decreased by twice the displacement thickness of the wall boundary layer. By making the gap between the edge of the model and the wall approximately equal to the wall-boundary-layer displacement thickness, one might hope to approximate closely two-dimensional flow over the span. This phenomenon

is, of course, very much more complicated than this, particularly in the supersonic case where the shock waves interact with the wall boundary layer. However, by taking circular-cylinder and wedge models and varying the gap size in increments of $1/16$ inch, it was found that the detached bow wave became closely two-dimensional when the gap size was $1/4$ inch (i.e., there was no blur ahead of or behind the shock pictures) which is almost exactly the boundary-layer displacement thickness when measured without a model in the test section. When the gap was $3/16$ inch the shock was blurred ahead of the main shock and when the gap was $5/16$ inch it was blurred behind the main shock. These tests were further substantiated by some schlieren pictures, which Mr. Walter G. Vincenti of the NACA Ames Aeronautical Laboratory kindly made available, showing a view looking down on a wedge model so that the leading edge of the detached shock appeared as a line; by varying the model span a discrete value of the span was found where this line was almost exactly parallel to the leading edge of the model, while for just slight variations from this gap size the shock was curved forward or backward. Figure 2 shows a finite-fringe interferogram of the circular-arc section with a detached shock where the definition of the shock wave was unusually sharp. This is strong, but of course not conclusive, evidence that the flow was closely two-dimensional over most of the span. Further evidence that the flow differed from two-dimensional flow only slightly is given in the next section.

Side-Wall Boundary-Layer Effect on Interferogram Evaluations

A result of the method of interferogram evaluation described above is that the effect of the side-wall boundary layer is approximately canceled out, since the over-all fringe shift from no-flow conditions is unimportant, only the relative fringe shifts from a point of known density being used. This is strictly true only if the integrated side-wall boundary-layer density, defined by

$$\int_0^{\delta} \rho \, dy \quad (8)$$

where y is the direction perpendicular to the tunnel wall and $y = 0$ is the wall, is the same over the entire field of view of the interferometer. Obviously, this can never be exactly true since the pressure field caused by the model, the boundary-layer growth, and the shock-wave and boundary-layer interaction all tend to change this value. An indication that all these effects might be small was obtained from the model tests where pressures were measured at two points on the model in the center of the span, where the flow is closely two-dimensional; the density increment between these two points on the model was compared with the density increment given by the interferogram. The standard deviation

from zero of the difference between these two increments over the whole range of test Mach numbers was about 1 percent of the stagnation density. Also, the values of pressure-drag coefficient obtained interferometrically for the attached-shock-wave cases checked the oblique-shock theory very closely, and it is well-known that the oblique-shock theory checks experiment quite well.

Determination of Free-Stream Mach Number

An interesting result of the method of evaluation just described is that the free-stream Mach number in subsonic flow can be determined from the interferogram and the measured pressure on the model, provided a large enough field of view ahead of the model is obtained in the interferogram. This can be done by noticing that a certain number of compression contours appear around the leading edge and then expansion contours follow these toward the back part of the airfoil; the center fringe corresponding to free-stream density can then be traced out into the flow field (see, e.g., figs. 9(a) to 9(d) of the 10° wedge in subsonic flow). The exact value of the density can be determined on this fringe as described previously and, hence, knowing the stagnation density in the settling chamber, the effective free-stream Mach number can be determined from the isentropic-flow relations. It is believed that this effective Mach number is a good approximation to the free-flight free-stream Mach number and would give the same flow as that measured in the wind tunnel for the very small models used in these tests.

This method is more accurate at high-subsonic speeds than at low speeds since more contour lines are obtained on the airfoil at the higher speeds (see above discussion). The estimated accuracy in determining free-stream Mach number in this way was ± 0.01 for the range of subsonic Mach numbers tested.

The free-stream Mach numbers for the supersonic tests were obtained by calibrating the flexible-nozzle jack settings against Mach number with a static-pressure probe in the center of the tunnel. The probe was traversed upstream and downstream in the region where the models were to be tested and an average Mach number was obtained there. The standard deviations from this average value were of the order of ± 0.005 in Mach number for the range of supersonic Mach numbers tested.

Wind-Tunnel Choking

In all the subsonic testing the embedded supersonic zone was not allowed to touch the upper or lower walls. In one or two of the low-supersonic tests there was a question whether the embedded subsonic zone touched the ceiling or not. In case it did, it is well-known that in

such cases the detached shock changes its curvature near the ceiling so as to come in nearly normal to the walls. Since the models were so very small (1/16 in. thick compared with the 10-in. height of the tunnel), it is believed that the effect of this on the pressure distribution was negligible.

Reynolds Number

The value of the Reynolds number for all of these tests was approximately 60,000 based on the chord of the model. The boundary layer on the models was laminar and no effort was made to trip the boundary layer to make it turbulent. The compression region in the shocks shown in the high-subsonic-flow interferograms is believed to be associated with the laminar boundary layer, as mentioned previously.

THEORETICAL WORK ON TRANSONIC FLOW

Relaxation Calculations

In 1946 Maccoll presented a paper at the Sixth International Congress for Applied Mechanics in which he described a relaxation calculation of the compressible flow past a 20° semiangle wedge followed by a straight section at Mach numbers of 0.7 and 1.5. The flow field in both cases contained both subsonic and supersonic velocities. His main assumptions were: (1) Sonic velocity occurs at the shoulder and (2) the streamlines of the flow are perpendicular to the sonic line (i.e., the line where sonic velocity occurs in the flow). The first assumption can be shown to be correct (see reference 22) so that indeed it is not an assumption. The second assumption, as Maccoll realized, was only approximately correct for $M_\infty = 1.5$ and certainly quite incorrect far away from the wedge at $M_\infty = 0.7$ (since the assumption leads to an infinite supersonic region above the wedge). In effect his solution at $M_\infty = 0.7$ was "choked" in the sense that the back part of the body could have no influence on the front part. It is well-known that for bodies at high-subsonic speeds a finite, closed supersonic region occurs in the flow, so that the sonic line makes all angles possible with the streamlines, including 0° . The method of solution used was to assume positions of the shock wave and sonic line, calculate the residues in the relaxation net using the isentropic-flow equations (an approximation since flow behind a curved shock is not isentropic), and then readjust the shock-wave and sonic-line location, calculate again, and so forth, iterating until the solution closely repeated itself. Maccoll found that the p/p_0 distribution on the wedge surface at $M_\infty = 1.5$ was nearly identical with the p/p_0 distribution at $M_\infty = 0.7$. This led him to propose that the pressure in the transonic region, on

bodies with distinct corners, varied as the stagnation pressure and he presented a drag curve through $M_{\infty} = 1$ for the 20° semiangle wedge calculated on this basis.

Drougge in 1948, following Maccoll, calculated the flow past a finite cone of 45° semiangle with detached shock wave at $M_{\infty} = 1.80$ and $M_{\infty} = 2.15$, using the same assumptions as Maccoll (reference 18). He also made experiments on this cone and found the agreement with his theory rather good. He made several tests at lower supersonic Mach numbers also and found that the p/p_0 distribution on the cone surface did remain nearly constant except as the Mach number became close to the attachment Mach number.

Drebinger in 1950 showed how to calculate, by relaxation techniques, the flow past finite cones and wedges with detached shocks, eliminating the isentropic-flow assumption and the assumption on the streamlines being perpendicular to the sonic line (reference 19). He calculated a specific example - a 26.6° semiangle wedge at $M_{\infty} = 1.440$ - and checked the calculated shock-wave shape and position experimentally. His calculations showed that, even for the detached-shock case, the streamlines differed from being perpendicular to the sonic lines by angles as large as 30° . His calculation was checked in detail experimentally in these tests and agreement was found to be excellent.

Transonic Perturbation Theory

By assuming that the velocity component parallel to the free stream direction differs only by a small quantity u from a^* , the critical velocity, and keeping only the highest-order terms in the differential equation, the equations of two-dimensional irrotational fluid motion are reduced to

$$\left. \begin{aligned} (\gamma + 1) \frac{u}{a^*} \frac{\partial u}{\partial x} + \frac{\partial v}{\partial y} &= 0 \\ \frac{\partial u}{\partial y} - \frac{\partial v}{\partial x} &= 0 \end{aligned} \right\} \quad (9)$$

It was from these equations that Von Kármán and Guderley independently arrived at the transonic similarity laws (references 9 and 4). For two-dimensional steady flow past sections whose shape functions are the same, these laws imply that

$$\frac{M^2 - 1}{[(\gamma + 1)t/c]^{2/3}} = f \left\{ \frac{M_\infty^2 - 1}{[(\gamma + 1)t/c]^{2/3}} \right\} \quad (10)$$

where M is the local Mach number on the surface of the section. The similarity in pressure and drag coefficients is then

$$\frac{(\gamma + 1)^{1/3} C_p}{(t/c)^{2/3}} = g \left\{ \frac{M_\infty^2 - 1}{[(\gamma + 1)t/c]^{2/3}} \right\} \quad (11)$$

$$\frac{(\gamma + 1)^{1/3} C_D}{(t/c)^{5/3}} = h \left\{ \frac{M_\infty^2 - 1}{[(\gamma + 1)t/c]^{2/3}} \right\} \quad (12)$$

These quantities will be called reduced local Mach number, reduced free-stream Mach number, reduced pressure coefficient, and reduced drag coefficient, respectively, using symbols ξ , ξ_∞ , \tilde{C}_p , and \tilde{C}_D .

By interchanging dependent and independent variables in the perturbation equations the problem becomes linear

$$\left. \begin{aligned} \bar{u} \frac{\partial y}{\partial \bar{v}} + \frac{\partial y}{\partial \bar{u}} &= 0 \\ \frac{\partial x}{\partial \bar{v}} - \frac{\partial y}{\partial \bar{u}} &= 0 \end{aligned} \right\} \quad (13)$$

where

$$\bar{u} = (\gamma + 1) \frac{u}{a^*}$$

$$\bar{v} = (\gamma + 1) \frac{v}{a^*}$$

and by eliminating x by differentiation, the Tricomi equation is obtained

$$\bar{u} \frac{\partial^2 y}{\partial v^2} + \frac{\partial^2 y}{\partial u^2} = 0 \quad (14)$$

The main difficulties with this hodograph (u,v) plane are: (a) The mapping of physical boundaries into the hodograph plane is in general not known until the solution to the problem is known so that it is not known where to apply the boundary conditions in the hodograph plane and (b) the mapping is often multivalued, complicating the solution. Two interesting cases are known where these difficulties are avoided. They are: (a) The free jet, studied by Tschaplygin in 1905, and (b) the finite wedge, studied recently by Guderley and Yoshihara, Vincenti and Wagoner, and Cole. These latter studies came to the author's attention after the present experimental study of the finite wedge in transonic flow had begun and served to make the study more interesting since the data could then be compared with the theoretical results.

Theoretical Studies of Transonic Flow past

Thin Wedge Sections

Guderley was apparently the first to formulate the problem of the thin finite wedge in the hodograph; he and Yoshihara found an approximate solution to the problem of the flow past a thin double-wedge profile at zero angle of attack at Mach number 1 using the transonic perturbation equations (reference 20).

Vincenti and Wagoner considered the thin double-wedge profile at zero angle of attack for low-supersonic reduced Mach numbers where the shock wave is detached (reference 21). Their solutions were effected by relaxation calculations in the hodograph plane. Here the bow shock wave and the sonic line are fixed boundaries (their positions are not known originally in the physical plane) and the boundary condition on the shock is the slope of the streamlines (or $y = \text{Constant}$ lines). This boundary condition was first shown by Busemann, who aptly called the configuration a "hedge hog."

Cole (reference 22) has recently given a simple approximate analytical solution to the flow past a thin wedge at zero angle of attack followed by a straight section at high-subsonic speeds ($M_\infty \leq 1$). His solution satisfies the Tricomi equation and the boundary conditions on the wedge and at infinity but not the boundary conditions on the sonic line. Effectively his solution gives a finite vertical sonic line from the shoulder which is also a limiting line. Cole has indicated that this solution is the singular part of the solution in the hodograph and as such is most likely the main part of the solution. It is

interesting to note that the drag-curve slope and curvature at $M_\infty = 1$ obtained from Cole's solution agree exactly with the values obtained from the simple physical considerations of the next section. Also, the pressure distribution on the wedge at $M_\infty = 1$ agrees within 1 or 2 percent with that obtained by Guderley and Yoshihara.

Since the back half of a double-wedge profile has only a very weak influence on the pressure distribution on the front half for $M_\infty > 1$ (only through the "last Mach wave" from the shoulder point to the sonic point on the detached shock), it is reasonable to take the solution of the double wedge at $M_\infty \geq 1$ and use the front-half solutions in connection with Cole's results for $M_\infty \leq 1$ for the wedge followed by a straight section and thus have a solution for the latter semi-infinite body completely through the transonic range. By using linearized subsonic theory and the shock-expansion supersonic theory, the zero-angle-of-attack flow is obtained for all possible values of M_∞ .

Tsien and Baron (reference 29) have shown that the shock-expansion theory can be expressed in the transonic similarity form for thin bodies in pure supersonic flow near $M_\infty = 1$.

Von Kármán (reference 9) has indicated also how linearized subsonic- and supersonic-flow results may be written in the transonic similarity form since, from the Prandtl-Glauert similarity, in linearized subsonic theory,

$$C_p = \frac{t/c}{\sqrt{1 - M_\infty^2}} f\left(\frac{x}{c}, \sqrt{1 - M_\infty^2} \frac{y}{c}\right) \quad (15)$$

and, in linearized supersonic theory,

$$C_p = \frac{t/c}{\sqrt{M_\infty^2 - 1}} g\left(\frac{x}{c}, \sqrt{M_\infty^2 - 1} \frac{y}{c}\right) \quad (16)$$

and from the expressions for reduced pressure coefficient and Mach number, multiplying both sides by $\frac{(\gamma + 1)^{1/3}}{(t/c)^{2/3}}$, these equations may also be written as:

$$\frac{(\gamma + 1)^{1/3} C_p}{(t/c)^{2/3}} = \sqrt{\frac{[(\gamma + 1)t/c]^{2/3}}{1 - M_\infty^2}} f\left\{ \frac{x}{c}, \sqrt{\frac{1 - M_\infty^2}{[(\gamma + 1)t/c]^{2/3}}} \left[(\gamma + 1) \frac{t}{c} \right]^{1/3} \frac{y}{c} \right\} \quad (15a)$$

$$\frac{(\gamma + 1)^{1/3} C_p}{(t/c)^{2/3}} = \sqrt{\frac{[(\gamma + 1)t/c]^{2/3}}{M_\infty^2 - 1}} \left\{ \frac{x}{c}, \sqrt{\frac{M_\infty^2 - 1}{[(\gamma + 1)t/c]^{2/3}} \left[(\gamma + 1) \frac{t}{c} \right]^{1/3}} \frac{y}{c} \right\} \quad (16a)$$

but

$$\tilde{C}_p = \frac{(\gamma + 1)^{1/3} C_p}{(t/c)^{2/3}}$$

$$\xi_\infty = \frac{M_\infty^2 - 1}{[(\gamma + 1)t/c]^{2/3}}$$

$$\tilde{y} = \left[(\gamma + 1)t/c \right]^{1/3} y$$

so equations (15) and (16) may be written in transonic form

$$\tilde{C}_p = F\left(\frac{x}{c}, \frac{\tilde{y}}{c}, \sqrt{-\xi_\infty}\right) \quad (17)$$

$$\tilde{C}_p = G\left(\frac{x}{c}, \frac{\tilde{y}}{c}, \sqrt{\xi_\infty}\right) \quad (18)$$

The subsonic pressure-distribution and drag-coefficient curves have been calculated here from Cole's analytical expressions and, combined with the results of Guderley and Yoshihara, Vincenti and Wagoner, and Tsien and Baron, the curves for reduced pressure and Mach number distribution and reduced drag coefficient¹ are given in figures 5 to 8 for the finite wedge followed by a straight section.

¹The reduced drag coefficient given in figure 8 is that for the half wedge and is equal to

$$\tilde{C}_D = \int_0^1 \tilde{C}_p d\left(\frac{x}{c}\right)$$

It can be shown that Cole's solution for large negative values of ξ_∞ goes over exactly into the linearized subsonic solution (see appendix A). The reduced-pressure-coefficient curve for $\xi_\infty = -2.02$ in figure 7 is so nearly identical for both solutions that they cannot be told apart (except that Cole's solution goes to $C_{p_{cr}}$ at $x/c = 1$ while the linearized solution goes to $-\infty$). This is to be expected since the transonic perturbation equations are not restricted to transonic flow but apply equally well to completely subsonic and completely supersonic flow.² The transonic equation can be written in the form

$$\left(1 - M_\infty^2\right) \frac{\partial^2 \phi}{\partial x^2} + \frac{\partial^2 \phi}{\partial y^2} = \frac{2M_\infty}{a_\infty} \left(1 + \frac{\gamma - 1}{2} M_\infty^2\right) \frac{\partial \phi}{\partial x} \frac{\partial^2 \phi}{\partial x^2} \quad (19)$$

where ϕ is the perturbation potential such that $u = U + \frac{\partial \phi}{\partial x}$, $v = \frac{\partial \phi}{\partial y}$. Thus it is clear that for completely subsonic or completely supersonic flows the term on the right is negligibly small but becomes of paramount importance in transonic flow.

CHARACTERISTIC FEATURES OF TRANSONIC FLOW PAST

WEDGE AND CIRCULAR-ARC SECTIONS

Characteristic Free-Stream Mach Numbers

Critical Mach number.- The Mach number at which sonic velocity first appears on the wedge is $M_\infty = 0$ (within the inviscid theory) since subsonic flow can not turn a sharp corner. Because of the fact that the boundary layer rounds off the corner, and perhaps also because of the spatial resolution limitations of the interferometric method, sonic velocity was not found there experimentally until approximately $\xi_\infty = -0.80$ for the wedges.

The critical Mach number for a half circular-arc airfoil followed by a straight section can be obtained approximately from linearized subsonic theory. This theory gives the surface pressure distribution as

$$C_p = \frac{-4(t/c)}{\pi \sqrt{1 - M_\infty^2}} \left[1 - \left(1 - \frac{x}{c}\right) \log \frac{x/c}{1 - x/c} \right] \quad (20)$$

²This was pointed out to the author by Dr. Milton Van Dyke of the NACA Ames Aeronautical Laboratory

which yields

$$C_{p_{\min}} = \frac{-1.626(t/c)}{\sqrt{1 - M_{\infty}^2}} \quad (21)$$

at $x/c = 0.783$ (see appendix B). This equation can also be written in transonic similarity form by multiplying both sides by $\frac{(\gamma + 1)^{1/3}}{(t/c)^{2/3}}$ (as shown in the previous section):

$$\tilde{C}_{p_{\min}} = \frac{-1.626}{\sqrt{-\xi_{\infty}}} \quad (22)$$

Now, within the transonic perturbation theory

$$\tilde{C}_p = -2(\xi - \xi_{\infty}) \quad (23)$$

Hence

$$C_{p_{cr}} = 2\xi_{\infty} \quad (24)$$

Equating $\tilde{C}_{p_{\min}}$ to $\tilde{C}_{p_{cr}}$ one obtains the critical reduced Mach number

$$\xi_{\infty_{cr}} = -0.871$$

For the thickness ratio $t/c = 0.088$ used in these tests, this predicts a critical Mach number of 0.834 at $x/c = 0.783$. Experimentally the critical Mach number was found to be 0.825 and occurred somewhere between $x/c = 0.75$ and 0.95 (the pressure distribution was very flat in this range). It is interesting to note that the experimental $M_{\infty_{cr}}$

was higher for the wedges than for the circular-arc profile of the same thickness ratio. This was probably due to a combination of three effects: (1) The boundary layer for the same Reynolds numbers used here was fairly thick in comparison with the dimensions of the model and thus it "rounded off" the shoulder more than would be the case at higher Reynolds numbers. (2) The height of the supersonic zone, even for an ideal nonviscous flow past thin wedges, appears to be quite small until the free-stream Mach number is quite close to 1. This is apparent from Cole's theory and also from the argument in reference 25 that the height of shocks in the supersonic zone must be of the form

$$\left[(\gamma + 1) \frac{t}{c} \right]^{1/3} \frac{h}{c} = \frac{1}{\xi_{\infty}^3} \tilde{C}_D$$

(3) The spatial resolution of the interferometric method may not have been sufficient to detect very small supersonic zones near the shoulder. There is also a large refraction error near the shoulder due to the high density gradients which tends to obscure details of the flow there.

Shock-attachment Mach number.- The shock-attachment Mach number depends only on the opening angle of the profile at the leading edge and can be predicted quite precisely by oblique-shock theory. If θ is the semiopening angle then it can be shown that approximately, for thin profiles,

$$\xi_{\infty A} = \frac{M_{\infty A}^2 - 1}{\left[(\gamma + 1)\theta \right]^{2/3}} = \frac{3}{4^{2/3}} \quad (25)$$

(see appendix C). If t/c is the thickness ratio of the circular-arc section, $\theta \approx 2(t/c)$. Hence for the circular-arc profile

$$\xi_{\infty A} = \frac{3}{2^{2/3}} \quad (26)$$

Mach number at which sonic velocity appears behind an oblique shock.- The Mach number at which sonic velocity appears behind an oblique shock $M_{\infty S}$ is just slightly higher than $M_{\infty A}$ and again is a function only of the opening angle. These values can also be found quite precisely from oblique-shock theory and approximately in similarity form can be given as

$$\xi_{\infty S} = \frac{M_{\infty S}^2 - 1}{\left[(\gamma + 1)\theta \right]^{2/3}} = 2^{1/3} \quad (27)$$

for the wedge (see appendix C) and

$$\xi_{\infty S} = 2 \quad (28)$$

for the circular-arc section

Characteristic Values of Local Mach Number

Mach number at leading edge.- The Mach number at the leading edge is zero (a stagnation point) for all free-stream Mach numbers less than the attachment Mach number.

Mach number at shoulder of wedge.- The Mach number at the shoulder of the wedge just before the turn is always 1. This is easily seen in the case of flow with detached shock since the only characteristic distance of the finite wedge is the distance from the leading edge to the shoulder which must determine the shock-detachment distance, and, if the sonic point occurred ahead of the shoulder, the shoulder could not influence the shock position. Subsonic flow cannot turn a sharp corner so the flow must therefore reach Mach number 1 right at the corner. In the case of subsonic free-stream flow the argument is not so simple (see reference 22).

At the shoulder the flow around the corner is locally a centered Prandtl-Meyer fan starting from $M = 1$. The Mach number just behind the corner is thus determined only by the wedge angle and is independent of the free-stream Mach number. Behind this point the flow will recompress to the free-stream Mach number through a shock or series of shocks, for free-stream Mach numbers less than the attachment Mach number. The expression for Mach number M_{PM} behind an expansion from $M = 1$ through an angle θ is

$$\theta = \sqrt{\frac{\gamma + 1}{\gamma - 1}} \tan^{-1} \sqrt{\frac{\gamma - 1}{\gamma + 1}} \sqrt{M_{PM}^2 - 1} - \tan^{-1} \sqrt{M_{PM}^2 - 1} \quad (29)$$

Expanding the right-hand side in powers of $\sqrt{M_{PM}^2 - 1}$ (assumed small) the first nonzero term yields

$$\theta \approx \frac{2}{3} \frac{(M_{PM}^2 - 1)^{3/2}}{\gamma + 1} \quad (30)$$

which is in transonic similarity form so

$$\xi_{PM} = \frac{M_{PM}^2 - 1}{[(\gamma + 1)\theta]^{2/3}} \approx \left(\frac{3}{2}\right)^{2/3} \quad (31)$$

PRESSURE DISTRIBUTION ON BODIES MOVING THROUGH AN
INFINITE FLUID AT SPEEDS NEAR MACH NUMBER 1

Stationary Value of Local Mach Number at Free-Stream
Mach Number 1

During the course of these investigations it was found that for the wedge and circular-arc sections the local Mach number distributions on these sections at very high subsonic speeds (above $M_{\infty cr}$ but below choking Mach number) and at very low supersonic speeds (where the detached shock wave was a chord length or so ahead of the section) were nearly identical. In trying to understand why this should be so, the following explanation was derived: (1) At low-supersonic speeds the bow shock wave is detached a great distance ahead of the profile and a subsonic flow region is embedded in the flow field between the shock and the sonic line. The part of the shock directly ahead of the profile is nearly normal over quite a distance (of course, the slope of the shock asymptotically tends to the slope of the Mach wave of the free-stream flow at large distances lateral to the flow direction). Nagamatsu (reference 30) has previously indicated this and points out that the flow past the profile should be closely approximated by assuming the profile is in a high-speed subsonic flow where the velocity distribution at infinity is slightly nonuniform, the minimum velocity being directly ahead of the profile and equal to the velocity behind the normal shock and then increasing in both lateral directions. (2) Now the normal shock near Mach number 1 is nearly symmetrical in the sense that the Mach number behind the shock is just as much below 1 as the Mach number ahead is above 1. This follows from the normal-shock relation:

$$1 - M_2^2 = \frac{M_1^2 - 1}{1 + \frac{2\gamma}{\gamma + 1}(M_1^2 - 1)} \quad (32)$$

where M_1 is the Mach number ahead of the shock and M_2 is the Mach number behind the shock; so near $M_1 = 1$,

$$1 - M_2^2 \approx M_1^2 - 1 \quad (33)$$

or

$$1 - M_2 \approx M_1 - 1 \quad (34)$$

Therefore if $M_\infty = 1 + \epsilon$ where ϵ is small, the flow past the profile is nearly the same as the flow past the profile at $M_\infty = 1 - \epsilon$ since the Mach number behind the central part of the detached shock wave is almost exactly $1 - \epsilon$. It follows therefore that the local Mach number distribution on the profile surface must have a stationary value at $M_\infty = 1$ and furthermore vary only slowly in the neighborhood of $M_\infty = 1$. Mathematically this means

$$\left. \frac{dM}{dM_\infty} \right|_{M_\infty=1} = 0 \quad (35)$$

It should be noticed that this argument is based on two assumptions:³ (1) The detached bow wave moves very far ahead of the profile as the flight Mach number decreases toward 1. (2) The radius of curvature of the detached bow wave at points directly ahead of the profile becomes extremely large as the flight Mach number decreases toward 1.

Examining these assumptions it would seem that the same reasoning should apply to any finite three-dimensional body in an infinite fluid traveling at speeds near Mach number 1, except that now two radii of curvature at points on the detached bow wave ahead of the body must be assumed to become large as the flight Mach number decreases toward 1. The detached bow wave is so far away from the body at speeds just slightly above Mach number 1 that the body appears as only a very small object in relation to the radii of curvature of the bow wave and, hence, it would appear as though the shape and attitude of the body could have no appreciable effect in changing the argument presented above.

The reasoning should also apply to an infinite yawed cylinder (whose cross section may be finite or, if the angle of attack is 0, may extend infinitely far downstream) provided that the Mach number considered is the component of the Mach number normal to the generators of the cylinder.

These arguments are for steady-flight speeds. Large accelerations through sonic flight speed could conceivably modify the phenomenon. Thus it is difficult to judge whether or not the available flight-test data confirm the concept since nearly all such data come from missile tests that involved large accelerations (or decelerations) through sonic flight speeds. The transonic-bump tests of Weaver on sweptback wings (reference 1) would seem to support these conclusions since they show

³It is believed that these are not actually assumptions but are capable of demonstration if one assumes a smooth variation of drag through Mach number 1.

drag-coefficient maximums very near Mach number 1, a necessary consequence of the concept for finite three-dimensional bodies and finite, unswept, two-dimensional bodies as will now be shown.

Slope of Pressure- and Drag-Coefficient Curves at $M_\infty = 1$

Equation (35) enables one to calculate the slope of the pressure- and drag-coefficient curves at Mach number 1 as follows:

$$C_p = \frac{p - p_\infty}{q_\infty} \quad (36)$$

$$= \frac{2}{\gamma M_\infty^2} \left[\frac{\left(1 + \frac{\gamma - 1}{2} M_\infty^2\right)^{\frac{\gamma}{\gamma - 1}}}{1 + \frac{\gamma - 1}{2} M^2} - 1 \right] \quad (37)$$

for isentropic flow so

$$\left. \frac{dC_p}{dM_\infty} \right|_{M_\infty=1} = \frac{4}{\gamma + 1} - \frac{2C_p}{\gamma + 1} \Big|_{M_\infty=1} \quad (38)$$

using

$$\left. \frac{dM}{dM_\infty} \right|_{M_\infty=1} = 0$$

Now for a two-dimensional body the pressure-drag coefficient (based on the chord) is given by the contour integral

$$C_D = \frac{-1}{c} \oint C_p (\hat{i} \cdot \hat{n}) ds \quad (39)$$

where

\hat{i} unit vector in stream direction

\hat{n} unit vector normal to profile pointing outward

ds element of length along profile contour

so if the angle of attack is constant and M_∞ is changing

$$\left. \frac{dC_D}{dM_\infty} \right|_{M_\infty=1} = -\frac{1}{c} \oint \left(\frac{4}{\gamma+1} - \frac{2C_p|_{M_\infty=1}}{\gamma+1} \right) \hat{i} \cdot \hat{n} ds \quad (40)$$

But $\oint \hat{i} \cdot \hat{n} ds = 0$ for a closed contour, so

$$\left. \frac{dC_D}{dM_\infty} \right|_{M_\infty=1} = -\frac{2}{\gamma+1} C_D|_{M_\infty=1} \quad (41)$$

For the front part of a profile (defined as that part ahead of the maximum thickness) the usual definition of a drag coefficient is

$$C_{DF} = -\frac{1}{c} \int_a^b C_p \hat{i} \cdot \hat{n} ds \quad (42)$$

where \int_a^b means the counterclockwise line integral from the point of maximum thickness on the upper surface to the point of maximum thickness on the lower surface; thus

$$\left. \frac{dC_{DF}}{dM_\infty} \right|_{M_\infty=1} = -\frac{1}{c} \int_a^b \left(\frac{4}{\gamma+1} - \frac{2C_p|_{M_\infty=1}}{\gamma+1} \right) \hat{i} \cdot \hat{n} ds$$

so

$$\left. \frac{dC_{DF}}{dM_\infty} \right|_{M_\infty=1} = \frac{4}{\gamma+1} \frac{t}{c} \cos \alpha - \frac{2}{\gamma+1} C_{DF}|_{M_\infty=1} \quad (43)$$

where

t maximum thickness of profile

α angle of attack of profile

Similarly the drag coefficient for the rear part is

$$C_{DR} = -\frac{1}{c} \int_b^a C_p \hat{i} \cdot \hat{n} ds \quad (44)$$

so

$$\left. \frac{dC_{DR}}{dM_\infty} \right|_{M_\infty=1} = -\frac{4}{\gamma+1} \frac{t}{c} \cos \alpha - \frac{2}{\gamma+1} C_{DR} \Big|_{M_\infty=1} \quad (45)$$

For the tests on wedge and circular-arc sections followed by straight sections the concept of drag coefficient of the front part of the section will often be used.

For bodies of revolution (which includes spheres, cone-cylinders, etc.) the pressure-drag coefficient (based on maximum cross-sectional area) at zero angle of attack is

$$C_D = \int_{x/l=0}^1 C_p d\left(\frac{r}{R}\right)^2 \quad (46)$$

where

- R maximum radius of body
 l length of body
 x distance from nose along axis

Therefore

$$\left. \frac{dC_D}{dM_\infty} \right|_{M_\infty=1} = \frac{-2C_D \Big|_{M_\infty=1}}{\gamma+1}$$

as before in the two-dimensional case. However, for front and back drag coefficients

$$C_{DF} = \int_{r=0}^R C_p d\left(\frac{r}{R}\right)^2 \quad (47)$$

so

$$\left. \frac{dC_{DF}}{dM_\infty} \right|_{M_\infty=1} = \frac{4}{\gamma + 1} - \frac{2}{\gamma + 1} C_{DF} \Big|_{M_\infty=1} \quad (48a)$$

and similarly

$$\left. \frac{dC_{DR}}{dM_\infty} \right|_{M_\infty=1} = -\frac{4}{\gamma + 1} - \frac{2}{\gamma + 1} C_{DR} \Big|_{M_\infty=1} \quad (48b)$$

and these differ from two-dimensional values obtained above in equations (43) and (45) by not involving the fineness ratio of the body (this is of course due to the different reference areas for drag coefficients).

For the general finite three-dimensional body the pressure-drag coefficient is given by

$$C_D = -\frac{1}{A} \iint_S C_p(\hat{i} \cdot \hat{n}) d\sigma \quad (49)$$

where A is some reference area of the body and S is the surface of the body. It follows as it did previously that

$$\left. \frac{dC_D}{dM_\infty} \right|_{M_\infty=1} = -\frac{2}{\gamma + 1} C_D \Big|_{M_\infty=1}$$

Slope of Drag-Coefficient Curve at $M_\infty = 1$ in Transonic

Similarity Parameters for Two-Dimensional Flows

Within the transonic approximation

$$C_p = -2(\xi - \xi_\infty) \quad (50)$$

so

$$\frac{dC_p}{d\xi_\infty} = -2 \left(\frac{d\xi}{d\xi_\infty} - 1 \right) \quad (51)$$

Now $\left. \frac{dM}{dM_\infty} \right|_{M_\infty=1} = 0$ implies that $\left. \frac{d\xi}{d\xi_\infty} \right|_{\xi_\infty=0} = 0$; hence

$$\left. \frac{d\tilde{C}_p}{d\xi_\infty} \right|_{\xi_\infty=0} = 2 \quad (52)$$

Now

$$\tilde{C}_p = -\frac{1}{t/c} \oint \tilde{C}_p \hat{i} \cdot \hat{n} d\left(\frac{s}{c}\right) \quad (53)$$

so

$$\left. \frac{d\tilde{C}_D}{d\xi_\infty} \right|_{\xi_\infty=0} = 0 \quad (54)$$

Similarly it is easy to show that

$$\left. \frac{d\tilde{C}_{DF}}{d\xi_\infty} \right|_{\xi_\infty=0} = 2 \quad (55)$$

and

$$\left. \frac{d\tilde{C}_{DR}}{d\xi_\infty} \right|_{\xi_\infty=0} = -2 \quad (56)$$

Other Data Showing Slow Variation of Local Mach

Number Near $M_\infty = 1$

As mentioned previously, Maccoll in 1946 had already proposed the slow variation of local Mach number near $M_\infty = 1$ on "bodies having distinct corners." It appears that this latter restriction is not necessary. Maccoll's proposal was based on rather slim evidence and it is believed that here, on the basis of the argument presented concerning the normal shock, the principle is explained more convincingly. Also the experimental evidence given here and by Drougge (reference 18), Bleakney and Griffith (personal communication), Weaver (reference 1), and by some NACA reports tends to bear out the conclusions of slow variation of local Mach number on bodies near $M_\infty = 1$.

This fact is sometimes slightly obscured in the NACA reports because pressure coefficient was plotted instead of p/p_0 or local Mach number. However, constant Mach number lines were sometimes drawn in these plots and there the evidence shows up strongly (see, e.g., reference 31, figs. 7 to 11, pp. 36 and 37). The relative constancy of local Mach number distribution near $M_\infty = 1$ for airfoils at an angle of attack is also shown clearly in figures 8, 9, and 10 of reference 32.

ON COMPARING THEORY AND EXPERIMENT

In references 21 and 25 discussions were presented on the philosophy of comparing experiments with approximate theories, and these discussions will not be repeated here, except to mention that in some of the theoretical curves presented here the values have been shown with a certain spread which results from using a pressure coefficient equal

to $-2 \frac{u - u_\infty}{a^*}$ or $-2 \frac{u - u_\infty}{U}$ (the former value is the one that fits

into transonic similarity theory; the latter value is the one more commonly used in perturbation analysis).

In connection with the idea presented in reference 25 of extrapolating experimental data to zero thickness in order to compare with results from transonic perturbation analyses, it is interesting to note that the characteristic Mach numbers mentioned in the section "Characteristic Features of Transonic Flow past Wedge and Circular-Arc Sections" can be presented in powers of the thickness of the wedge (or equivalently in powers of the wedge angle), the first term of which gives the transonic similarity expression; two of these values are

$$\begin{aligned} \xi_\infty S &= \frac{M_\infty^2 - 1}{[(\gamma + 1)\theta]^{2/3}} \\ &= 2^{1/3} \left[1 + \frac{19\gamma + 2}{24} \left(\frac{2}{\gamma + 1} \right)^{1/3} \theta^{2/3} + o(\theta^{4/3}) \right] \end{aligned} \quad (57)$$

$$\begin{aligned} \xi_{PM} &= \frac{M_{PM}^2 - 1}{[(\gamma + 1)\theta]^{2/3}} \\ &= \left(\frac{3}{2} \right)^{2/3} \left\{ 1 + \frac{4\gamma}{5(\gamma + 1)} \left[\frac{3(\gamma + 1)}{2} \right]^{2/3} \theta^{2/3} + o(\theta^{4/3}) \right\} \end{aligned} \quad (58)$$

(See appendixes D and E.) In transonic perturbation theory the terms

in θ on the right-hand side are neglected. This can lead to fairly large errors for even moderately large values of θ since the approach to $\theta = 0$ is nonlinear and

$$\frac{d\xi_{\infty S}}{d\theta} \quad \text{and} \quad \frac{d\xi_{PM}}{d\theta} \rightarrow \infty \quad \text{as} \quad \theta \rightarrow 0 \quad (59)$$

Judging from this one might expect that quantitative agreement of transonic perturbation analyses with experiment would not be so good. However, in comparing two similar shapes with only slightly different thickness ratios by transonic similarity considerations one would expect fairly good agreement.

EXPERIMENTAL RESULTS

Flow Field near 10° Wedge

Figure 9 shows interferograms of the flow past the 10° semiangle wedge for 14 Mach numbers from 0.700 to 0.892 and 1.207 to 1.465 (the interferograms for the $4\frac{1}{2}^\circ$ and $7\frac{1}{2}^\circ$ wedges were very similar and hence are not shown here). Notice that the lines of constant density in the subsonic-flow interferograms are roughly elliptical in shape as predicted by the theory (see appendixes A and B). A supersonic flow region was first detected between $M_\infty = 0.700$ and 0.794 (the sonic line is shown as a dashed line in the figs.) and a shock emanating from the corner appears in the supersonic zone at $M_\infty = 0.794$. As the Mach number was increased, this zone grew larger and a shock appeared at the rear of it, while the shock emanating from the corner weakened and disappeared. This rearward shock was of the typical λ type associated with a laminar boundary layer, and the interferograms clearly indicated the separation of the boundary layer ahead of this shock. The similarity between the flow field at $M_\infty = 0.892$ and at $M_\infty = 1.207$ (figs. 9(d) and 9(e)) is striking; the base of the rearward shock has moved quite far back on the wake of the blunt trailing edge at $M_\infty = 1.207$ but in the vicinity of and ahead of the sonic line the two fields are nearly identical except for the detached shock wave which appears about $1\frac{1}{2}$ chord lengths ahead of the wedge at $M_\infty = 1.207$. As the Mach number was increased above 1.207, the detached shock moved in closer to the leading edge and finally "attached" at a Mach number quite close to the theoretical attachment Mach number of $M_\infty = 1.418$. Notice that the process of attachment is very continuous. The effect of the boundary layer is quite noticeable in the last few interferograms: This can be roughly accounted for by considering the boundary layer to change the shape of

the body by its displacement thickness and then considering a nonviscous flow past this revised shape. On the wedge the boundary layer will not grow so rapidly as on a flat plate because of the favorable pressure gradient and, in fact, the effect of the strong expansion around the corner is known to cause an almost complete collapse of the boundary layer there. As the bow shock wave gets close to attachment the velocities in the subsonic region behind it are getting very close to sonic velocity and hence the flow in this region is very sensitive to any slight curvature of the "revised shape" of the wedge. This accounts for the shift of the base of the sonic line forward to the leading edge as the shock approaches attachment. The nonviscous theory would indicate that the sonic line would always begin at the corner and, at a Mach number just slightly above the shock-attachment Mach number, the whole subsonic region would become sonic; then, with increasing Mach number, the flow behind the shock would be completely supersonic. As observed, the boundary-layer effect is to make the wedge have a curved surface and the sonic line actually moves slowly from the corner to the nose. Even with attached shock wave at $M_\infty = 1.465$ the flow behind the shock is not quite uniform (as nonviscous theory would indicate it should be) because of the effective curved surface caused by the boundary layer.

Local Mach Number Distributions on Three Thin Wedges

Figure 10 shows the variation of local Mach number distribution on the surfaces of the $4\frac{1}{2}^\circ$, $7\frac{1}{2}^\circ$, and 10° semiangle wedges with free-stream Mach number. This should be compared with figure 5 which shows the corresponding theoretical curves in terms of the transonic similarity parameters. The general behavior of the theoretical and experimental curves is quite definitely in good agreement. Particularly noteworthy is the slow variation of the local Mach number distribution near free-stream Mach number 1.

Pressure-Coefficient Distributions on Three Thin Wedges

The slow variation of the Mach number distribution in the range near $M_\infty = 1$ is obscured when the results are plotted in terms of pressure coefficient, since the pressure coefficient changes a great deal if local Mach number is constant while the free-stream Mach number changes. A better parameter for presenting transonic pressure distributions would be p/p_0 (p/p_0' in case of a detached shock). Typical C_p distributions are shown in figure 11 for the $7\frac{1}{2}^\circ$ wedge (the results for the 10° and $4\frac{1}{2}^\circ$ wedges were very similar and hence they are not presented).

The points shown were where the fringes intersected the body in the interferograms. Since for a wedge the drag coefficient is proportional to the average C_p , the drag rise is evident in the subsonic distributions as the point where $C_p = 0$ moves rearward with increasing free-stream Mach number. Linearized subsonic theory (which predicts $C_D = 0$) locates the $C_p = 0$ point at $x/c = 50$ percent. Figure 7 shows theoretical reduced C_p distributions at various reduced free-stream Mach numbers. Again the qualitative agreement of these curves with experiment is evident.

Shock-Detachment Distance for Three Thin Wedges

Figure 12 shows the shock-detachment distance against reduced free-stream Mach number for the three thin wedges and includes the theoretical values from reference 21. Here Vincenti and Wagoner's values for

ξ_{∞} have been multiplied by $\frac{\xi_{\infty A} \Big|_{\theta=7\frac{1}{2}^\circ}}{\xi_{\infty A} \Big|_{\theta=0^\circ}}$ in order to make the transonic

perturbation value of detachment reduced Mach number agree with the value from oblique-shock theory for the $7\frac{1}{2}^\circ$ wedge:⁴ The reason for this was discussed in the section "On Comparing Theory and Experiment," namely, the difficulty of comparing transonic perturbation theory quantitatively with experiment. Notice how rapidly the shock wave moves away from the wedge as the Mach number is decreased toward 1.

Drag-Coefficient Variation with Mach Number for Three Thin Wedges

It was shown in reference 25 that the viscous effects on the wedge tend to compensate each other at the leading edge and the shoulder so that the over-all pressure drag is nearly the same as if the flow were inviscid. Thus it would be expected that the pressure-drag coefficients obtained by integrating the experimental pressure distributions would check the inviscid transonic perturbation theory. The reduced drag

⁴In terms of Mach number, for the $7\frac{1}{2}^\circ$ wedge the shock theory predicts attachment at $M_{\infty A} = 1.33$ ($\xi_{\infty A} = 1.68$), while the transonic perturbation theory predicts $M_{\infty A} = 1.25$ ($\xi_{\infty A} = 1.19$).

coefficient used here was

$$\tilde{c}_D = \int_0^1 \tilde{c}_p d\left(\frac{x}{c}\right) \quad (60)$$

which is, in essence, the reduced drag coefficient of the upper (or lower) half wedge. This was done since the wedge model was regarded as the front half of a double-wedge profile and hence the value given here is the part of the reduced drag coefficient contributed by the front half of such an airfoil (C_{DF} as in equation (42)), based on the chord of the double-wedge profile, which would be twice the chord of the model used here. Of course, this viewpoint is valid only for supersonic free-stream Mach numbers.

Figure 13 shows the reduced drag coefficients for the three thin wedges plotted against reduced Mach number. It is seen that the results give nearly a universal curve, which they should if the transonic similarity law is true, but that there are systematic variations with wedge angle. This is to be expected based on the discussion of the section "On Comparing Theory and Experiment." The vertical lines through the experimental points indicate estimated accuracy of the data. This figure should be compared with figure 8, the theoretical reduced-drag-coefficient variation with reduced Mach number. It is obvious that the qualitative agreement of theory and experiment is good. In figure 14 the theory and experiment are compared directly for the three thin wedges. Here the theoretical drag coefficients are shown with a vertical spread, the upper values for $M_\infty > 1$ corresponding to the use of

the pressure coefficient $C_p = \frac{-2(u - u_\infty)}{a^*}$ and the lower values, to the

use of the pressure coefficient $C_p = \frac{-2(u - u_\infty)}{U}$. The situation is vice versa for $M_\infty < 1$. From this figure it is evident that the transonic perturbation theory gives a good approximation to experiment.

Flow Field at $M_\infty = 1.44$ for the 26.6° Wedge

Figure 15 shows the experimental and theoretical constant-velocity lines in the subsonic region behind the detached shock wave for a 26.57° semiangle wedge at $M_\infty = 1.44$. The theoretical analysis was made from relaxation calculations by Drebinger (reference 19) who used the flow equations with entropy variation behind the shock taken into account. The experimental constant-velocity lines were determined from the isopycnic lines of the interferogram by taking into account the lateral stagnation-pressure gradient behind the curved shock. The

isopycnic lines near this strong shock wave were probably slightly in error because of the "smearing out" of the pressure discontinuity across the shock in the side-wall boundary layers. It is seen that the agreement between theory and experiment on detachment distance and constant-velocity contours near the wedge is good.

Figure 16 shows the surface pressure distribution from reference 17 and the present experiments. Again it is seen that the agreement is good.

Flow Field near the 8.8-Percent Circular-Arc Section

Figure 17 shows interferograms of the flow past the 8.8-percent circular-arc section for 14 Mach numbers from 0.718 to 0.936 and 1.11 to 1.500.

Supersonic velocity first occurred at $M_\infty = 0.825$ (see the section "Critical Mach number") and in figures 17(c) and 17(d) a nearly symmetric supersonic zone is shown at $M_\infty = 0.848$. No shock waves were apparent in this zone although a sensitive schlieren apparatus might have shown some weak shocks there. At $M_\infty = 0.890$ the supersonic zone has grown rapidly and now terminates in the λ -shock configuration. Further increase of the Mach number to $M_\infty = 0.935$ (figs. 17(e) and 17(f)) shows the supersonic zone increasing laterally and the terminating shock moving rearward into the wake of the body. Figures 17(e) and 17(f) also show the density distribution at $M_\infty \approx 1.11$ (the detached shock wave was just out of the field of view of the interferometer) and it is interesting to note the similarity between the flow field at $M_\infty = 0.935$ and $M_\infty \approx 1.11$. It would appear as though the shock terminating the supersonic zone at $M_\infty = 0.935$ had moved rearward to form the trailing-edge shock (which is actually in the wake here because of the blunt trailing edge) and the supersonic zone had grown laterally until the sonic line joined with the detached shock far away from the body at $M_\infty = 1$, thus causing an embedded subsonic zone in the supersonic flow with further increase in Mach number.

With further increase of Mach number above $M_\infty = 1.11$, figures 17(g) to 17(n) show that the detached shock again approached the leading edge and the embedded subsonic zone decreased in size until finally the shock "attached" somewhere between $M_\infty = 1.400$ and $M_\infty = 1.450$ (the theoretical value being $M_{\infty A} = 1.423$).

Local Mach Number Distributions on 8.8-Percent Circular-Arc Section

Figure 18 shows the local Mach number distributions for the 8.8-percent circular-arc section as obtained from the experiments at

various free-stream Mach numbers. Again it is apparent that the variation of local Mach number distribution near $M_\infty = 1$ is very slow and, indeed, the distribution for $M_\infty = 1$ could be interpolated from this figure with good accuracy.

Figure 19 is a cross plot of the data of figure 18 except that here the data are given in transonic similarity parameters. This figure shows contours of constant reduced local Mach number on a plot of reduced free-stream Mach number against chordwise position. The dashed lines represent subsonic local Mach numbers; the solid lines, supersonic local Mach numbers. Note again the slow variation of local Mach number distribution with free-stream Mach number near sonic velocity.

Pressure-Coefficient Distributions on 8.8-Percent

Circular-Arc Section

Figure 20 shows the pressure-coefficient distributions on the 8.8-percent circular-arc section for various free-stream Mach numbers. The points shown are where the fringes intersected the body in the interferogram. Again the presentation in this manner obscures the interesting fact observed in figure 18.

Drag-Coefficient Variation with Mach Number for 8.8-Percent

Circular-Arc Section

Figure 21 shows the experimental determination of the drag coefficient of the front part of the 8.8-percent circular-arc section. This again is of the nature of a fore-drag coefficient and, as shown in equation (43), it should have a positive slope equal to

$$\frac{4}{\gamma + 1} \frac{t}{c} - \frac{2}{\gamma + 1} C_D \Big|_{M_\infty=1} \quad \text{at } M_\infty = 1; \text{ this is how the subsonic data have}$$

been joined with the supersonic data. The vertical lines through the experimental points again indicate estimated accuracy of the data. For the case of an attached shock the pressure distribution can be calculated using characteristics theory and the shock polar; however, a close approximation is obtained by considering the flow behind the shock wave to be Prandtl-Meyer flow. (This yields, approximately, parabolic-shaped bow and trailing-edge shock waves; see reference 33.) From this pressure distribution the drag was calculated and is shown in figure 21. Taking into account the "reflected" characteristics from the shock wave would give more compression and increase the drag coefficient so that it would agree better with the experimental values of $M_\infty = 1.450$ and 1.500 shown in figure 21.

Note that the tests were made at low enough supersonic speeds to get definitely below the drag-coefficient maximum at $M_\infty \approx 1.20$.

Local Mach Number Distributions on a 12-Percent

Biconvex Circular-Arc Airfoil

Figure 22 shows local Mach number distributions from reference 8 for high-subsonic-speed flow over a 12-percent biconvex circular-arc airfoil (with turbulent boundary layer). The data for the 8.8-percent circular-arc section at two supersonic speeds have been scaled according to the transonic similarity laws to the 12-percent case and are shown for the front half of the 12-percent airfoil in figure 22. The back half for these two cases has been faired in using a Prandtl-Meyer expansion which should be approximately correct (a more accurate determination could have been made using characteristics theory and the shock polar). At $M_\infty = 1.58$, the theory indicates that the shock is attached with sonic speed just behind the shock on the leading edge, so that the distribution can be obtained by standard methods mentioned above; again the Prandtl-Meyer expansion approximation was used for the distribution at $M_\infty = 1.58$ in figure 22.

The behavior of the Mach number distributions is similar to those shown previously, except in this case the movement of the shock terminating the local supersonic zone is shown. Apparently little change in local Mach number distribution occurs between $M_\infty = 0.936$ and $M_\infty = 1.29$.

Drag-Coefficient Variation with Mach Number for a

12-Percent Biconvex Circular-Arc Airfoil

The data of figure 23 were converted to pressures which were integrated to give the pressure-drag coefficient for the various free-stream Mach numbers. In addition the drags of the front and back halves are shown separately. The drag-coefficient variation between $M_\infty = 0.96$ and $M_\infty = 1.20$ was based on constant local Mach number distribution at values interpolated between the curves for $M_\infty = 0.936$ and $M_\infty = 1.29$. The data were faired into the curves for attached shock wave calculated on the Prandtl-Meyer expansion basis. It is seen that the fore-drag coefficient has a maximum after $M_\infty = 1$ while the drag coefficient of the rear part has a maximum before $M_\infty = 1$. The over-all airfoil has a maximum drag coefficient just before $M_\infty = 1$ in order for the curve to have the slightly negative slope at $M_\infty = 1$ given by equation (41).

CONCLUSIONS

The transonic similarity theory of Von Kármán and Guderley was checked and found to be in good agreement with experiment for thin wedge profiles near a free-stream Mach number of 1.

The results of theoretical calculations, using transonic perturbation theory, made by Guderley and Yoshihara, Vincenti and Wagoner, and Cole for a wedge in transonic flow were checked experimentally at high-subsonic and low-supersonic speeds for three wedges of different angles and were found to be in good agreement with experiment.

The flow field and the surface pressure distribution for a 26.6° semiangle wedge at a free-stream Mach number of 1.44 were obtained experimentally and were found to be in excellent agreement with the theoretical calculations of this flow made by Drebinger.

The pressure distributions and drag coefficients for an 8.8-percent circular-arc section followed by a straight section and for a 12-percent biconvex circular-arc airfoil were presented completely through the transonic range. It was shown that some difficulty arises in comparing two-dimensional transonic perturbation theory with experiment, since this theory neglects thickness-ratio terms of order $(t/c)^{2/3}$ and higher; for even moderate thickness-ratios this will cause noticeable deviations from more exact theory.

It was shown from some physical arguments that the local Mach number distribution on bodies traveling through an infinite fluid has a stationary value at free-stream Mach number 1. This was verified experimentally for the case of two-dimensional flow. It was shown that this concept implies a drag-coefficient maximum just below free-stream Mach number 1 for all bodies in steady flight. This fact can be used to obtain the variation of local Mach number distribution on bodies completely through the transonic range of velocities from wind-tunnel tests, provided small models are used so that tests can be carried well above critical Mach number and to low-enough supersonic Mach numbers so that the bow shock wave is detached a chord length or so.

California Institute of Technology
Pasadena, Calif., June 1, 1951

APPENDIX A

ASYMPTOTIC REPRESENTATION OF COLE'S SOLUTION FOR LARGE
NEGATIVE VALUES OF REDUCED FREE-STREAM MACH NUMBER

Cole's solution for the high-subsonic-velocity flow past a thin wedge (reference 22) is given as follows (in Cole's notation)

$$y(z, v; z_1) = \left(\frac{2zz_1}{3}\right)^{1/3} v_0 \int_0^\infty \frac{\sinh \lambda (v_0 - v)}{\sinh \lambda v_0} J_{-1/3}(\lambda z) J_{-1/3}(\lambda z_1) \lambda \, d\lambda \quad (61)$$

$$x(z, v; z_1) = 1 - z_1^{1/3} z^{2/3} v_0 \int_0^\infty \frac{\cosh \lambda (v_0 - v)}{\sinh \lambda v_0} J_{2/3}(\lambda z) J_{-1/3}(\lambda z_1) \lambda \, d\lambda \quad (62)$$

where the center line of the wedge is at $y = 0$; the leading edge, at $x = 0$; the shoulder, at $x = 1$; and

$$\left. \begin{aligned} z &= \frac{2}{3} (1 - M_\infty^2)^{3/2} = \frac{2}{3} \left[-(\gamma + 1) \frac{u}{a^*} \right]^{3/2} \\ z_1 &= \frac{2}{3} (1 - M_\infty^2)^{3/2} = \frac{2}{3} \left[-(\gamma + 1) \frac{u_\infty}{a^*} \right]^{3/2} \\ v_0 &= (\gamma + 1)\theta \end{aligned} \right\} \quad (63)$$

and the other notation is the same as that in the present paper.

Using the standard methods of partial-fraction expansion one may write

$$\frac{\sinh \lambda (v_0 - v)}{\sinh \lambda v_0} = 1 - \frac{v}{v_0} + 2 \sum_{n=1}^{\infty} \sin \left(n\pi \frac{v}{v_0} \right) \frac{\lambda^2 v_0^2}{\lambda^2 v_0^2 + n^2 \pi^2} \quad (64)$$

$$\frac{\cosh \lambda (v_0 - v)}{\sinh \lambda v_0} = \frac{1}{\lambda v_0} + 2 \sum_{n=1}^{\infty} \cos \left(n\pi \frac{v}{v_0} \right) \frac{\lambda v_0}{\lambda^2 v_0^2 + n^2 \pi^2} \tag{65}$$

Substituting these into the integrals above and making use of the integrals

$$\int_0^{\infty} \frac{\lambda^3}{\lambda^2 + \alpha^2} J_{-1/3}(\lambda\beta) J_{-1/3}(\lambda\gamma) d\lambda = \begin{cases} -\alpha^2 I_{-1/3}(\alpha\gamma) K_{-1/3}(\alpha\beta) & \beta > \gamma > 0 \\ -\alpha^2 K_{1/3}(\alpha\gamma) I_{-1/3}(\alpha\beta) & \gamma > \beta > 0 \end{cases} \tag{66}$$

and

$$\int_0^{\infty} \frac{\lambda^2}{\lambda^2 + \alpha^2} J_{-1/3}(\lambda\beta) J_{2/3}(\lambda\gamma) d\lambda = \begin{cases} -\alpha I_{2/3}(\alpha\gamma) K_{-1/3}(\alpha\beta) & \beta > \gamma > 0 \\ \alpha K_{2/3}(\alpha\gamma) I_{-1/3}(\alpha\beta) & \gamma > \beta > 0 \end{cases} \tag{67}^5$$

equations (61) and (62) can be written as

$$\tilde{y} = v_0^{1/3} y = \begin{cases} 2 \left(\frac{2}{3} \frac{z}{v_0} \frac{z_1}{v_0} \right)^{1/3} \sum_{n=1}^{\infty} n\pi \sin \left(n\pi \frac{v}{v_0} \right) I_{-1/3} \left(n\pi \frac{z}{v_0} \right) K_{-1/3} \left(n\pi \frac{z_1}{v_0} \right); & z_1 > z > 0 \\ 2 \left(\frac{2}{3} \frac{z}{v_0} \frac{z_1}{v_0} \right)^{1/3} \sum_{n=1}^{\infty} n\pi \sin \left(n\pi \frac{v}{v_0} \right) K_{-1/3} \left(n\pi \frac{z}{v_0} \right) I_{-1/3} \left(n\pi \frac{z_1}{v_0} \right); & z > z_1 > 0 \end{cases} \tag{68}$$

⁵Equation (67) is from reference 34; equation (66) is obtained by differentiation of equation (67) with respect to γ .

$$x = \begin{cases} 1 + 2 \left(\frac{z_1}{v_0} \right)^{1/3} \left(\frac{z}{v_0} \right)^{2/3} \sum_{n=1}^{\infty} n\pi \cos \left(n\pi \frac{v}{v_0} \right) I_{2/3} \left(n\pi \frac{z}{v_0} \right) K_{-1/3} \left(n\pi \frac{z_1}{v_0} \right); & z_1 > z > 0 \\ -2 \left(\frac{z_1}{v_0} \right)^{1/3} \left(\frac{z}{v_0} \right)^{2/3} \sum_{n=1}^{\infty} n\pi \cos \left(n\pi \frac{v}{v_0} \right) K_{2/3} \left(n\pi \frac{z}{v_0} \right) I_{-1/3} \left(n\pi \frac{z_1}{v_0} \right); & z > z_1 > 0 \end{cases} \quad (69)$$

Making use of the asymptotic formulas

$$I_\nu(z) \approx \frac{1}{\sqrt{2\pi z}} e^z + \dots \text{ as } z \rightarrow \infty \quad (70)$$

$$K_\nu(z) \approx \sqrt{\frac{\pi}{2z}} e^{-z} + \dots \text{ as } z \rightarrow \infty \quad (71)$$

and the simple summations

$$\sum_{n=1}^{\infty} e^{-an} \sin n\pi x = \frac{\sin \pi x}{2 \cosh a - 2 \cos \pi x} \quad (72)$$

$$\sum_{n=1}^{\infty} e^{-an} \cos n\pi x = \frac{\cos \pi x - e^{-a}}{2 \cosh a - 2 \cos \pi x} \quad (73)$$

Figures 5, 6, and 7 were calculated from this equation for $v = 0$, for the cases $\xi_\infty \leq 0$.

one can write equations (68) and (69) for large values of z and z_1 as

$$\tilde{y} \approx \frac{1}{2} \left(\frac{z}{3} \right)^{1/3} \left(\frac{z}{v_0} \frac{z_1}{v_0} \right)^{-1/6} \frac{\sin \pi \frac{v}{v_0}}{\cosh \frac{\pi(z - z_1)}{v_0} - \cos \pi \frac{v}{v_0}}; \quad z, z_1 \rightarrow \infty \quad (74)$$

$$x \approx \left\{ \begin{array}{l} 1 + \frac{1}{2} \left(\frac{z}{z_1} \right)^{1/6} \frac{\cos \pi \frac{v}{v_0} - e^{\pi(z-z_1)/v_0}}{\cosh \frac{\pi(z - z_1)}{v_0} - \cos \pi \frac{v}{v_0}}; \quad z_1 > z \rightarrow \infty \\ -\frac{1}{2} \left(\frac{z}{z_1} \right)^{1/6} \frac{\cos \pi \frac{v}{v_0} - e^{-\pi(z-z_1)/v_0}}{\cosh \frac{\pi(z - z_1)}{v_0} - \cos \pi \frac{v}{v_0}}; \quad z > z_1 \rightarrow \infty \end{array} \right. \quad (75)$$

Eliminate v between equations (74) and (75) for $z_1 > z \rightarrow \infty$

$$\left[\frac{y}{\left(\frac{z}{z_1} \right)^{1/6} 2 \left(\frac{3z_1}{2} \right)^{1/3} \sinh \frac{\pi(z - z_1)}{v_0}} \right]^2 + \left[\frac{x + \frac{\left(\frac{z}{z_1} \right)^{1/6} e^{-\pi(z-z_1)/v_0}}{2 \sinh \frac{\pi(z - z_1)}{v_0}}}{\frac{\left(\frac{z}{z_1} \right)^{1/6}}{2 \sinh \frac{\pi(z - z_1)}{v_0}}} \right]^2 = 1 \quad (76)$$

and for $z > z_1 \rightarrow \infty$ simply replace x by $x - 1$ and $z - z_1$ by $z_1 - z$ in equation (76). Thus the lines of constant Mach number are ellipses with center on $y = 0$, with ratio of semiaxes equal to

$$\left(\frac{3z_1}{2} \right)^{1/3} = \sqrt{1 - M_\infty^2} \quad (77)$$

which is precisely the solution given by the linearized subsonic theory (see appendix B).

Now, in the notation of the present paper,

$$\frac{\pi(z - z_1)}{v_0} = \frac{2\pi}{3} \left[(-\xi)^{3/2} - (-\xi_\infty)^{3/2} \right]$$

and since $\xi - \xi_\infty$ is small on the wedge and since

$$\tilde{C}_p = -2(\xi - \xi_\infty)$$

one can write

$$\frac{\pi(z - z_1)}{v_0} = \frac{2\pi(-\xi_\infty)^{3/2}}{3} \left\{ \left[1 - \frac{\tilde{C}_p}{2(-\xi_\infty)} \right]^{3/2} - 1 \right\}$$

Hence,

$$\frac{\pi(z - z_1)}{v_0} = \frac{2\pi(-\xi_\infty)^{3/2}}{3} \left\{ \left[1 - \frac{3}{4} \frac{\tilde{C}_p}{(-\xi_\infty)} + \dots \right] - 1 \right\}$$

so, approximately,

$$\frac{\pi(z - z_1)}{v_0} \approx -\frac{\pi(-\xi_\infty)^{1/2}}{2} \tilde{C}_p = -\frac{\pi}{2} \frac{C_p \sqrt{1 - M_\infty^2}}{\theta}; \quad z, z_1 \rightarrow \infty \quad (78)$$

Similarly, for large values of z and z_1 it follows that

$$\left(\frac{z}{z_1} \right)^{1/6} \approx 1; \quad z, z_1 \rightarrow \infty \quad \text{for } z - z_1 \text{ small} \quad (79)$$

Substituting equations (78) and (79) into equation (16) one gets the exact linearized subsonic solution for constant-velocity lines (see appendix B). Therefore on the wedge ($y = 0$), from equations (76), (78),

and (79), one has approximately for large values of z and z_1

$$x + \frac{1}{e^{\pi\sqrt{-\xi_\infty}\tilde{C}_p} - 1} = \pm \frac{1}{e^{\frac{\pi}{2}\sqrt{-\xi_\infty}\tilde{C}_p} - e^{-\frac{\pi}{2}\sqrt{-\xi_\infty}\tilde{C}_p}}$$

Solving this for \tilde{C}_p

$$\tilde{C}_p \sqrt{-\xi_\infty} = -\frac{2}{\pi} \log_e \frac{1-x}{x}$$

or

$$C_p = \frac{-2\theta}{\pi \sqrt{1 - M_\infty^2}} \log_e \frac{x}{x-1} \quad (80)$$

which is precisely the linearized subsonic solution for flow past a wedge (see appendix B). Thus Cole's solution far away from $M_\infty = 1$ tends exactly to the linearized subsonic solution.

APPENDIX B

LINEARIZED SUBSONIC AND SUPERSONIC FLOW PAST WEDGE
AND CIRCULAR-ARC SECTIONS

Linearized Subsonic Flow past a Wedge

Let the wedge center line be on $y = 0$, with the leading edge at $x = 0$ and the shoulder at $x = c$. Then the incompressible-flow problem is to find an analytic function $u - iv$ such that $v = 0$ on $y = 0$ except for $0 < x < c$ where $v = U\theta$ and $u - iv = 0$ at infinity. Such a function is

$$u - iv = \frac{U\theta}{\pi} \log_e \frac{z/c}{(z/c) - 1} \quad (81)$$

where

$$z = x + iy$$

U free-stream velocity

Thus on $y = 0$,

$$C_{p0} = \frac{-2u}{U} = \frac{-2\theta}{\pi} \log_e \frac{x/c}{1 - (x/c)} \quad (82)$$

Using the Prandtl-Glauert transformation, for linearized subsonic flow

$$C_p = \frac{C_{p0}}{\sqrt{1 - M_\infty^2}} = \frac{-2\theta}{\pi \sqrt{1 - M_\infty^2}} \log_e \frac{x/c}{1 - (x/c)} \quad (83)$$

or in transonic similarity notation

$$\tilde{C}_p = \frac{-2}{\pi \sqrt{-\xi_\infty}} \log_e \frac{x/c}{1 - (x/c)} \quad (84)$$

For the incompressible case the lines of constant pressure in the fluid will be where

$$\frac{z/c}{(z/c) - 1} = \text{Constant}$$

but these are circles with centers at

$$x = \frac{e \frac{-\pi C_p}{\theta}}{1 - e \frac{-\pi C_p}{\theta}}, \quad y = 0 \quad (85)$$

and radii

$$\frac{e \frac{-\pi C_p}{2\theta}}{1 - e \frac{-\pi C_p}{\theta}}$$

In the Prandtl-Glauert transformation, the y distance is stretched by the factor $\sqrt{1 - M_\infty^2}$ as is the pressure coefficient so the lines of constant pressure (and hence density) are ellipses with ratio of axes equal to $\sqrt{1 - M_\infty^2}$ given by the equation

$$\left[\frac{y}{\frac{1}{2 \sqrt{1 - M_\infty^2} \sinh \frac{\pi}{2} \frac{C_p \sqrt{1 - M_\infty^2}}{\theta}}} \right]^2 + \left[\frac{x + \frac{e \frac{\pi C_p \sqrt{1 - M_\infty^2}}{2\theta}}{2 \sinh \frac{\pi C_p \sqrt{1 - M_\infty^2}}{2\theta}}}{\frac{1}{\sinh \frac{\pi}{2} \frac{C_p \sqrt{1 - M_\infty^2}}{\theta}}} \right]^2 = 1 \quad (86)$$

Linearized Supersonic Flow past a Wedge

From the Ackeret theory the pressure coefficient in supersonic flow is proportional to the slope and for the wedge yields simply

$$C_p = \frac{2\theta}{\sqrt{M_\infty^2 - 1}} \quad (87)$$

or

$$\tilde{C}_p \approx \frac{2}{\sqrt{\xi_\infty}} \quad (88)$$

Linearized Subsonic Flow past a Circular-Arc Section

For the circular-arc section, the slope of the surface varies almost linearly with distance from the zero-slope point along the axis of the profile. For the section shown in figure 1 then, with the center line on $y = 0$, the leading edge at $x = 0$, and the zero-slope point at $x = c$, the incompressible-flow problem is again to find an analytic function $u - iv$ such that on $y = 0$, $v = 0$ except for $0 < x < c$

where $v = 2U \frac{t}{c} (1 - \frac{x}{c})$ where t is the half thickness at $x = c$ and $u - iv = 0$ at infinity. Such a function is

$$u - iv = -\frac{2U}{\pi} \frac{t}{c} \left[\left(\frac{z}{c} - 1 \right) \log_e \frac{z/c}{(z/c) - 1} - 1 \right] \quad (89)$$

On the wedge ($y = 0$, $0 < x < c$), then

$$C_{p0} = -\frac{2u}{U} = -\frac{4}{\pi} \frac{t}{c} \left[\left(1 - \frac{x}{c} \right) \log_e \frac{x/c}{1 - (x/c)} + 1 \right] \quad (90)$$

so the linearized subsonic solution is

$$C_p = \frac{-\frac{4}{\pi} \frac{t}{c}}{\sqrt{1 - M_\infty^2}} \left[\left(1 - \frac{x}{c} \right) \log_e \frac{x/c}{1 - (x/c)} + 1 \right] \quad (91)$$

or

$$\tilde{C}_p = \frac{4}{\pi \sqrt{1 - \xi_\infty}} \left[\left(1 - \frac{x}{c} \right) \log_e \frac{x/c}{1 - (x/c)} + 1 \right] \quad (92)$$

The minimum C_p is obtained by differentiation, and one finds that

$$\frac{dC_p}{d(x/c)} = 0$$

at the point where $\log_e \frac{x/c}{1 - (x/c)} = \frac{1}{x/c}$ and numerically the solution of this transcendental equation is

$$\frac{x}{c} = 0.783 \quad (93)$$

which gives

$$C_{pmin} = \frac{-1.626 (t/c)}{\sqrt{1 - M_\infty^2}} \quad (94)$$

Linearized Supersonic Flow past a Circular-Arc Section

The result here is again simple from the Ackeret theory:

$$C_p = \frac{4(t/c)}{\sqrt{M_\infty^2 - 1}} \left(1 - \frac{x}{c}\right) \quad (95)$$

or

$$\tilde{C}_p = \frac{4}{\sqrt{\xi_\infty}} \left(1 - \frac{x}{c}\right) \quad (96)$$

APPENDIX C

TRANSONIC SHOCK POLAR

The equation of the shock polar in the hodograph plane is

$$v^2 = (U - \bar{u})^2 \frac{\frac{\bar{u}}{a^*} - \frac{a^*}{U}}{\frac{a^*}{U} + \frac{2}{\gamma + 1} \frac{U}{a^*} - \frac{\bar{u}}{a^*}} \quad (97)$$

where U is the velocity ahead of the shock and \bar{u} and \bar{v} are velocity components behind the shock parallel and perpendicular to the direction of U , respectively. Making the transonic approximation in this equation let

$$\left. \begin{aligned} \bar{u} &= a^* + u \\ \bar{v} &= v \\ U &= a^* + u_\infty \end{aligned} \right\} \quad (98)$$

Substituting into equation (97), neglecting higher powers of the perturbation velocities, one obtains

$$v^2 = \frac{\gamma + 1}{2} (u_\infty - u)^2 \left(\frac{u}{a^*} + \frac{u_\infty}{a^*} \right) \quad (99)$$

Letting

$$\left. \begin{aligned} u' &= (\gamma + 1) \frac{u}{a^*} \\ v' &= (\gamma + 1) \frac{v}{a^*} \end{aligned} \right\} \quad (100)$$

one then has

$$2(v')^2 = (u_\infty' - u')^2 (u' + u_\infty') \quad (101)$$

The wedge angle for detachment of the shock will now be given by the maximum value of v' . This is easily seen to occur at $u' = -\frac{1}{3} u_{\infty}'$ giving $v_{\max}' = \frac{4}{9} \sqrt{3} u_{\infty}'^{3/2}$. Since within the transonic approximation

$$v' = (\gamma + 1)\theta$$

on the wedge and

$$u_{\infty}' \approx M_{\infty}^2 - 1 \quad (102)$$

this implies that

$$(\gamma + 1)\theta_{\max} \approx \frac{4}{3^{3/2}} (M_{\infty}^2 - 1)^{3/2} \quad (103)$$

or, viewed in another light, this implies that the reduced attachment Mach number is

$$\xi_{\infty A} = \frac{M_{\infty A}^2 - 1}{[(\gamma + 1)\theta]^{2/3}} = \frac{3}{4^{2/3}} = 1.19 \quad (104)$$

Similarly, the wedge angle for obtaining exactly sonic velocity behind the shock is given by the value of v' where $u' = 0$. This is

$v' = \frac{1}{\sqrt{2}} (u_{\infty}')^{3/2}$. Again using equation (102) this can be written

$$(\gamma + 1)\theta_s \approx \frac{1}{\sqrt{2}} (M_{\infty}^2 - 1)^{3/2} \quad (105)$$

and, viewed in another light, this implies that the reduced Mach number for which sonic velocity is obtained behind the shock on a wedge is

$$\xi_{\infty S} = \frac{M_{\infty S} - 1}{[(\gamma + 1)\theta]^{2/3}} = 2^{1/3} = 1.26 \quad (106)$$

APPENDIX D

VARIATION OF REDUCED MACH NUMBER AT WHICH SONIC VELOCITY OCCURS
BEHIND AN OBLIQUE SHOCK WITH FLOW-DEFLECTION ANGLE

The oblique-shock relations can be written

$$M_2^2 = \frac{1 + \frac{\gamma - 1}{2} M_1^2}{\gamma M_1^2 \sin^2 \beta - \frac{\gamma - 1}{2}} + \frac{M_1^2 \cos^2 \beta}{1 + \frac{\gamma - 1}{2} M_1^2 \sin^2 \beta} \quad (107)$$

$$\tan \theta = 2 \cot \beta \frac{M_1^2 \sin^2 \beta - 1}{M_1^2 (\gamma + \cos 2\beta) + 2} \quad (108)$$

where

M_1 Mach number ahead of shock

M_2 Mach number behind shock

β shock-wave angle

θ flow deflection

For $M_2 = 1$, eliminating β between these two equations yields

$$\tan \theta = \frac{f(M_1)}{\gamma M_1^2 - f(M_1)} \sqrt{\frac{M_1^2 - 1 + \frac{\gamma + 1}{2\gamma} f(M_1)}{1 + \frac{\gamma + 1}{2\gamma} f(M_1)}} \quad (109)$$

where

$$f(M_1) = \frac{M_1^2 - 1}{1} - 1 + \sqrt{1 + \frac{\gamma - 1}{\gamma + 1} (M_1^2 - 1) + \left(\frac{M_1^2 - 1}{2}\right)^2}$$

Expanding the right-hand side in powers of $M_1^2 - 1$ (assumed small), one obtains

$$(\gamma + 1) \tan \theta = \frac{(M_1^2 - 1)^{3/2}}{2^{1/2}} \left[1 - \frac{19\gamma + 2}{16(\gamma + 1)} (M_1^2 - 1) + \dots \right] \quad (110)$$

Reverting this series and letting $\theta \approx \tan \theta$ and $M_1 = M_{\infty S}$, one finds

$$\xi_{\infty S} = \frac{M_{\infty S}^2 - 1}{[(\gamma + 1)\theta]^{2/3}} = 2^{1/3} \left[1 + \frac{19\gamma + 2}{24 \left(\frac{\gamma + 1}{2}\right)^{1/3}} \theta^{2/3} + o(\theta^{4/3}) \right] \quad (111)$$

For $\gamma = 1.4$,

$$\frac{19\gamma + 2}{24 \left(\frac{\gamma + 1}{2}\right)^{1/3}} = 1.122$$

APPENDIX E

VARIATION OF REDUCED MACH NUMBER BEHIND A PRANDTL-MEYER

EXPANSION FROM $M = 1$ THROUGH AN ANGLE θ , WITH θ

The exact relation here is

$$\theta = \sqrt{\frac{\gamma+1}{\gamma-1}} \tan^{-1} \sqrt{\frac{\gamma-1}{\gamma+1}} \sqrt{M_{PM}^2 - 1} - \tan^{-1} \sqrt{M_{PM}^2 - 1} \quad (112)$$

Expanding the right-hand side in terms of $\sqrt{M_{PM}^2 - 1}$, using

$$\tan^{-1} x = x - \frac{x^3}{3} + \frac{x^5}{5} - \frac{x^7}{7} + \dots$$

one obtains

$$(\gamma+1)\theta = \frac{2}{3} (M_{PM}^2 - 1)^{3/2} \sum_{n=1}^{\infty} \frac{(-1)^n a_n (M_{PM}^2 - 1)^n}{1 + \frac{2n}{3}} \quad (113)$$

where

$$a_n = \frac{\gamma+1}{2} \left[1 - \left(\frac{\gamma-1}{\gamma+1} \right)^{n+1} \right]$$

Reverting this series the first few terms are

$$M_{PM}^2 - 1 = \left[\frac{3(\gamma+1)}{2} \theta \right]^{3/2} \left\{ 1 + \frac{4\gamma}{5(\gamma+1)} \left[\frac{3(\gamma+1)}{2} \theta \right]^{2/3} + o(\theta^{4/3}) \right\} \quad (114)$$

Therefore,

$$\xi_{PM} = \frac{M_{PM}^2 - 1}{[(\gamma + 1)\theta]^{2/3}} = \left(\frac{3}{2}\right)^{2/3} \left\{ 1 + \frac{4\gamma}{5(\gamma + 1)} \left[\frac{3(\gamma + 1)}{2}\right]^{2/3} \theta^{2/3} + o(\theta^{4/3}) \right\} \quad (115)$$

For $\gamma = 1.4$,

$$\frac{4\gamma}{5(\gamma + 1)} \left[\frac{3(\gamma + 1)}{2}\right]^{2/3} = 1.097$$

REFERENCES

1. Weaver, John H.: A Method of Wind-Tunnel Testing through the Transonic Range. Jour. Aero. Sci., vol. 15, no. 1, Jan. 1948, pp. 28-34.
2. Ackeret, J., Feldman, F., and Rott, N.: Investigations of Compression Shocks and Boundary Layers in Gases Moving at High Speed. NACA TM 1113, 1947.
3. Liepmann, Hans Wolfgang: The Interaction between Boundary Layer and Shock Waves in Transonic Flow. Jour. Aero. Sci., vol. 13, no. 12, Dec. 1946, pp. 623-637.
4. Guderley, G.: On the Transition from a Transonic Potential Flow to a Flow with Shocks. Tech. Rep. No. F-TR-2160-ND, Air Materiel Command, Army Air Forces, Aug. 1947.
5. Ferri, Antonio: Elements of Aerodynamics of Supersonic Flows. The Macmillan Co., 1949.
6. Sears, W. R.: Transonic Potential Flow of a Compressible Fluid. Jour. Appl. Phys., vol. 21, no. 8, Aug. 1950, pp. 771-778.
7. Kuo, Yung-Huai: On the Stability of Two-Dimensional Smooth Transonic Flows. Jour. Aero. Sci., vol. 18, no. 1, Jan. 1951, pp. 1-6, 54.
8. Liepmann, Hans Wolfgang, Ashkenas, Harry, and Cole, Julian D.: Experiments in Transonic Flow. Tech. Rep. No. 5667, Air Materiel Command, U. S. Air Force, Feb. 1948.
9. Von Kármán, Th.: The Similarity Law of Transonic Flow. Jour. Math. and Phys., vol. 26, no. 3, Oct. 1947, pp. 182-190.
10. Busemann, Adolf: A Review of Analytical Methods for the Treatment of Flows with Detached Shocks. NACA TN 1858, 1949.
11. Busemann, Adolf: The Drag Problem at High Subsonic Speeds. Jour. Aero. Sci., vol. 16, no. 6, June 1949, pp. 337-344.
12. Guderley, K. Gottfried: Considerations of the Structure of Mixed Subsonic-Supersonic Flow Patterns. Tech. Rep. No. F-TR-2168-ND, Air Materiel Command, Army Air Forces, Oct. 1947.
13. Guderley, K. Gottfried: Singularities at the Sonic Velocity. Tech. Rep. No. F-TR-1171-ND, Air Materiel Command, Army Air Forces, June 1948.

14. Frankl, F.: On the Problems of Chaplygin for Mixed Sub- and Supersonic Flows. NACA TM 1155, 1947.
15. Maccoll, J. W., and Codd, J.: Theoretical Investigations of the Flow around Various Bodies in the Sonic Region of Velocities. Theoretical Res. Rep. No. 17/45, Armament Res. Dept., British Ministry of Supply, Sept. 1945.
16. Emmons, Howard W.: The Theoretical Flow of a Frictionless, Adiabatic, Perfect Gas inside of a Two-Dimensional Hyperbolic Nozzle. NACA TN 1003, 1946.
17. Emmons, Howard W.: Flow of a Compressible Fluid past a Symmetrical Airfoil in a Wind Tunnel and in Free Air. NACA TN 1746, 1948.
18. Drougge, G.: The Flow around Conical Tips in the Upper Transonic Range. Rep. No. 25, The Aero. Res. Inst. of Sweden (Stockholm), 1948.
19. Drebinger, J. W.: Detached Shock Waves. Ph. D. Thesis, Harvard Univ., May 1950.
20. Guderley, G., and Yoshihara, H.: The Flow over a Wedge Profile at Mach Number One. Jour. Aero. Sci., vol. 17, no. 11, Nov. 1950, pp. 723-736.
21. Vincenti, Walter G., and Wagoner, Cleo B.: Transonic Flow past a Wedge Profile with Detached Bow Wave - General Analytical Method and Final Calculated Results. NACA TN 2339, 1951.
22. Cole, J. D.: Drag of a Finite Wedge at High Subsonic Speeds. Jour. Math. and Phys., vol. 30, no. 2, July 1951, pp. 79-93.
23. Pack, D. C.: Investigation of the Flow past Finite Wedges of 20 deg. and 40 deg. Apex Angle at Subsonic and Supersonic Speeds, using a Mach-Zehnder Interferometer. R. & M. No. 2321, British A.R.C., 1946.
24. Griffith, Wayland C.: Transonic Flow. Tech. Rep. II-7, Contract N6ori-105, Task II, Project NRO61-020, Office of Naval Research and Dept. of Phys., Princeton Univ., Dec. 19, 1950.
25. Liepmann, H. W., and Bryson, A. E., Jr.: Transonic Flow past Wedge Sections. Jour. Aero. Sci., vol. 17, no. 12, Dec. 1950, pp. 745-755.
26. Dhawan, Satish, and Roshko, Anatol: A Flexible Nozzle for a Small Supersonic Wind Tunnel. Jour. Aero. Sci., vol. 18, no. 4, April 1951, pp. 253-258.

27. Ashkenas, H. I.: Design and Construction of a Mach-Zehnder Interferometer for Use with the GALCIT Transonic Wind Tunnel. A.E. Thesis, C.I.T., 1949.
28. Ashkenas, Harry I., and Bryson, Arthur E.: Design and Performance of a Simple Interferometer for Wind-Tunnel Measurements. Jour. Aero. Sci., vol. 18, no. 2, Feb. 1951, pp. 82-90.
29. Tsien, H. S., and Baron, J.: Airfoils in Slightly Supersonic Flow. Jour. Aero. Sci., vol. 16, no. 1, Jan. 1949, pp. 55-61.
30. Nagamatsu, Henry T.: Theoretical Investigation of Detached Shock Waves. Ph. D. Thesis, C.I.T., 1949.
31. Graham, Donald J., Nitzberg, Gerald E., and Olson, Robert N.: A Systematic Investigation of Pressure Distributions at High Speeds over Five Representative NACA Low-Drag and Conventional Airfoil Sections. NACA Rep. 832, 1945.
32. Nitzberg, Gerald E., and Crandall, Stewart: A Study of Flow Changes Associated with Airfoil Section Drag Rise at Supercritical Speeds. NACA TN 1813, 1949.
33. Liepmann, H. W.: On the Relation between Wave Drag and Entropy Increase. Rep. No. SM-13726, Douglas Aircraft Co., Inc., March 16, 1950.
34. Watson, G. N.: A Treatise on the Theory of Bessel Functions. Second ed., The Univ. Press (Cambridge), 1944.

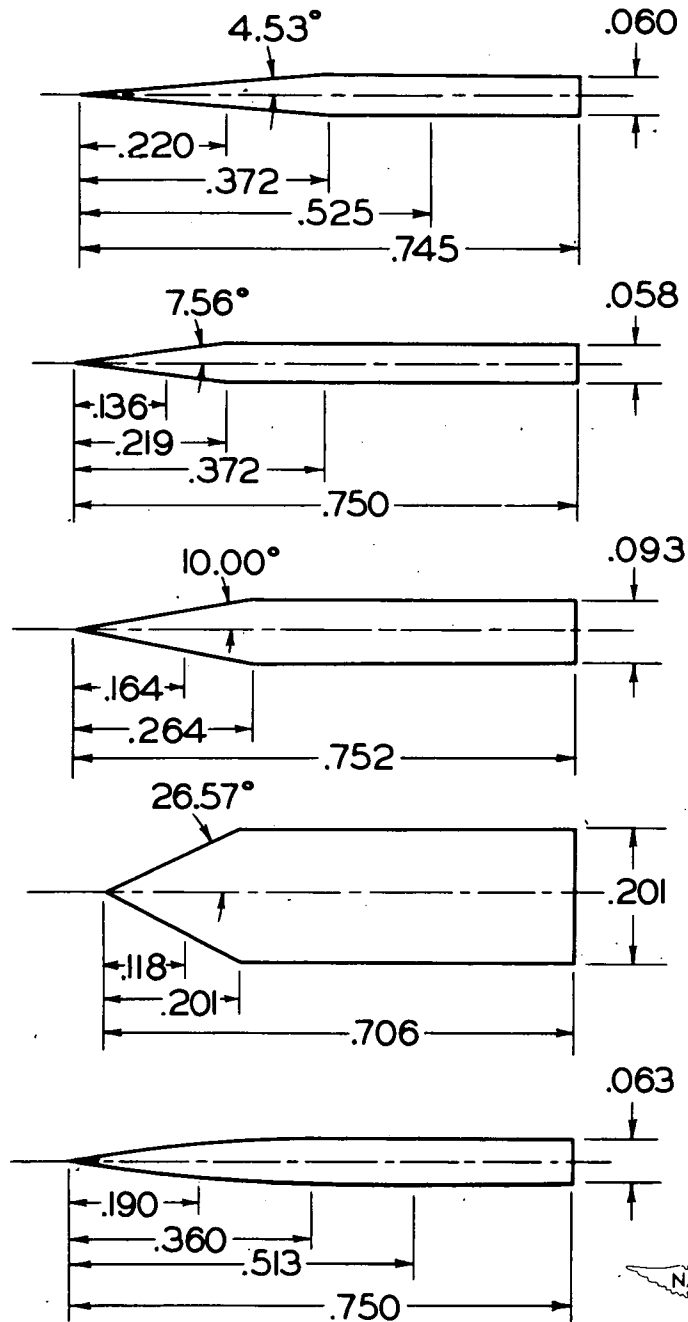


Figure 1.- Geometry of sections tested. All dimensions are in inches.

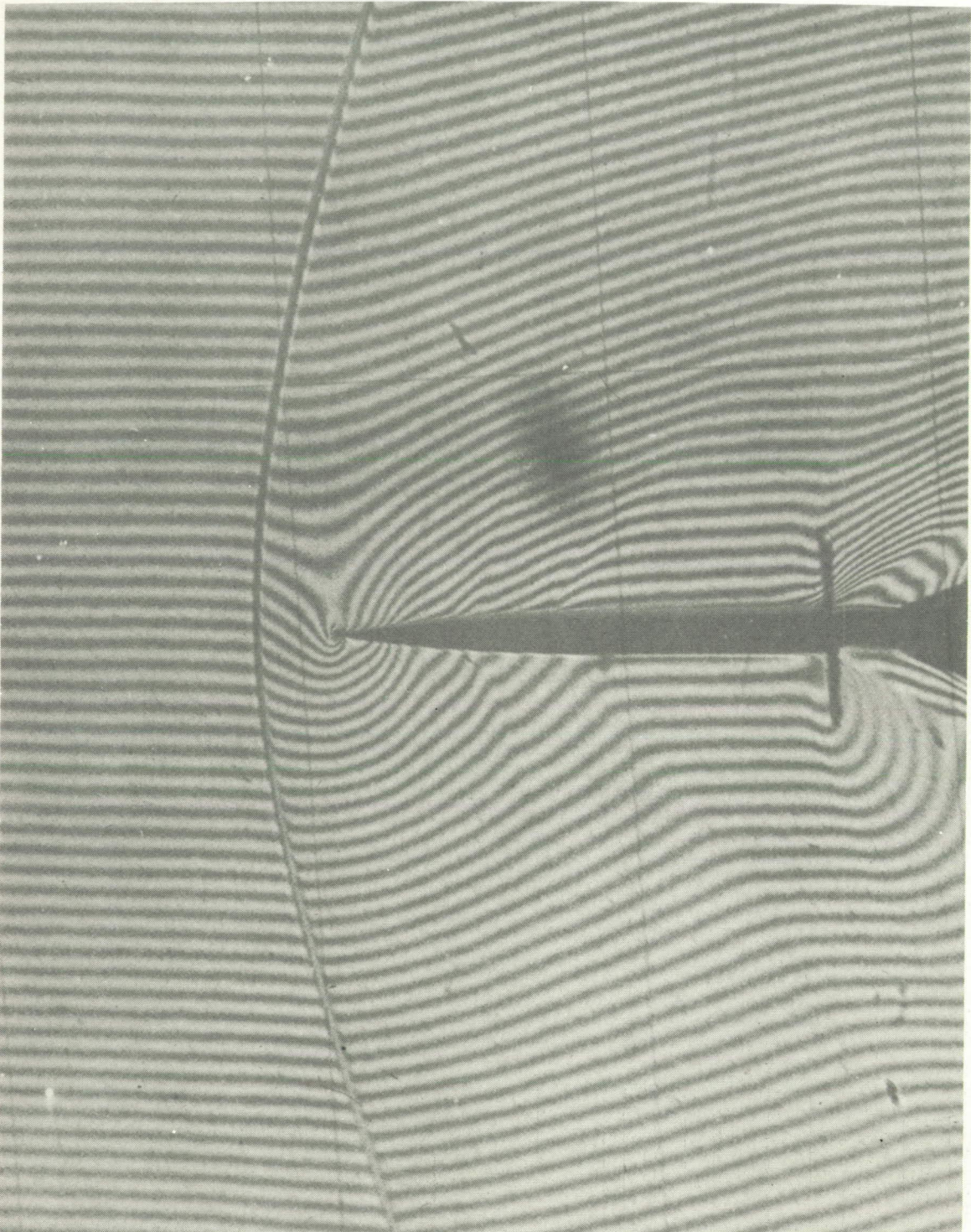


Figure 2.- Typical finite-fringe interferogram. 8.8-percent circular-arc section at $M = 1.200$.

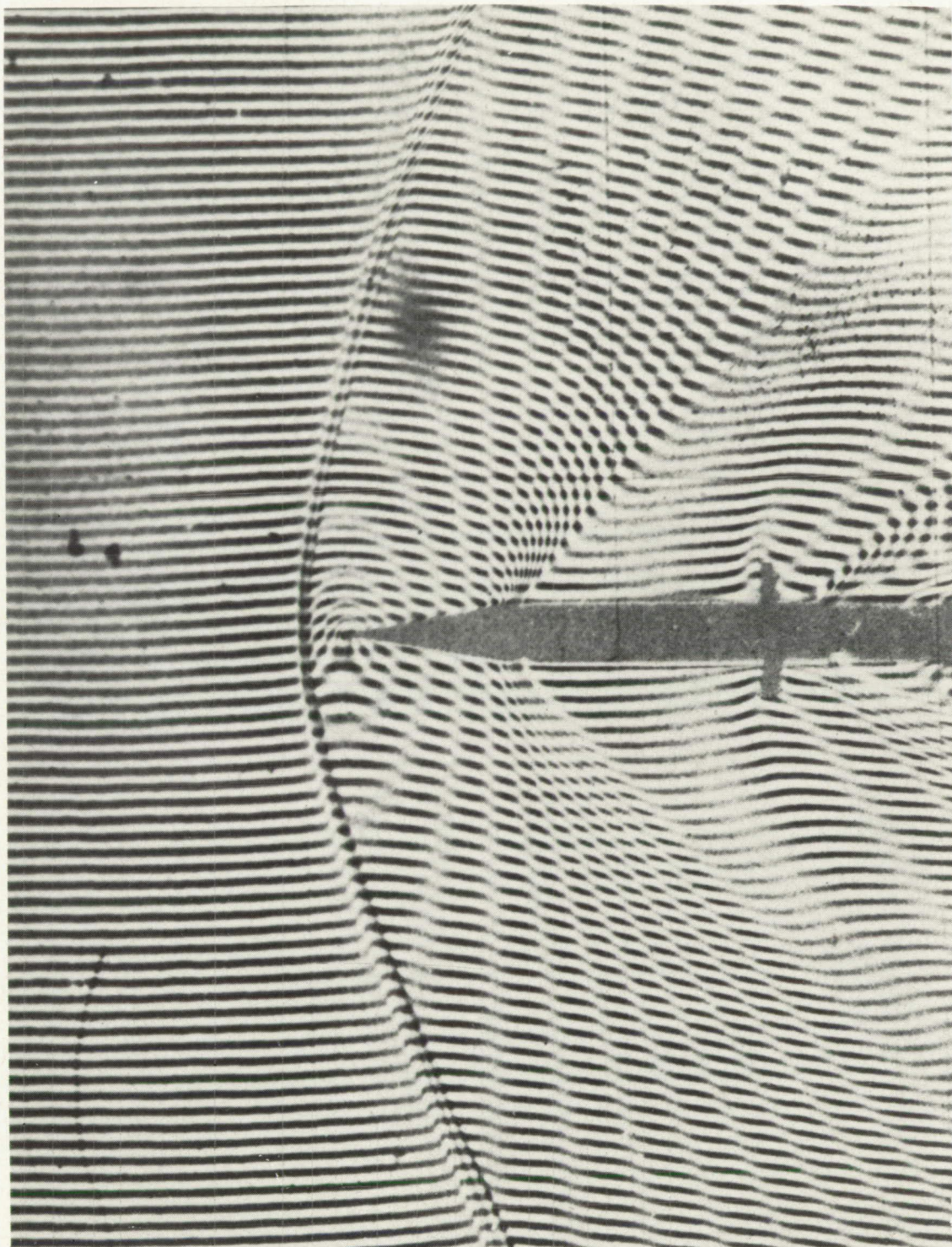


Figure 3.- Typical superimposed finite-fringe interferogram. 10° semi-angle wedge at $M = 1.278$.

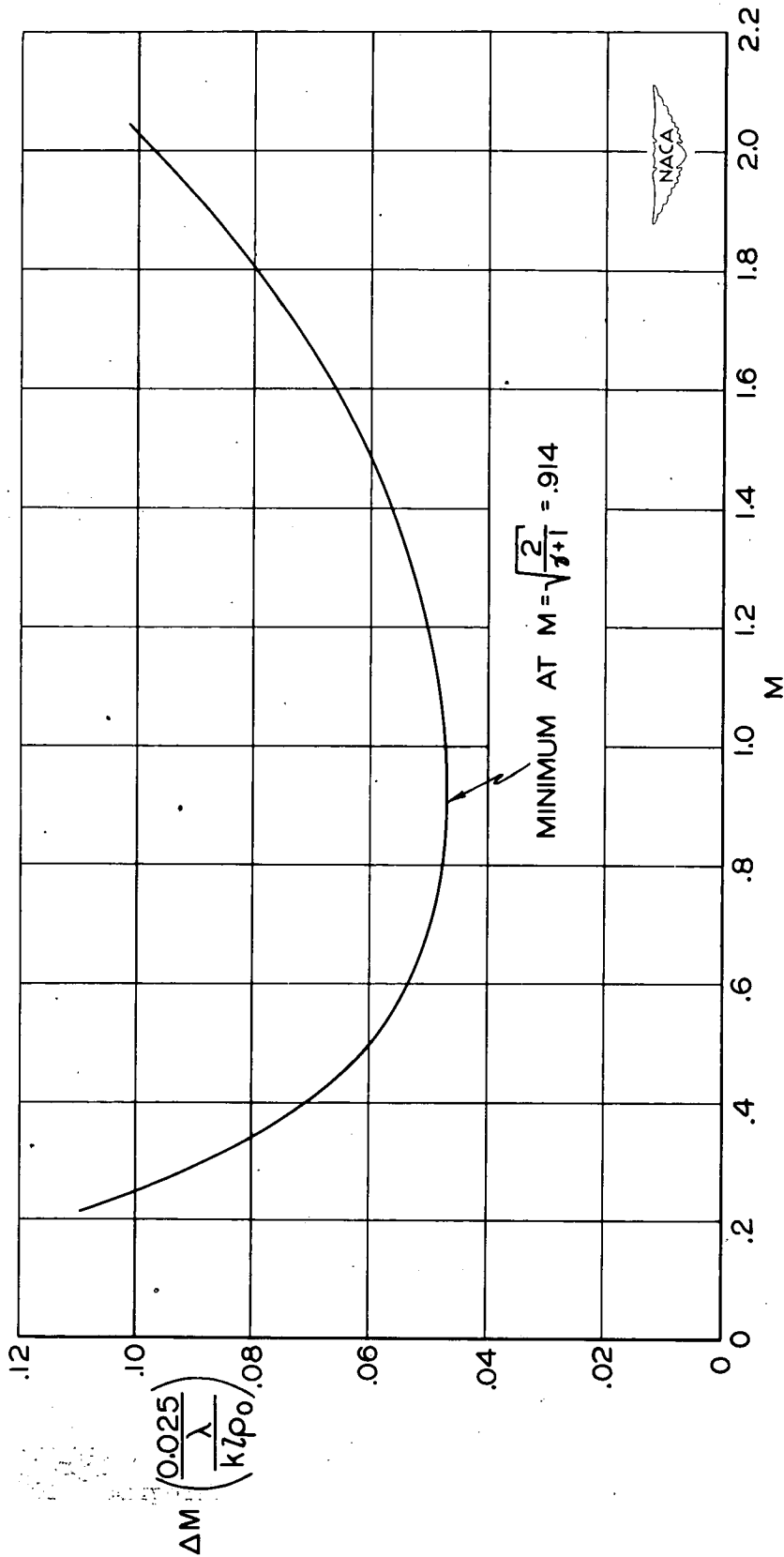


Figure 4.- Increment in Mach number per fringe contour against local Mach number for air ($\gamma = 1.4$). For these tests $\lambda/k\lambda\rho_0 = 0.025 \pm 0.001$.

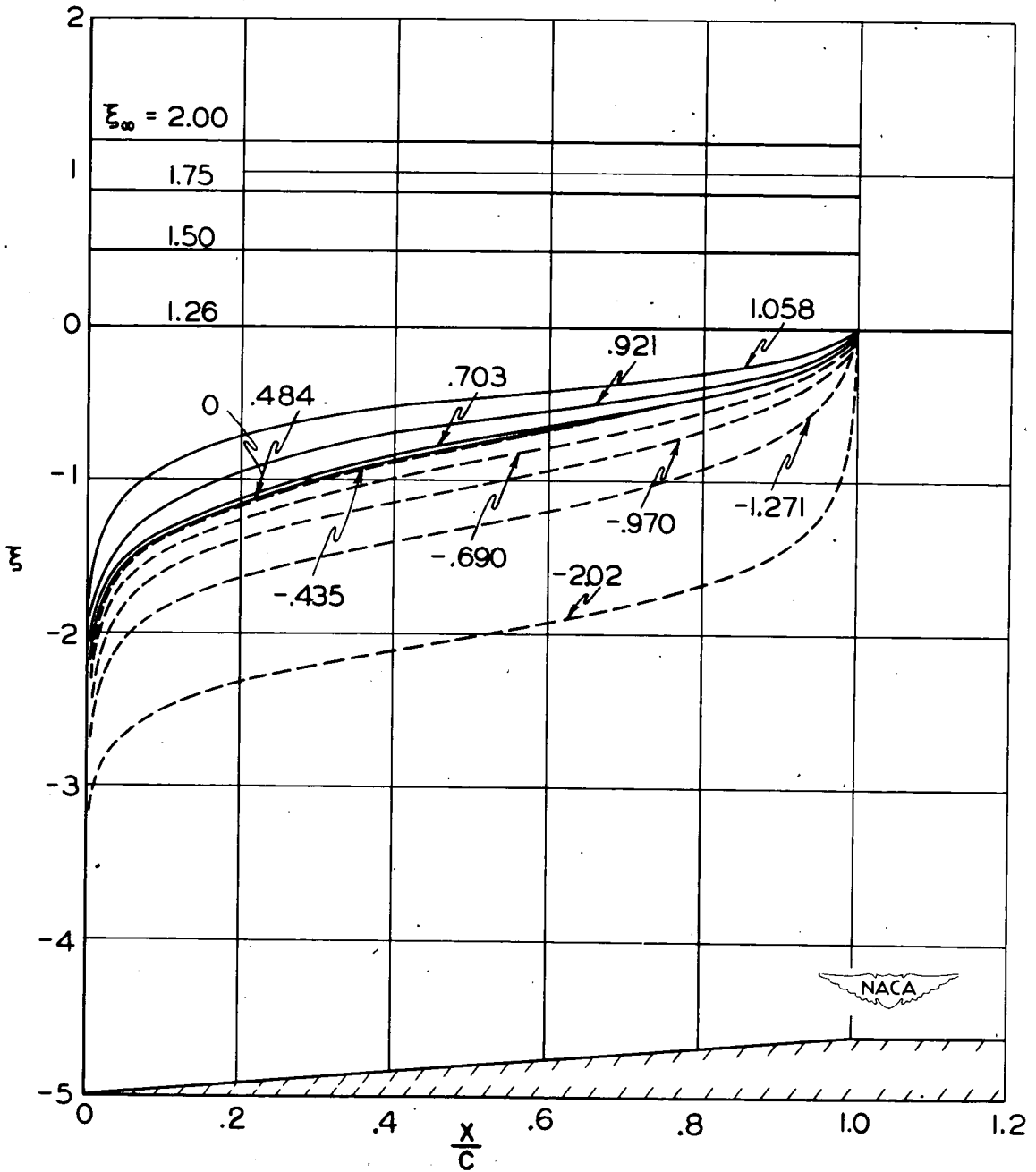


Figure 5.- Theoretical reduced local Mach number distributions on a wedge near Mach number 1. Data from references 20 to 22 and 29.

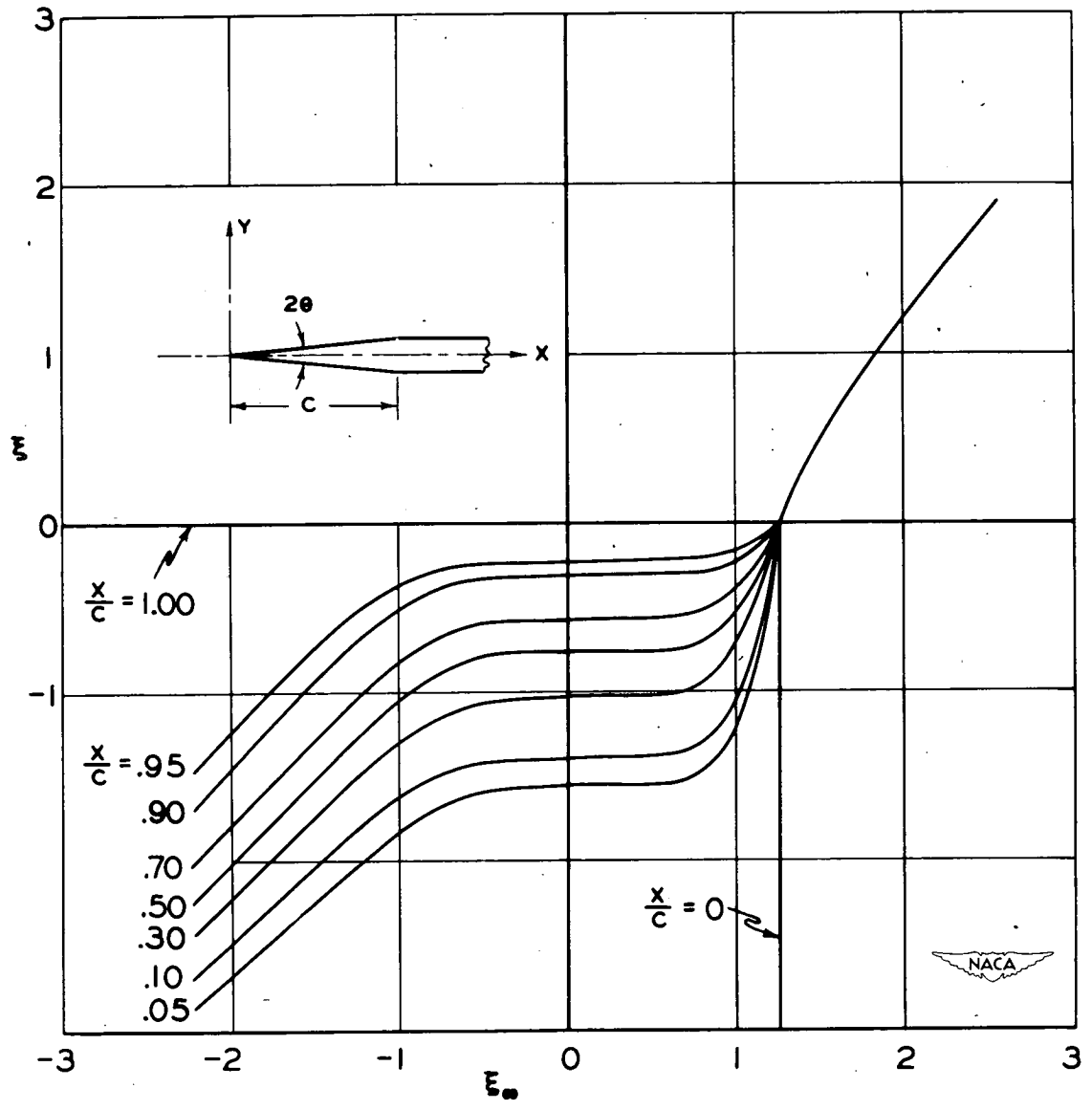


Figure 6.- Theoretical reduced local Mach number against reduced free-stream Mach number at several chordwise stations on a wedge. Data from references 20 to 22 and 29.

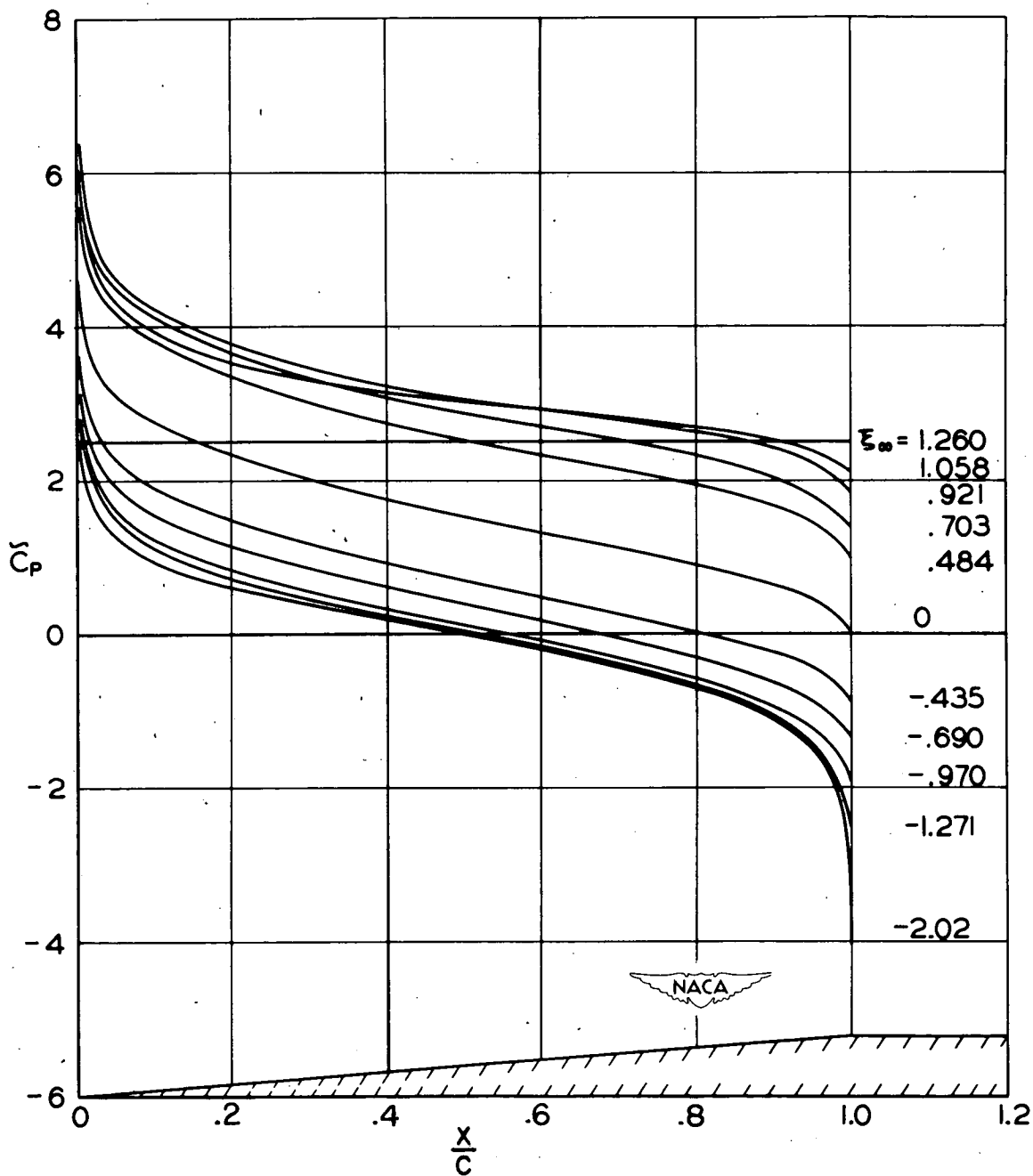


Figure 7.- Theoretical reduced pressure-coefficient distributions on a wedge near Mach number 1. Data from references 20 to 22 and 29.

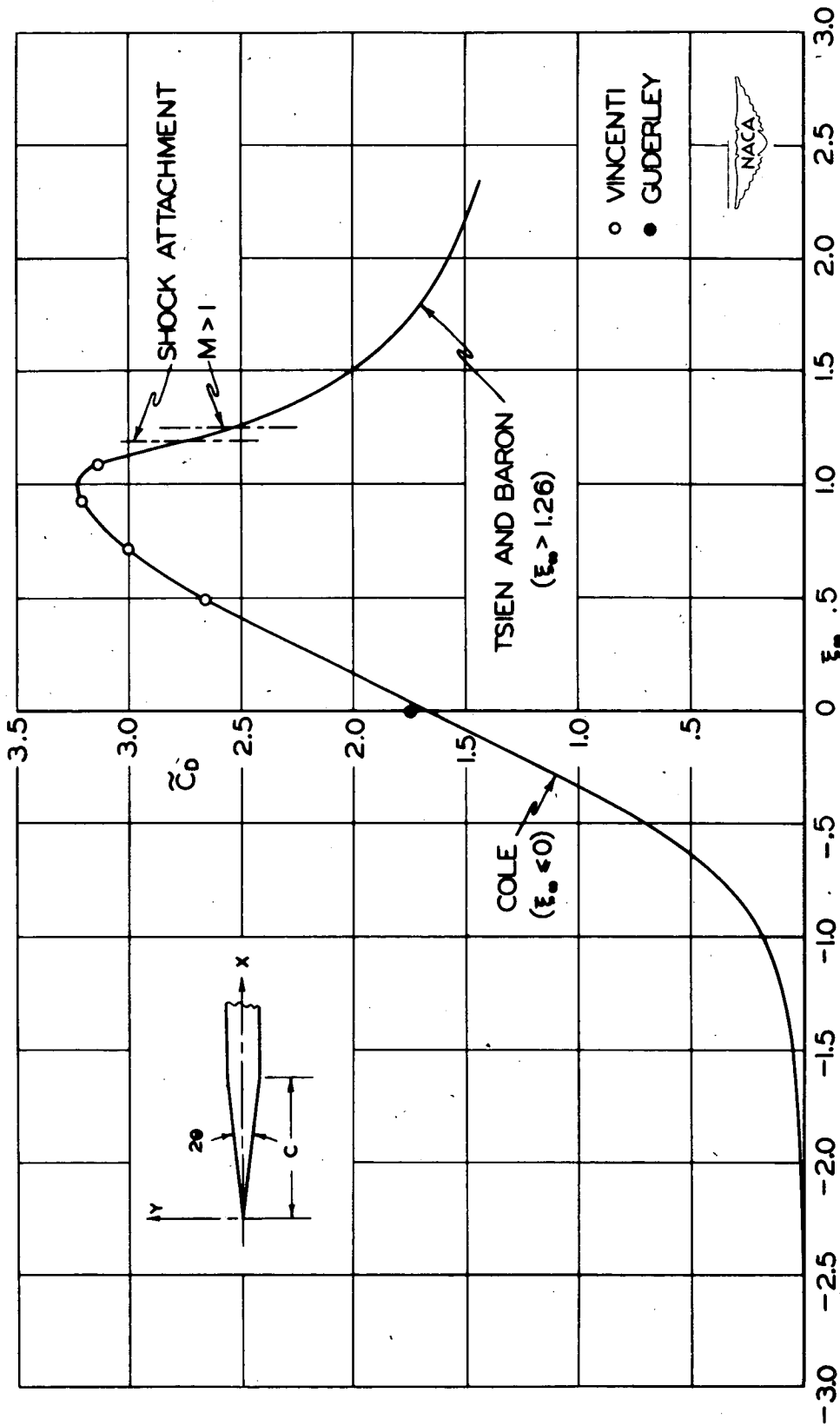


Figure 8.- Theoretical reduced drag coefficient against reduced Mach number for a wedge.

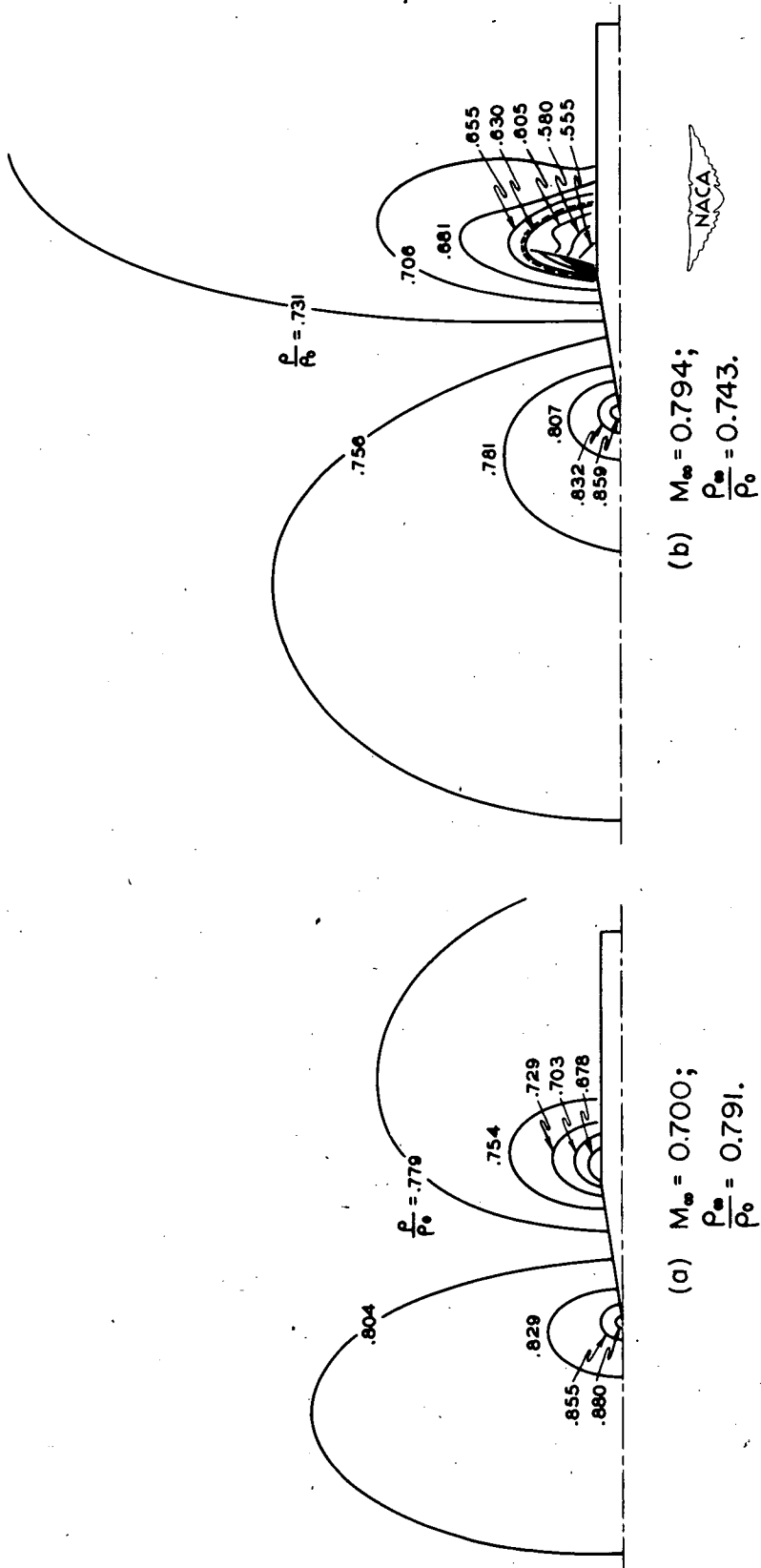
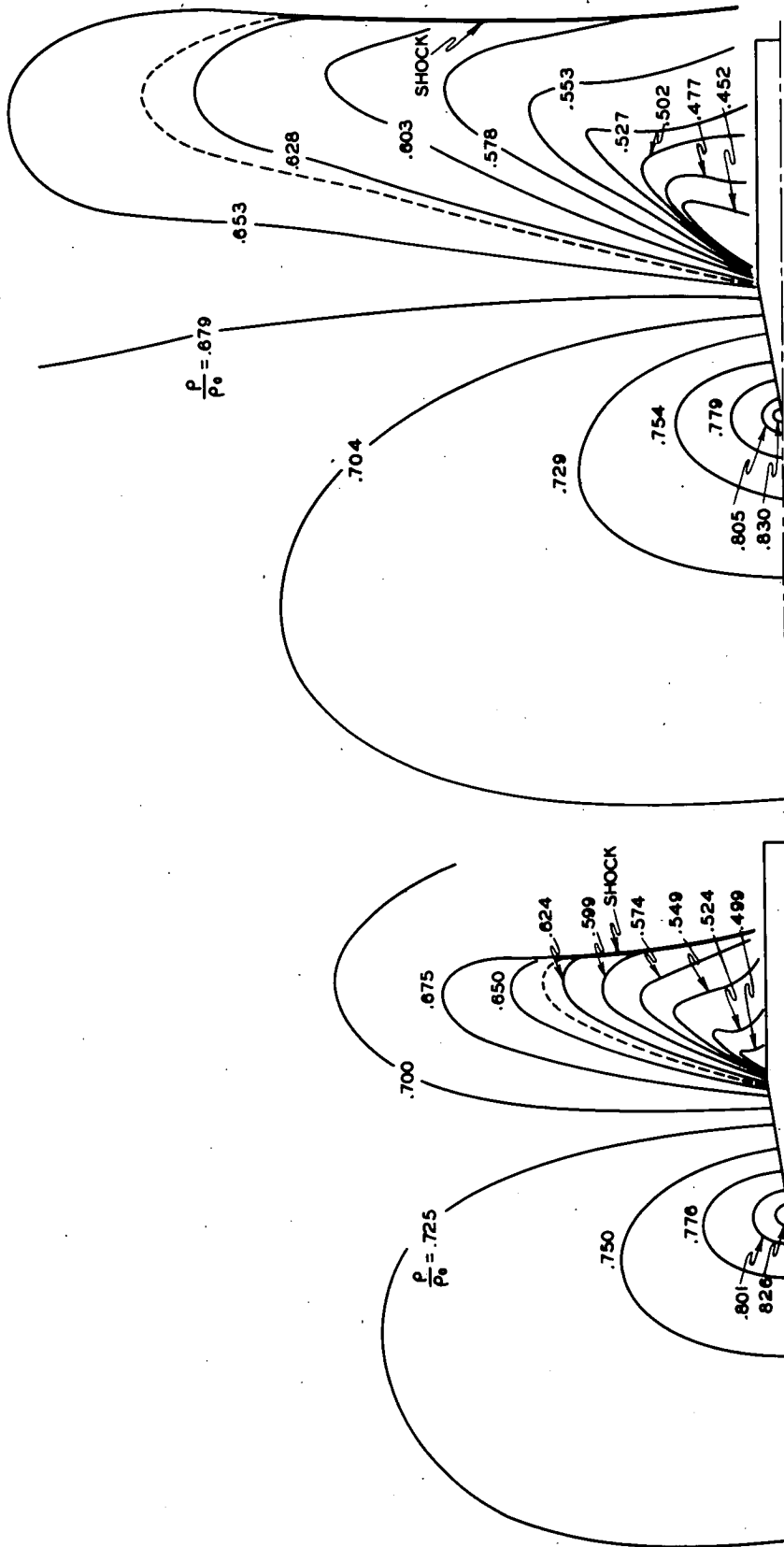


Figure 9.- Interferograms of flow past 10° semiangle wedge for various Mach numbers.



(d) $M_\infty = 0.892$;
 $\frac{p_\infty}{p_0} = 0.691$.

(c) $M_\infty = 0.852$;
 $\frac{p_\infty}{p_0} = 0.712$.

Figure 9.- Continued.

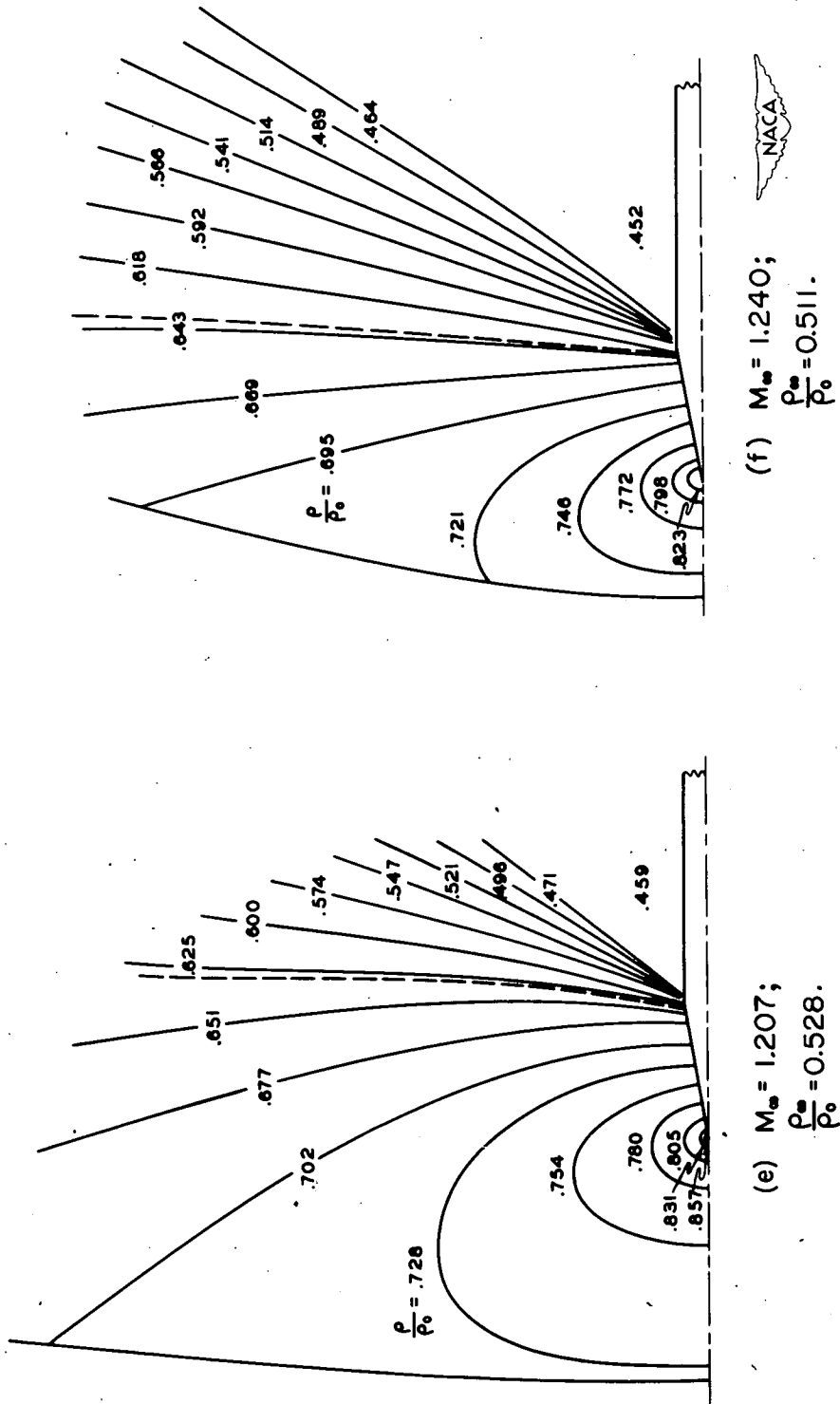
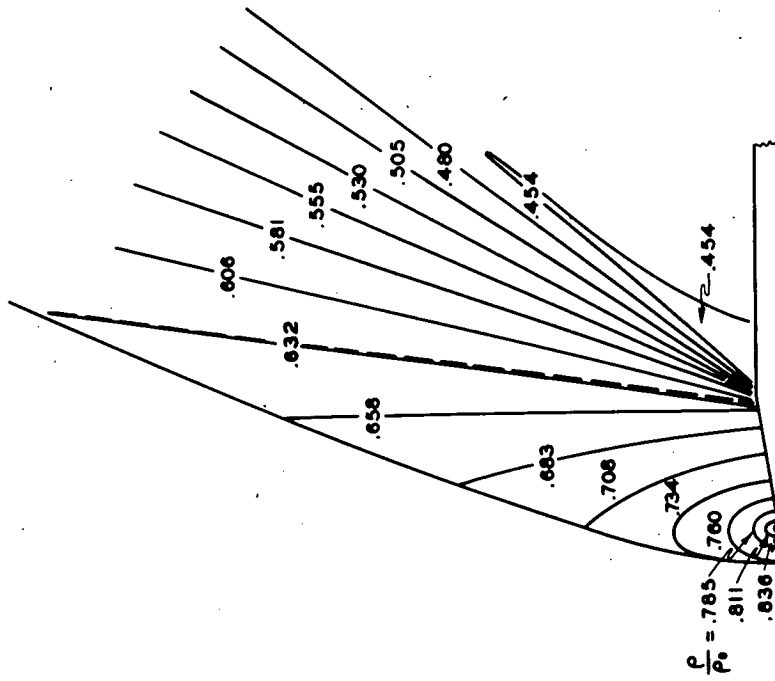
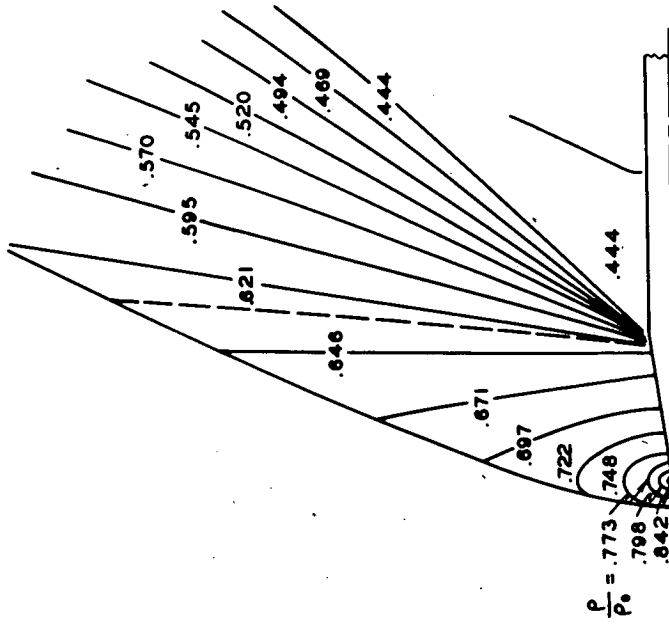


Figure 9.- Continued.



(g) $M_\infty = 1.278$;
 $\frac{p_0}{p_0} = 0.493$.



(h) $M_\infty = 1.315$;
 $\frac{p_0}{p_0} = 0.476$.

Figure 9.- Continued.

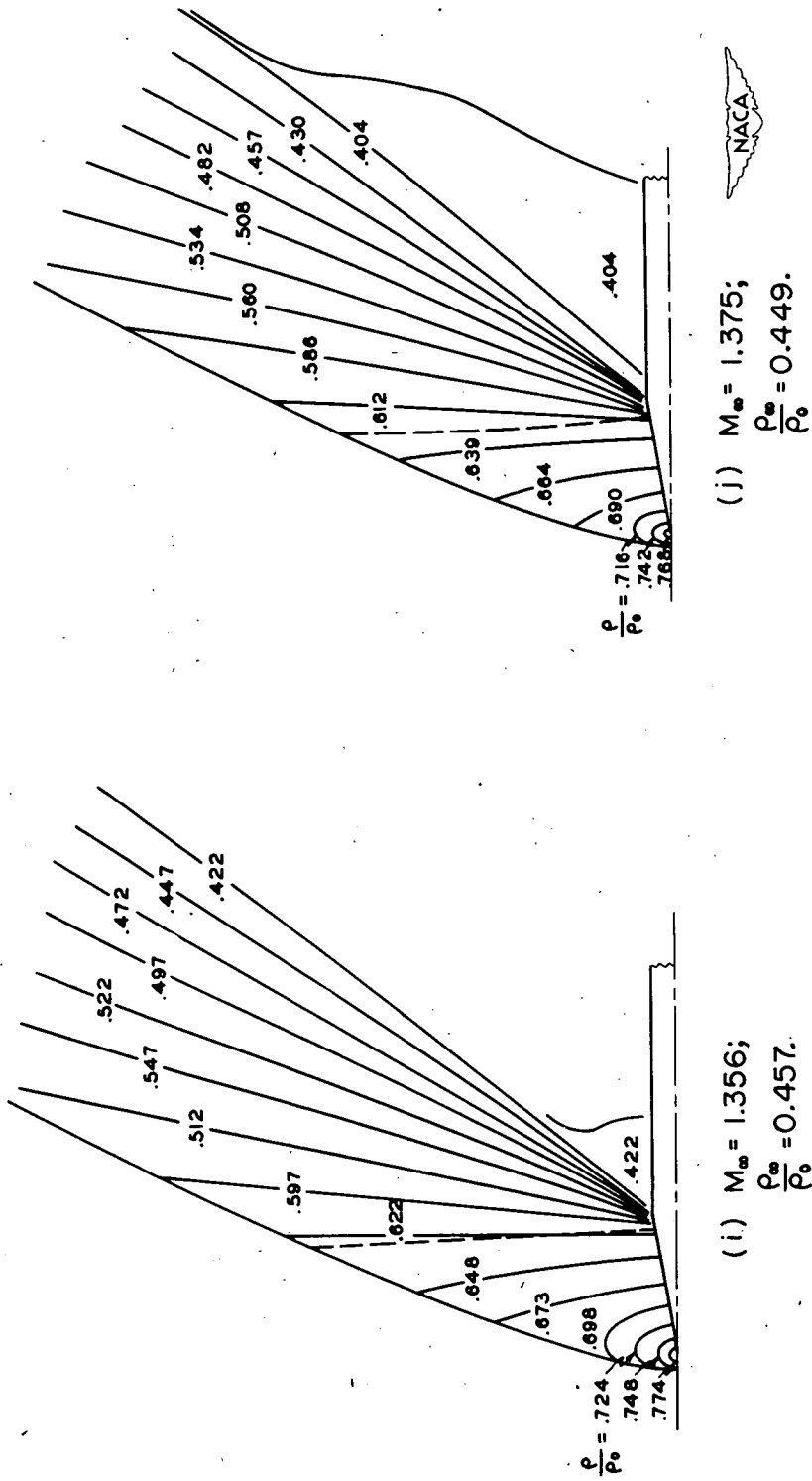


Figure 9.- Continued.

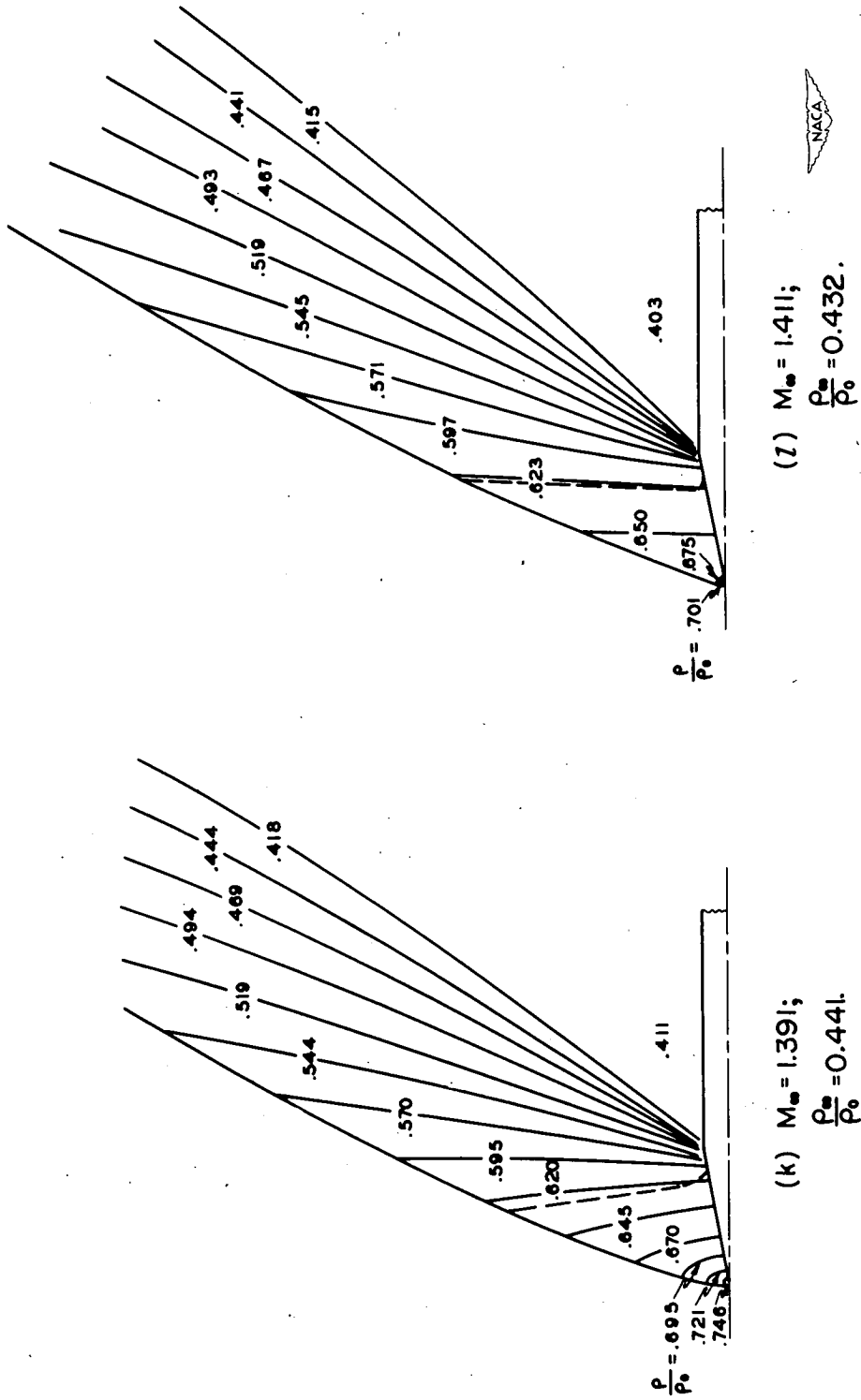


Figure 9.- Continued.

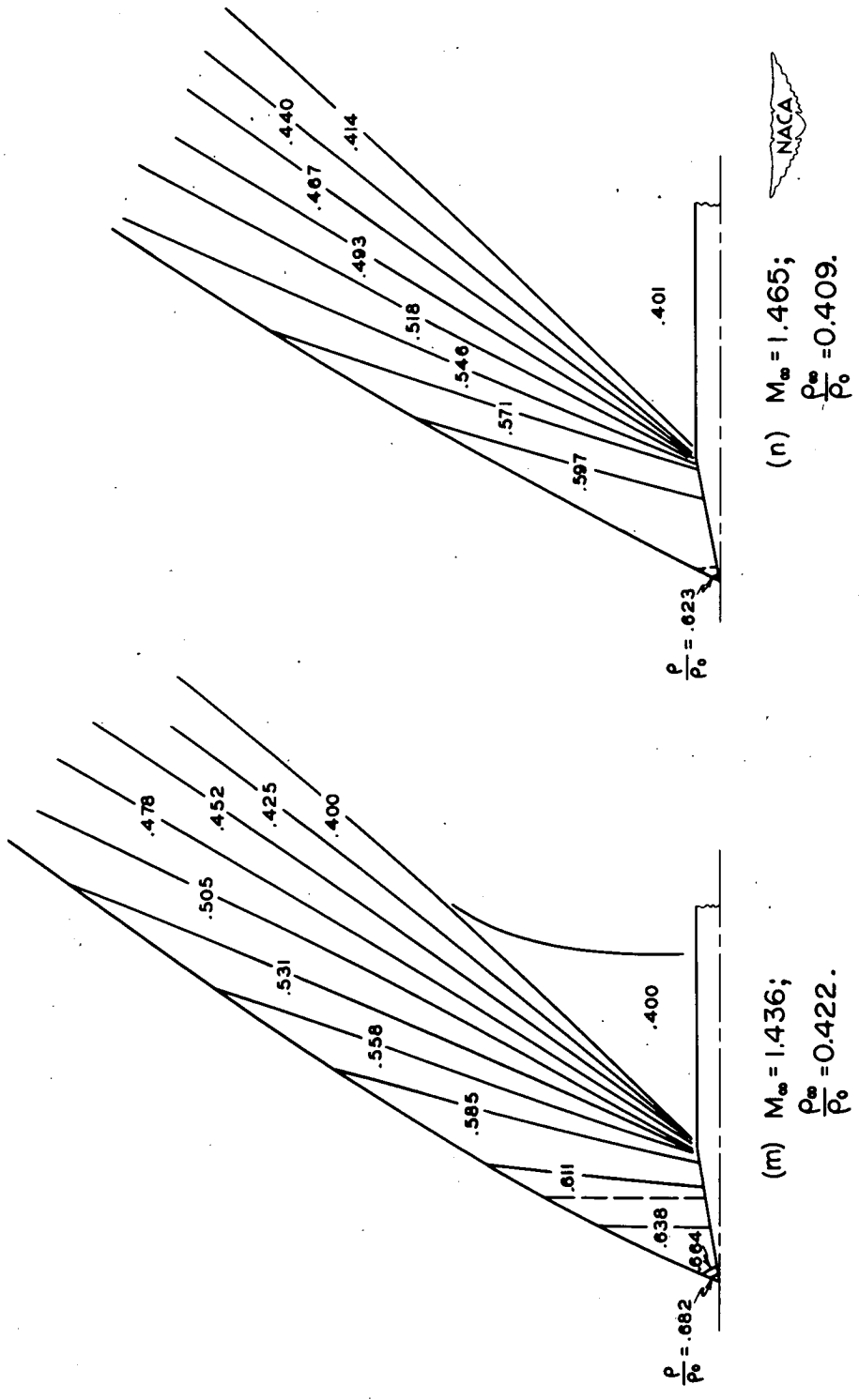
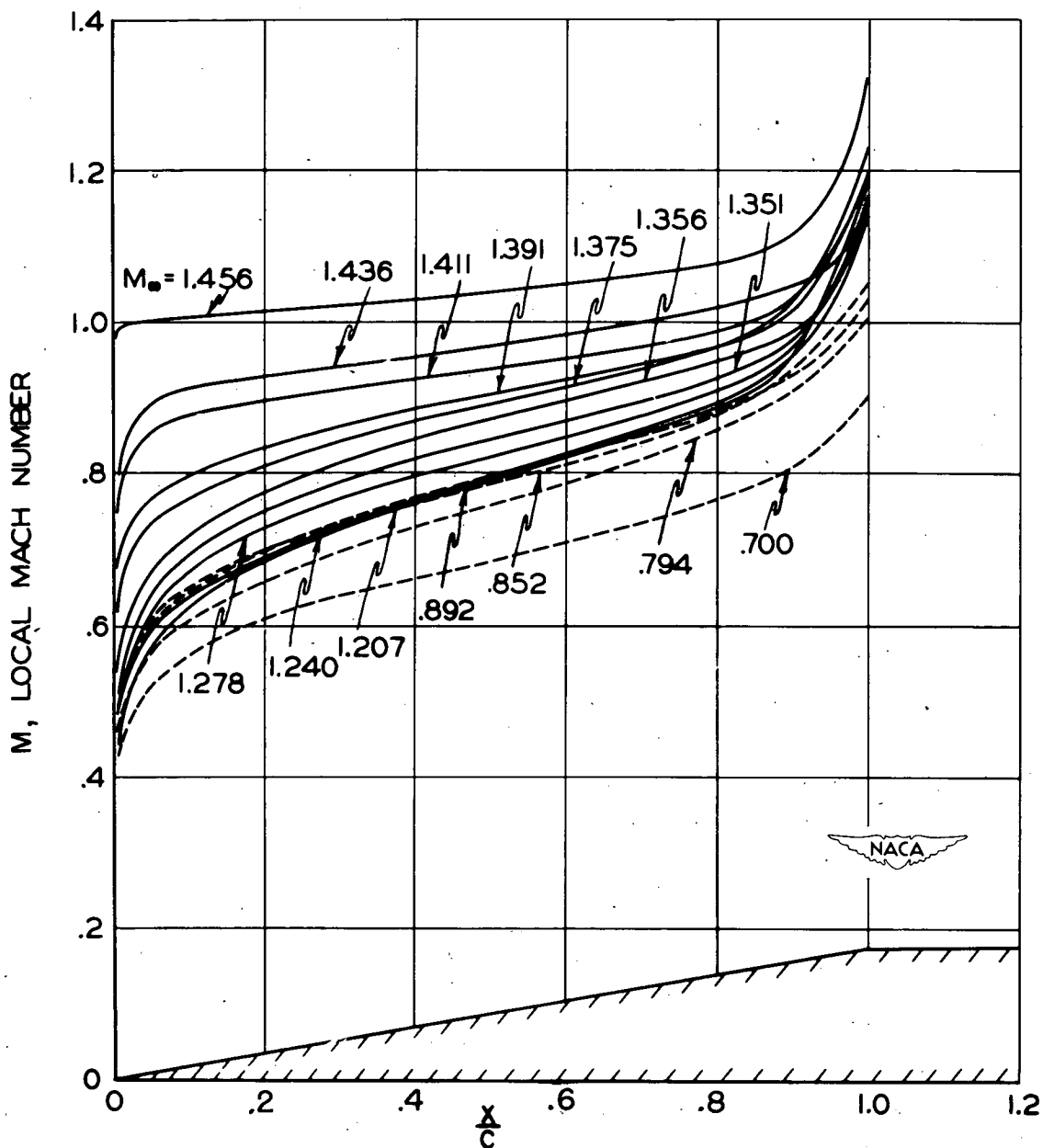
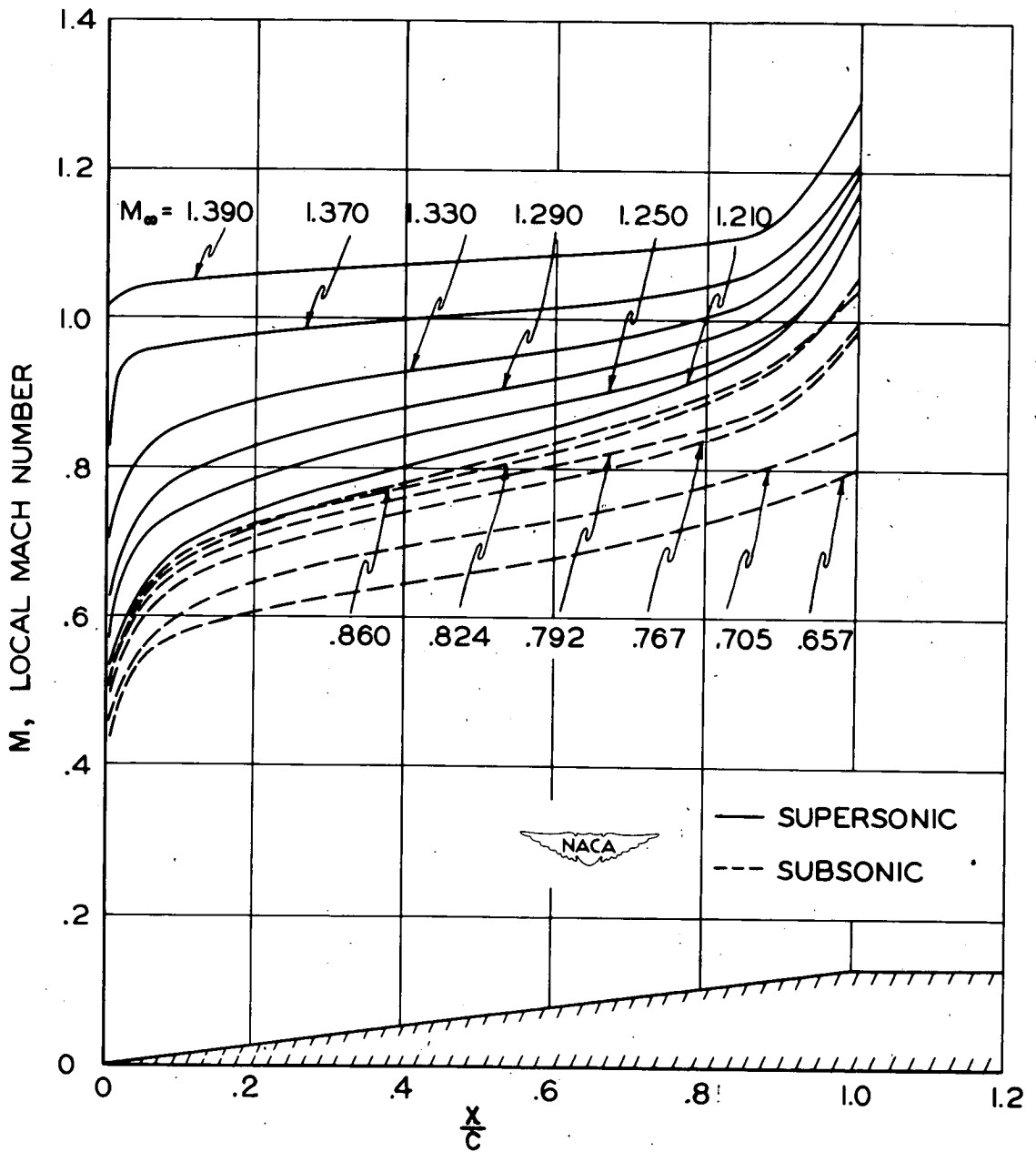


Figure 9.- Concluded.



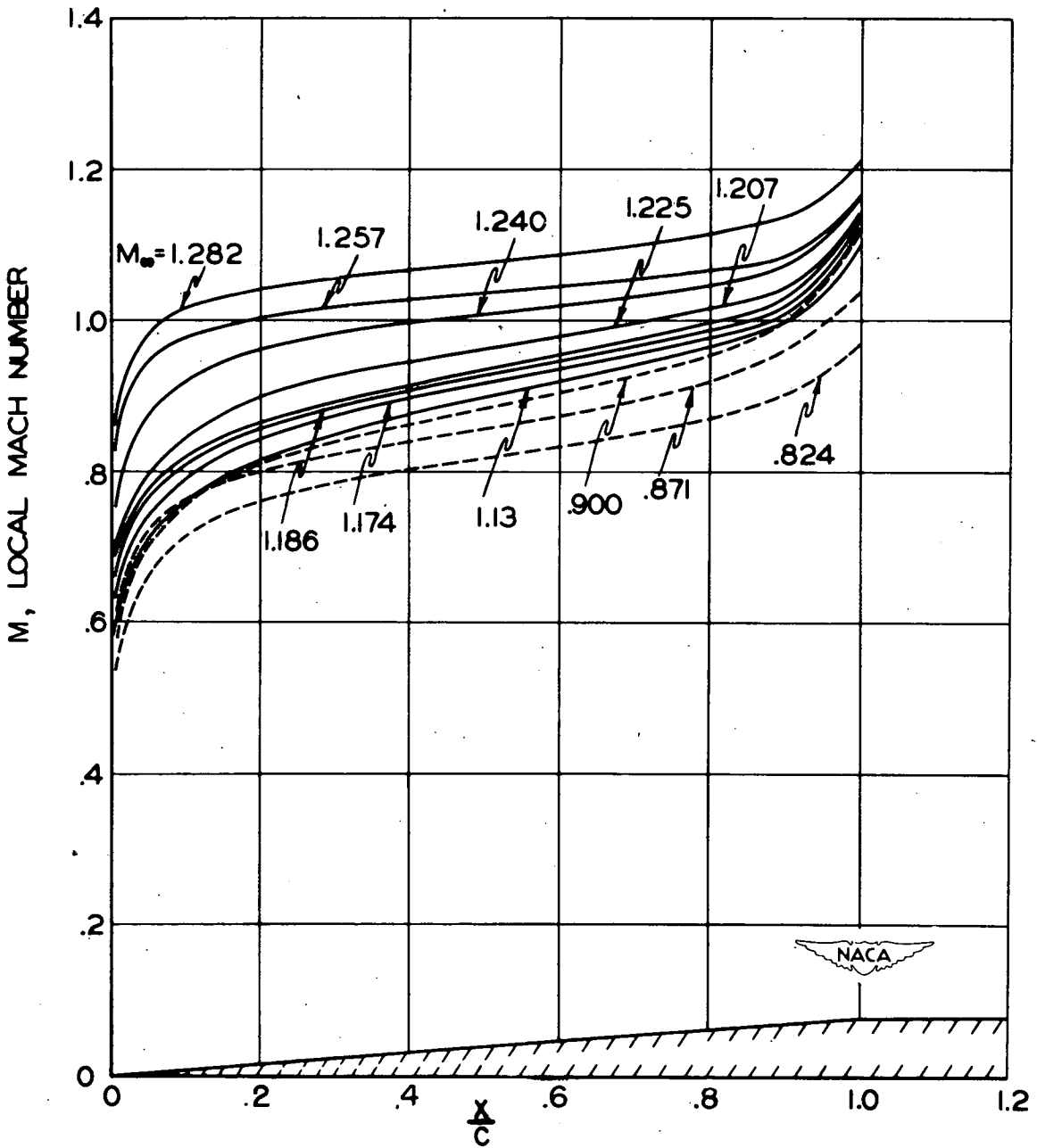
(a) 10° semiangle wedge.

Figure 10.- Local Mach number against x/c for increasing free-stream Mach number.



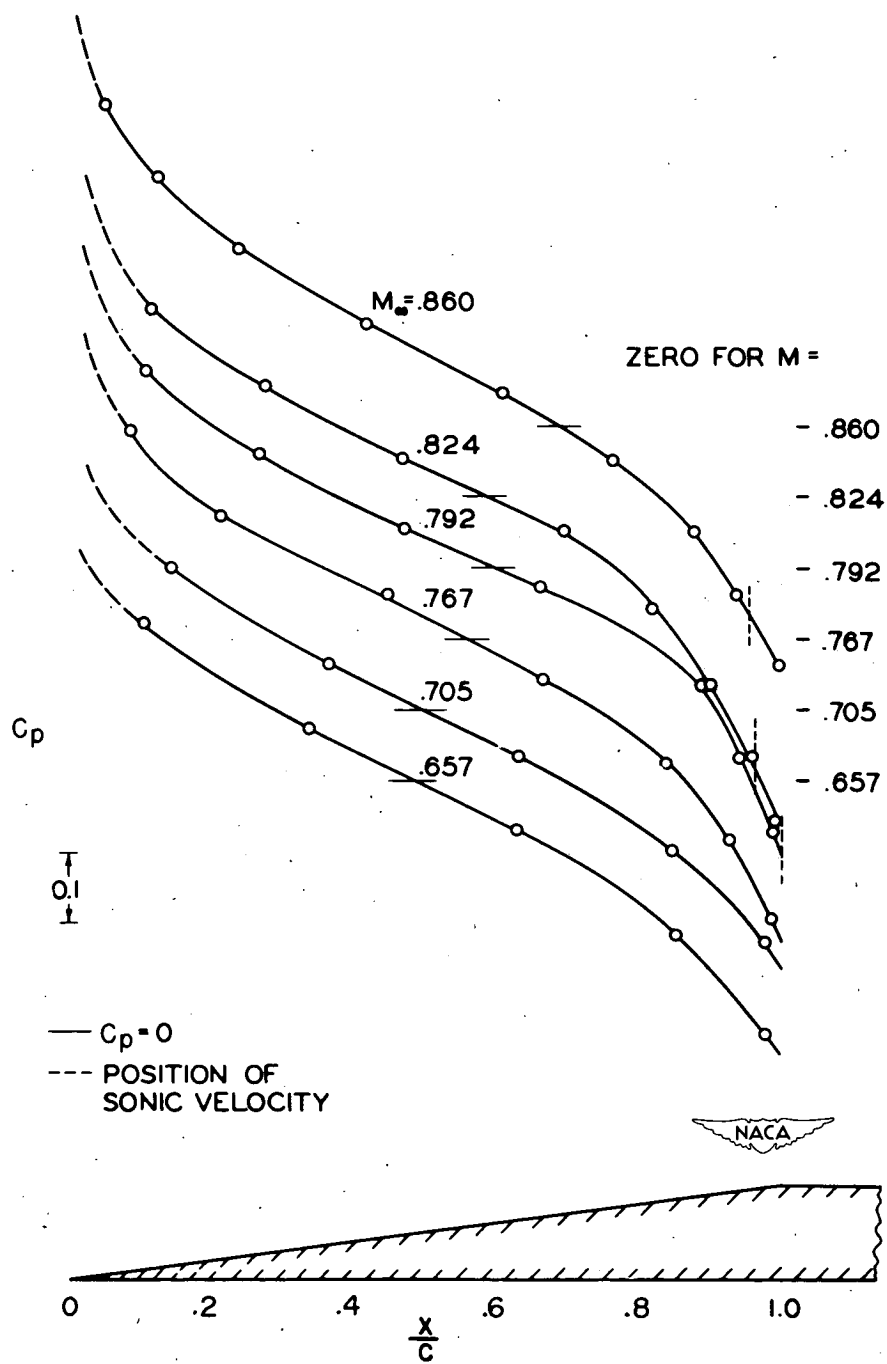
(b) $7\frac{1}{2}^\circ$ semiangle wedge.

Figure 10.- Continued.



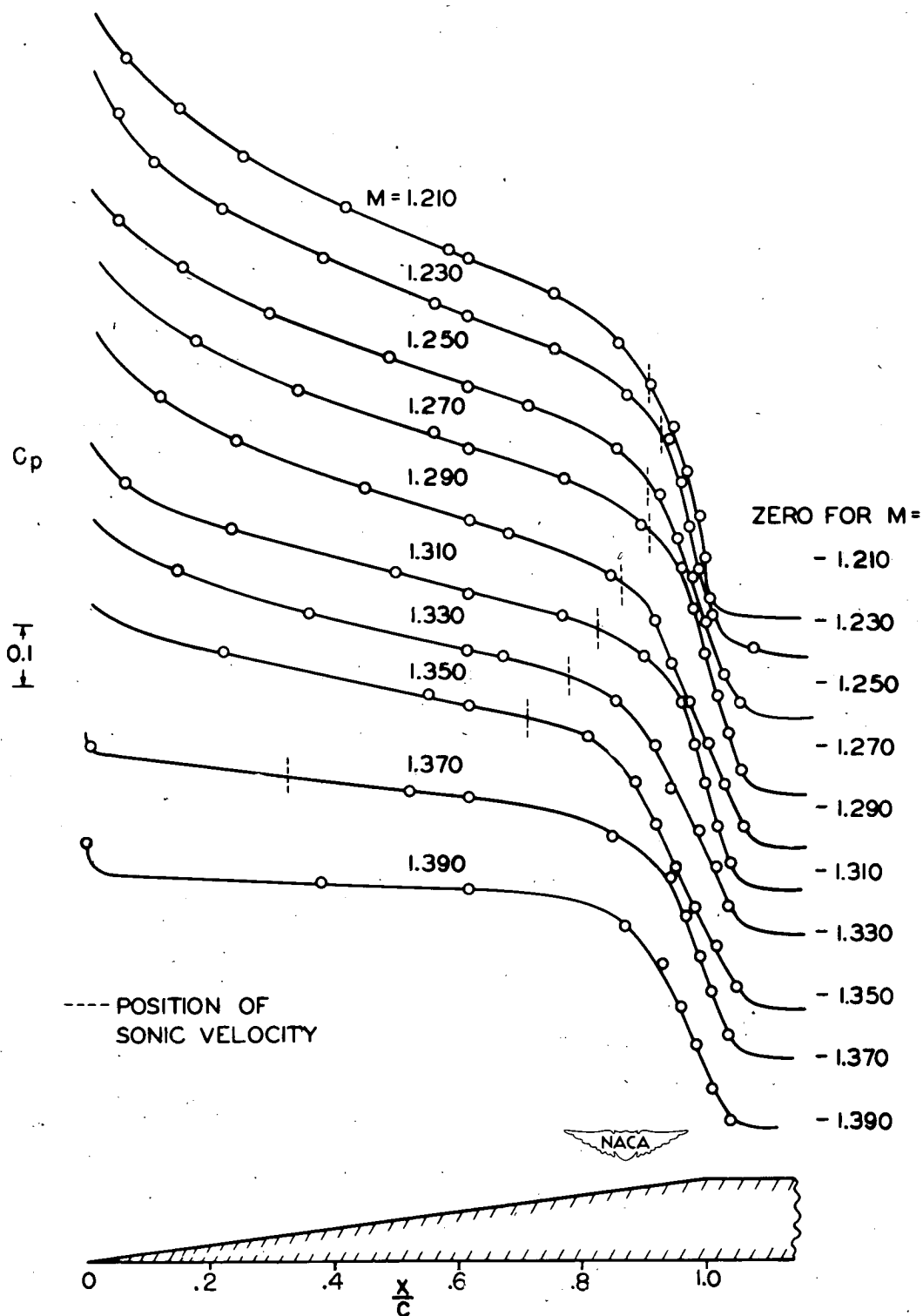
(c) $1/2^\circ$ semiangle wedge.

Figure 10.- Concluded.



(a) Subsonic.

Figure 11.- Pressure distributions for $7\frac{1}{2}^{\circ}$ semiangle wedge.



(b) Supersonic.

Figure 11.- Concluded.

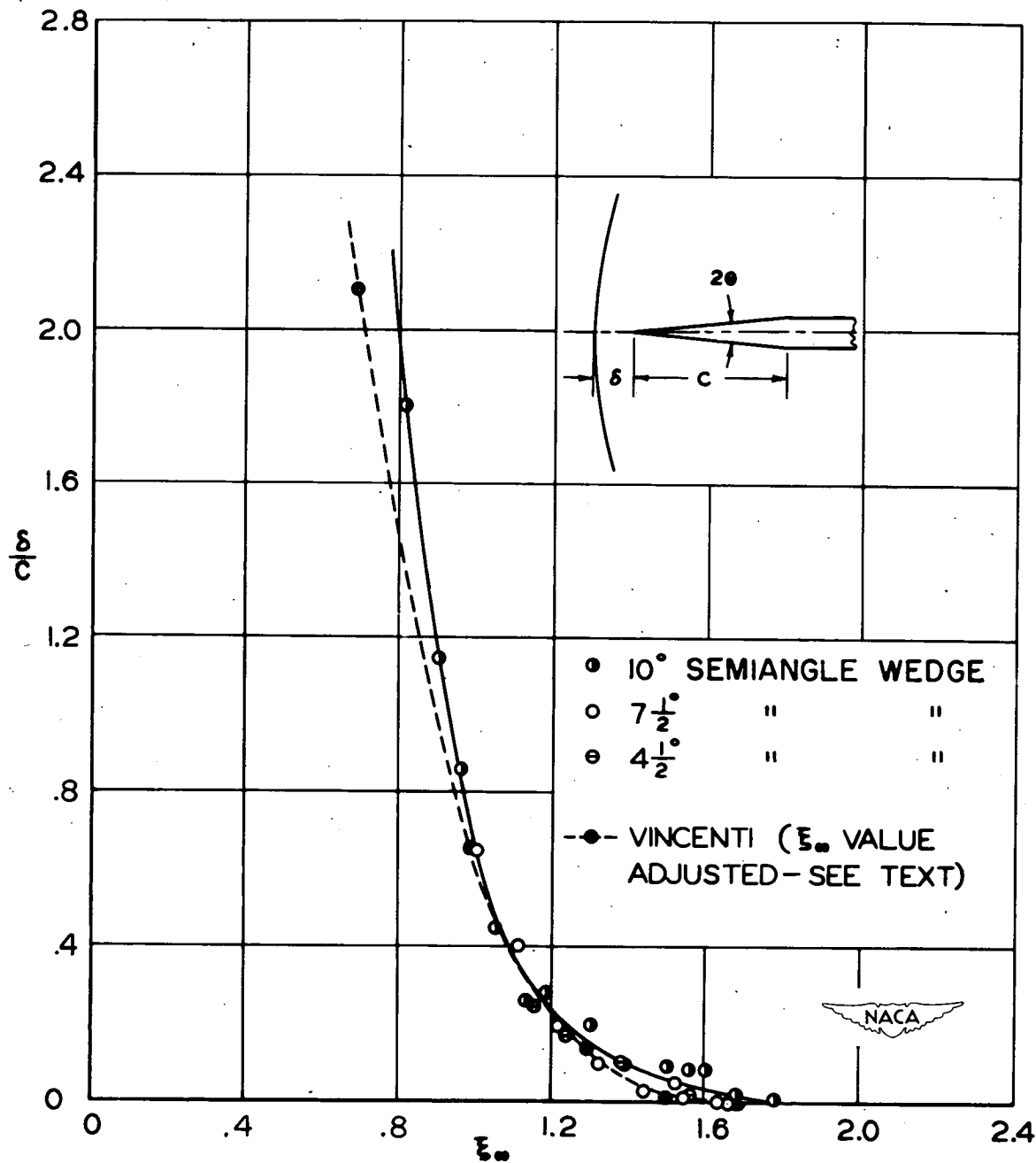


Figure 12.- Shock-detachment distance against reduced Mach number for a wedge.

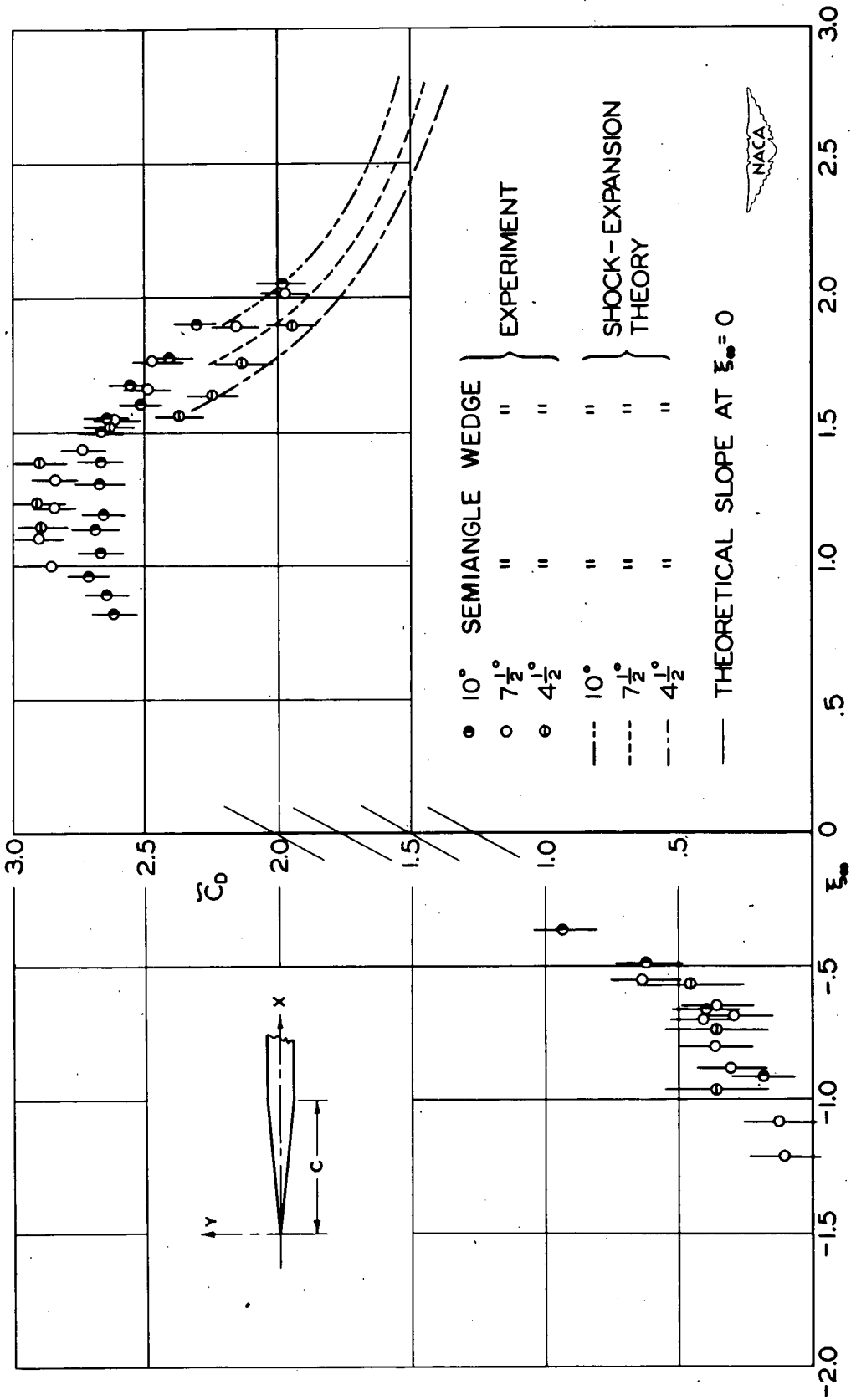


Figure 13.- Experimental reduced drag coefficient against reduced Mach number on a wedge.

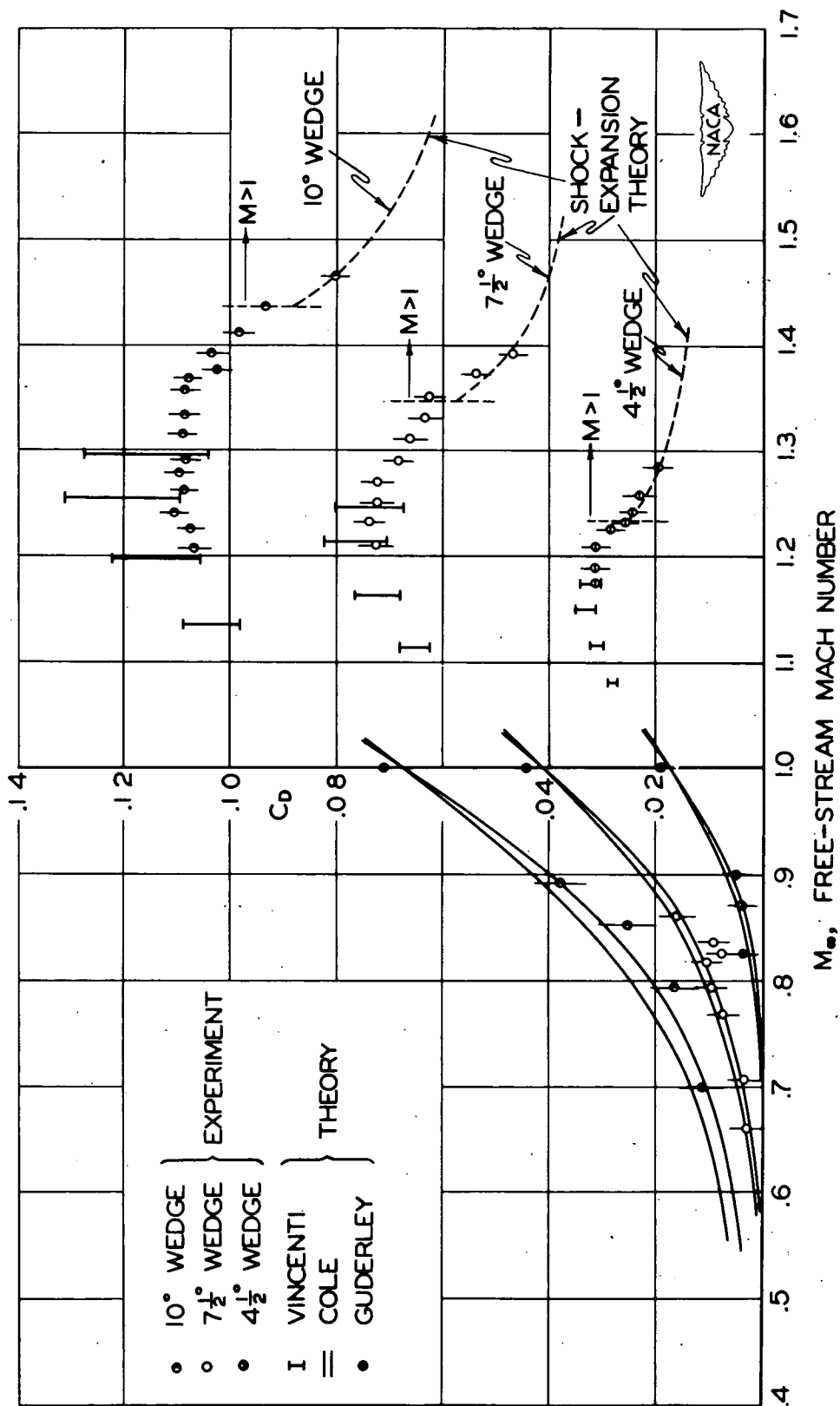


Figure 14.- Drag coefficient against Mach number for 10° , $7\frac{1}{2}^\circ$, and $4\frac{1}{2}^\circ$ semiangle wedges. Comparison of theory with experiment.

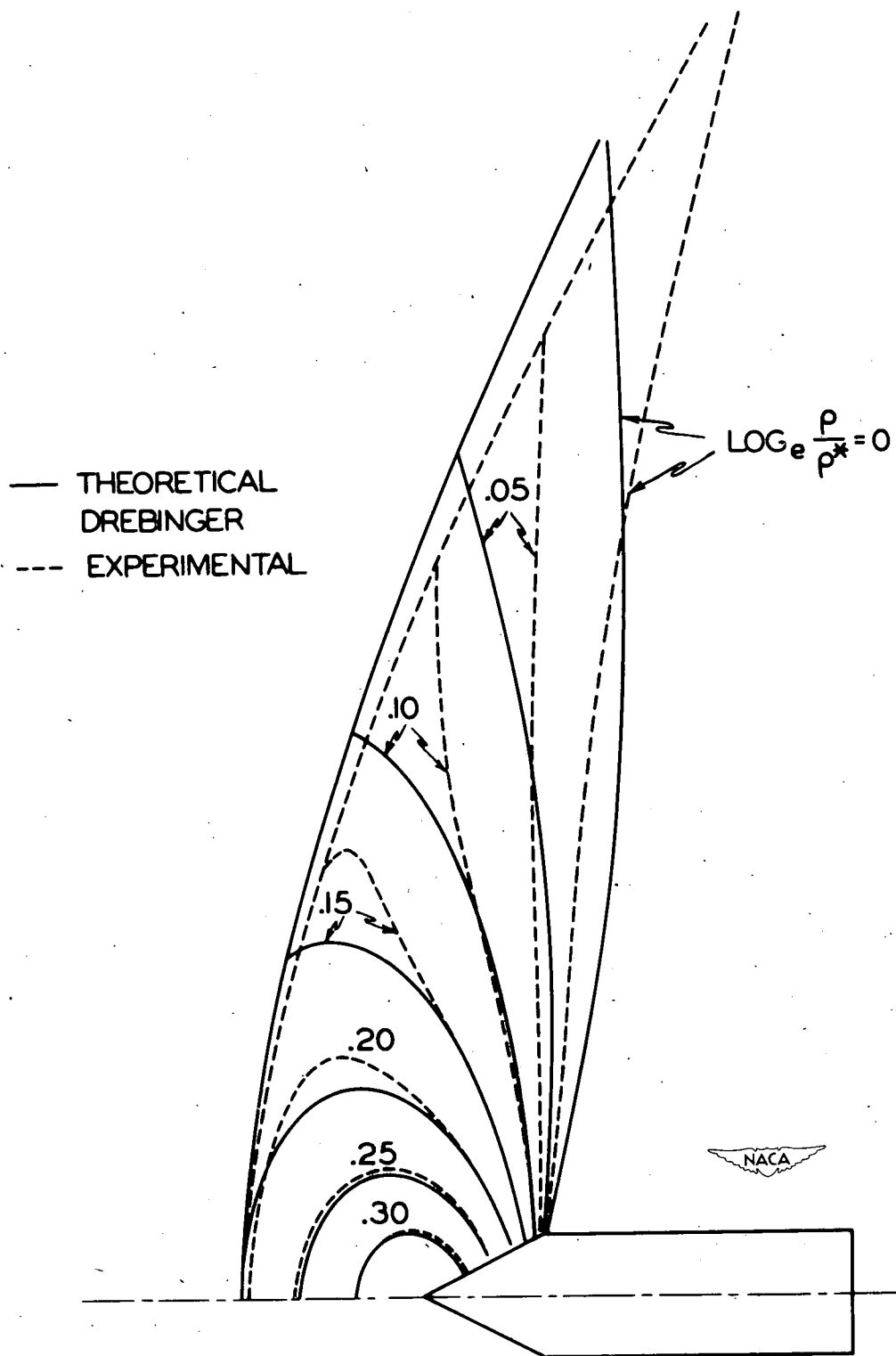


Figure 15.- Constant Mach number contours for 26.6° semiangle wedge at $M_\infty = 1.440$.

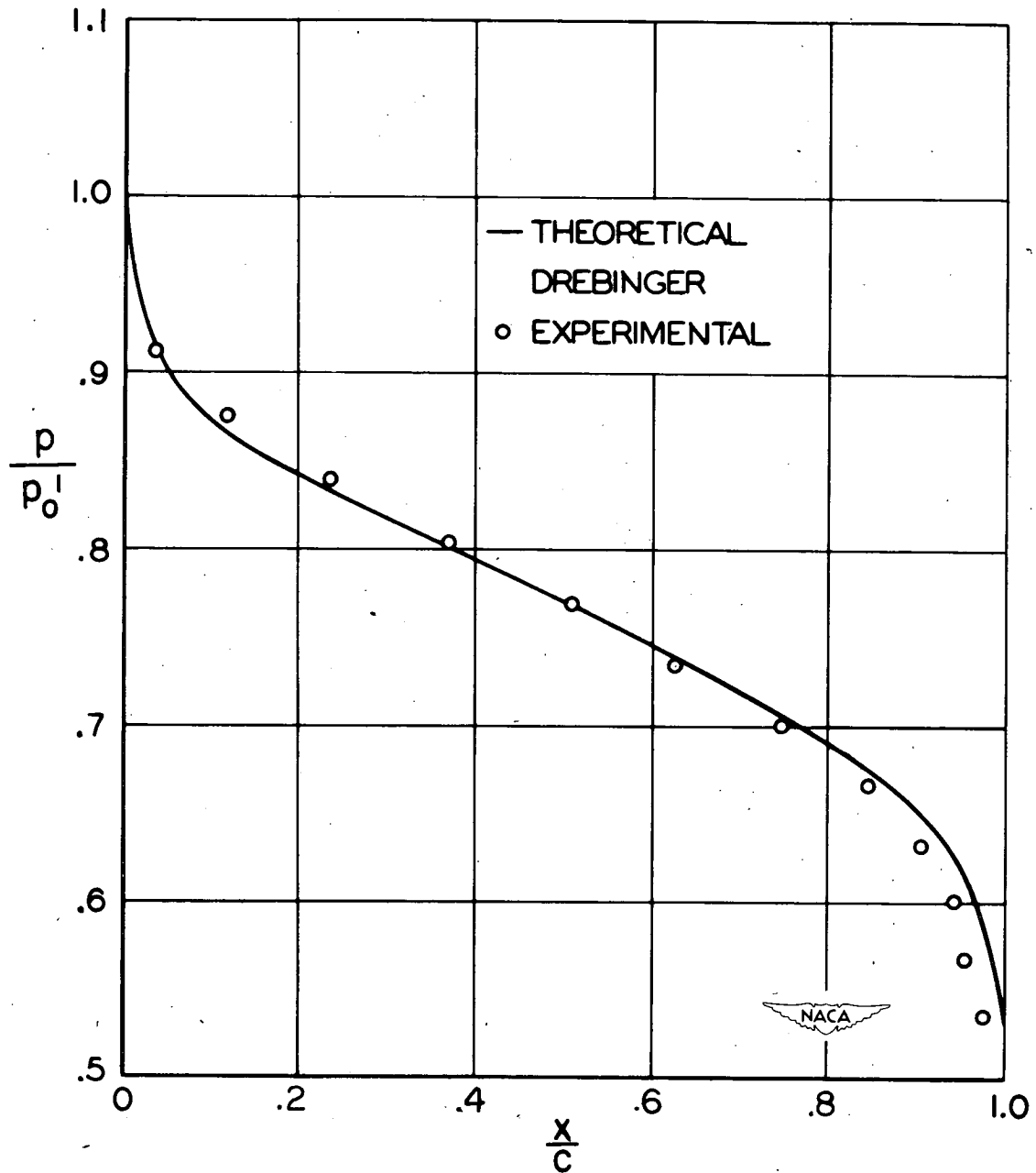


Figure 16.- Pressure distribution on a 26.6° semiangle wedge at $M_\infty = 1.440$.

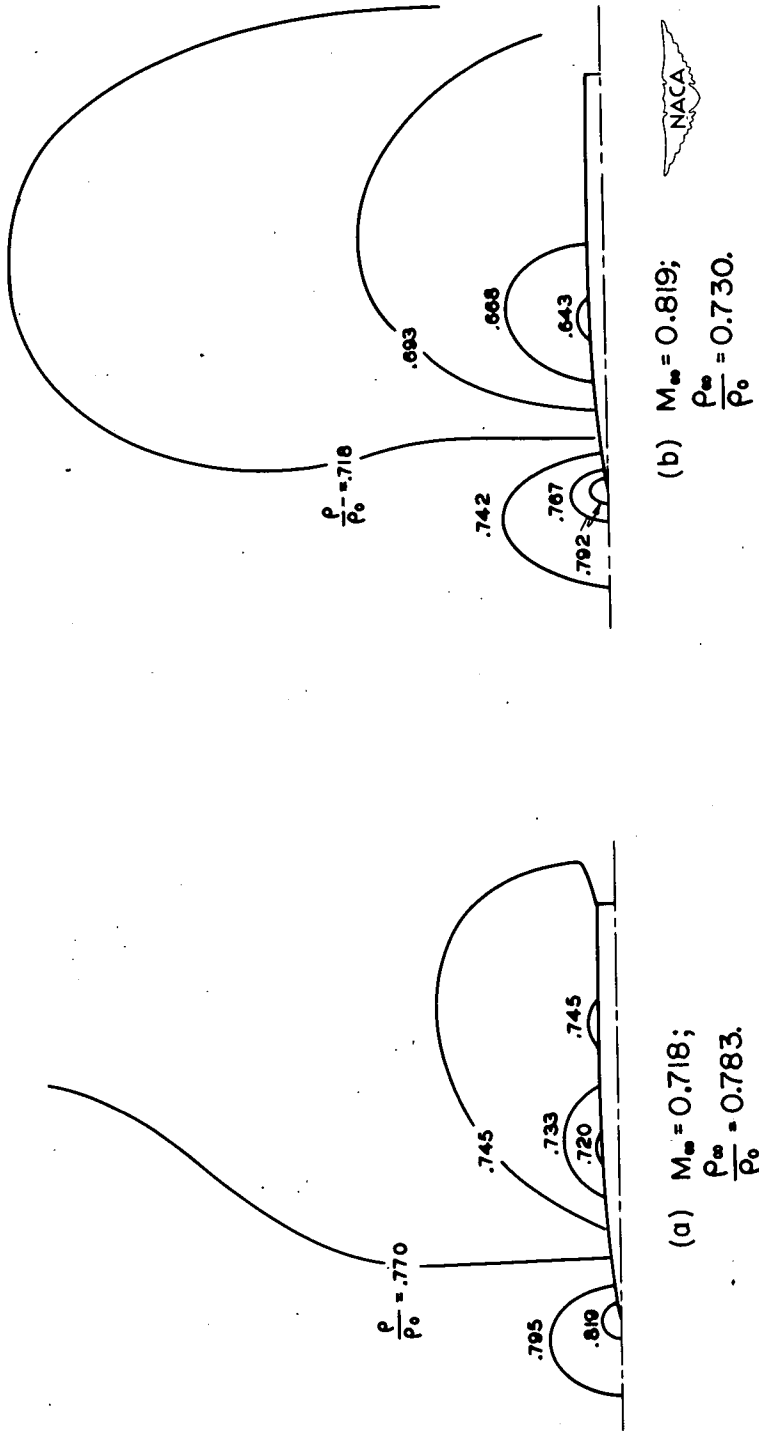


Figure 17.- Interferograms of flow past 8.8-percent circular-arc section for various Mach numbers.

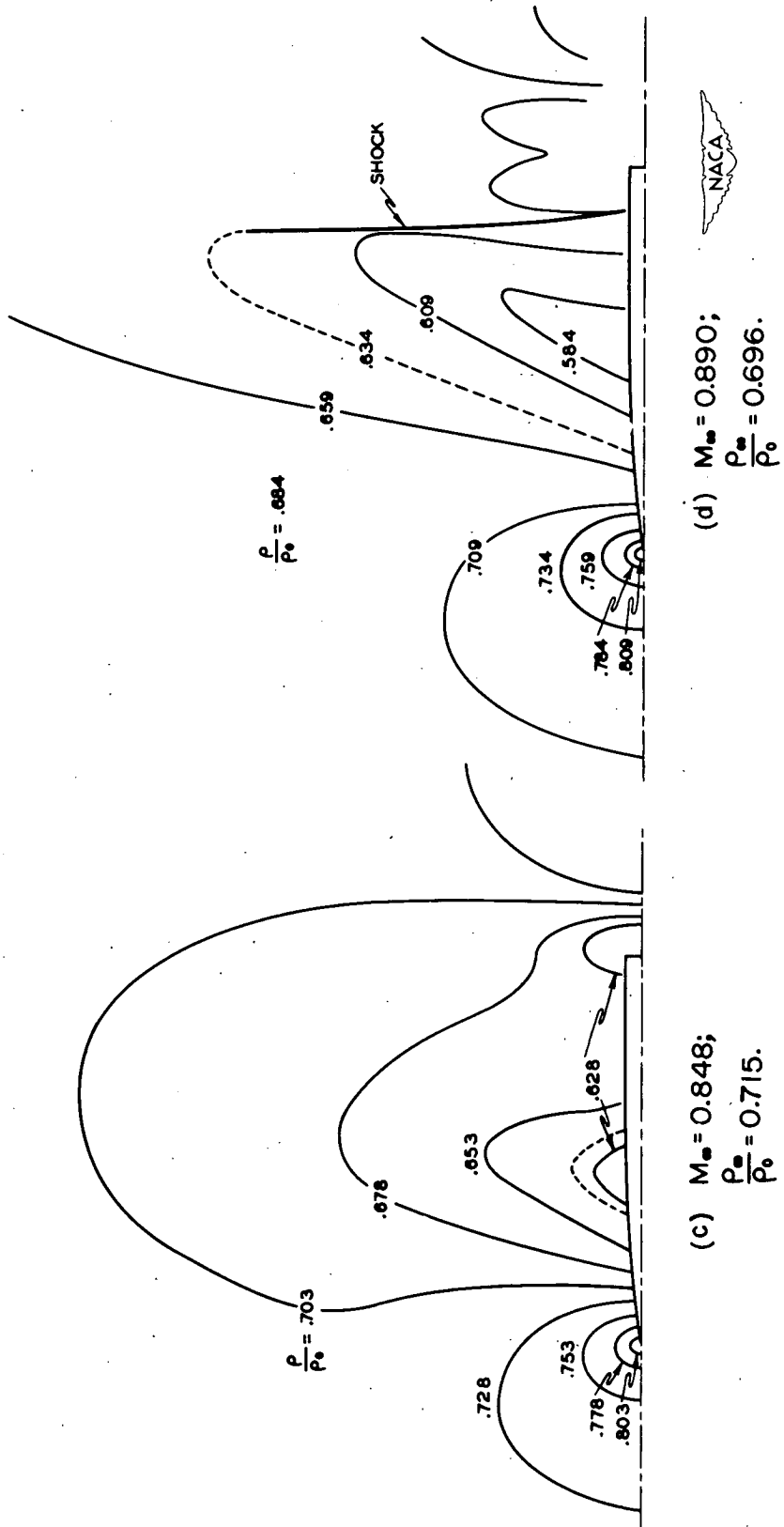


Figure 17.- Continued.

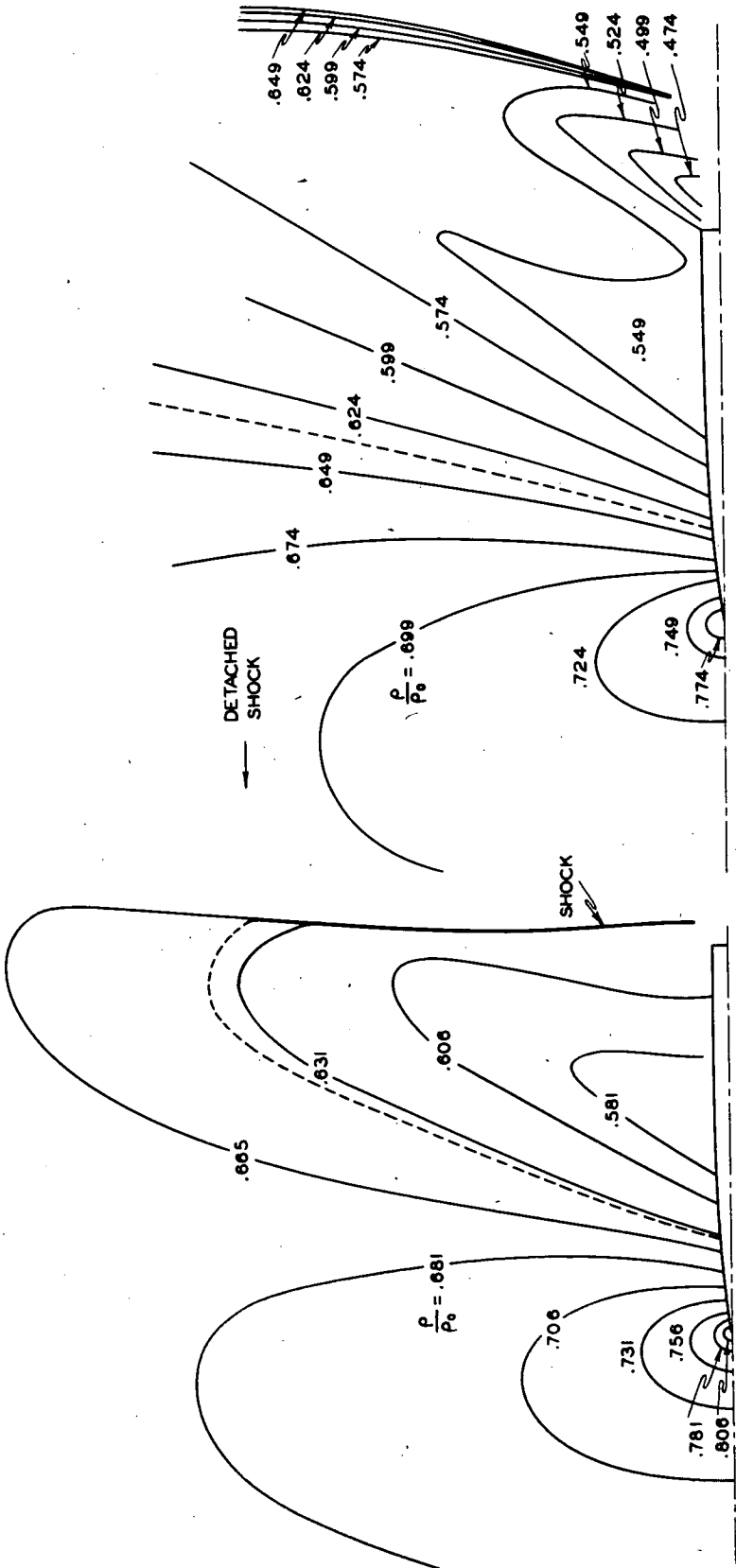


Figure 17.- Continued.

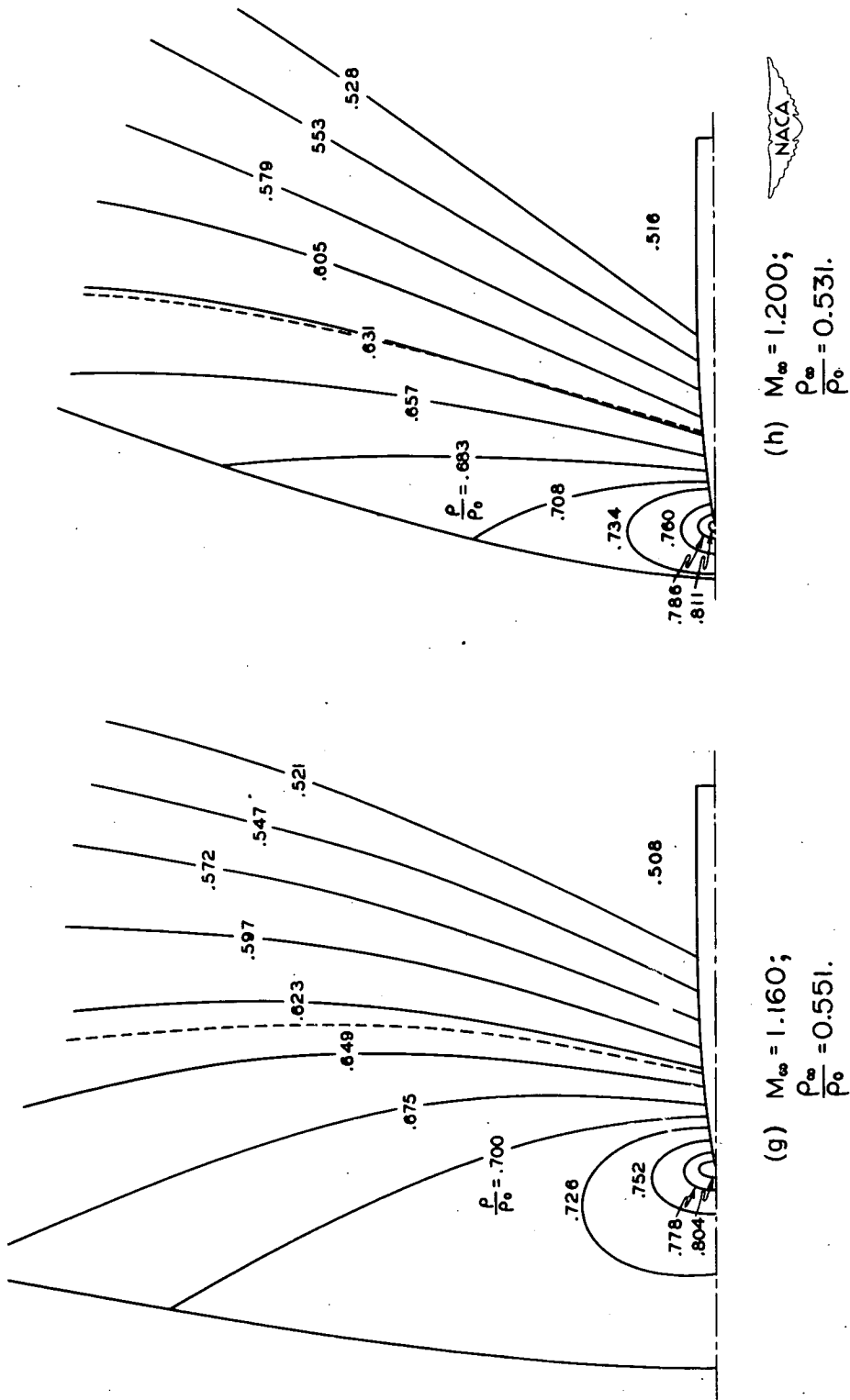


Figure 17.- Continued.

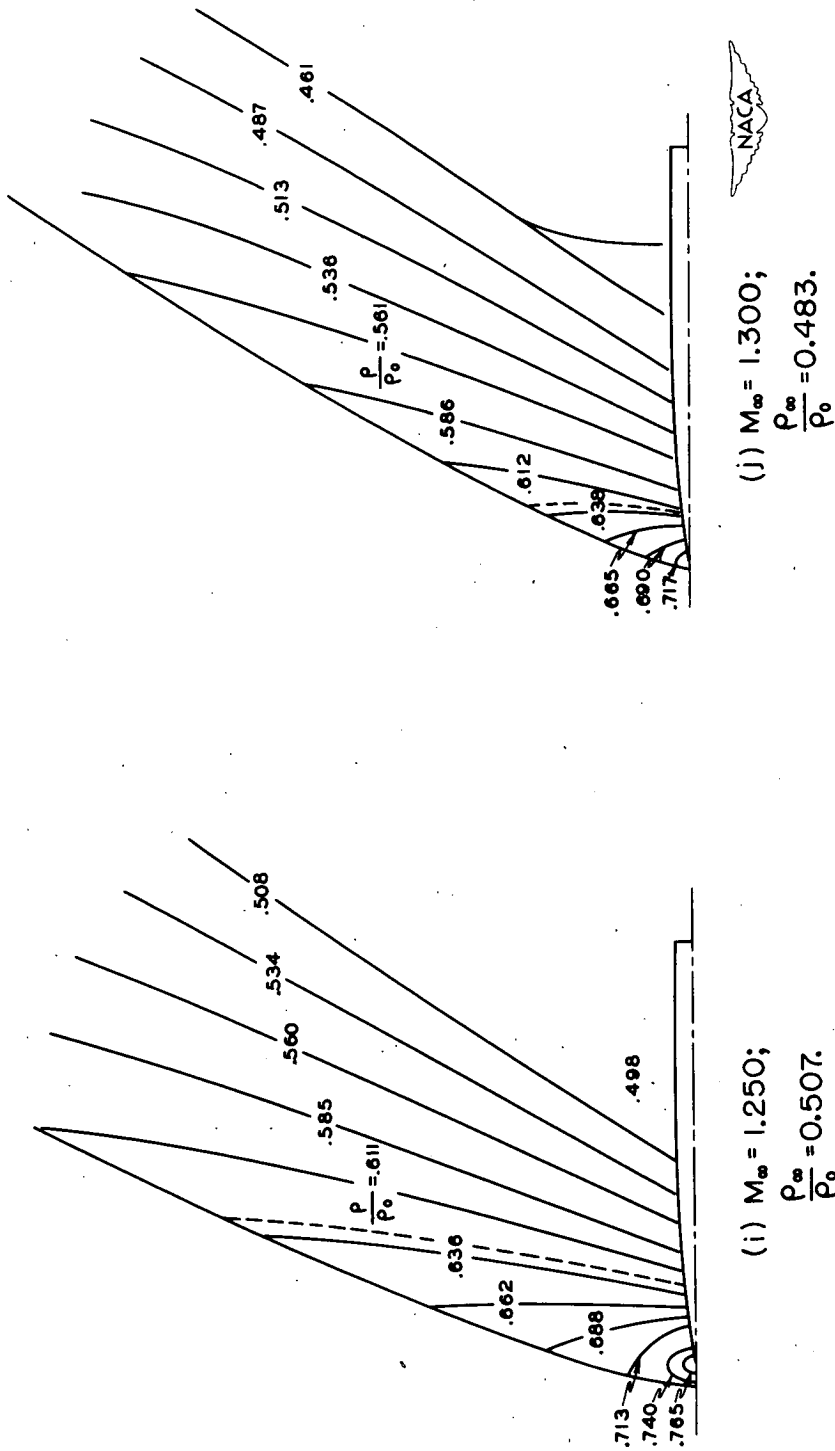


Figure 17.- Continued.

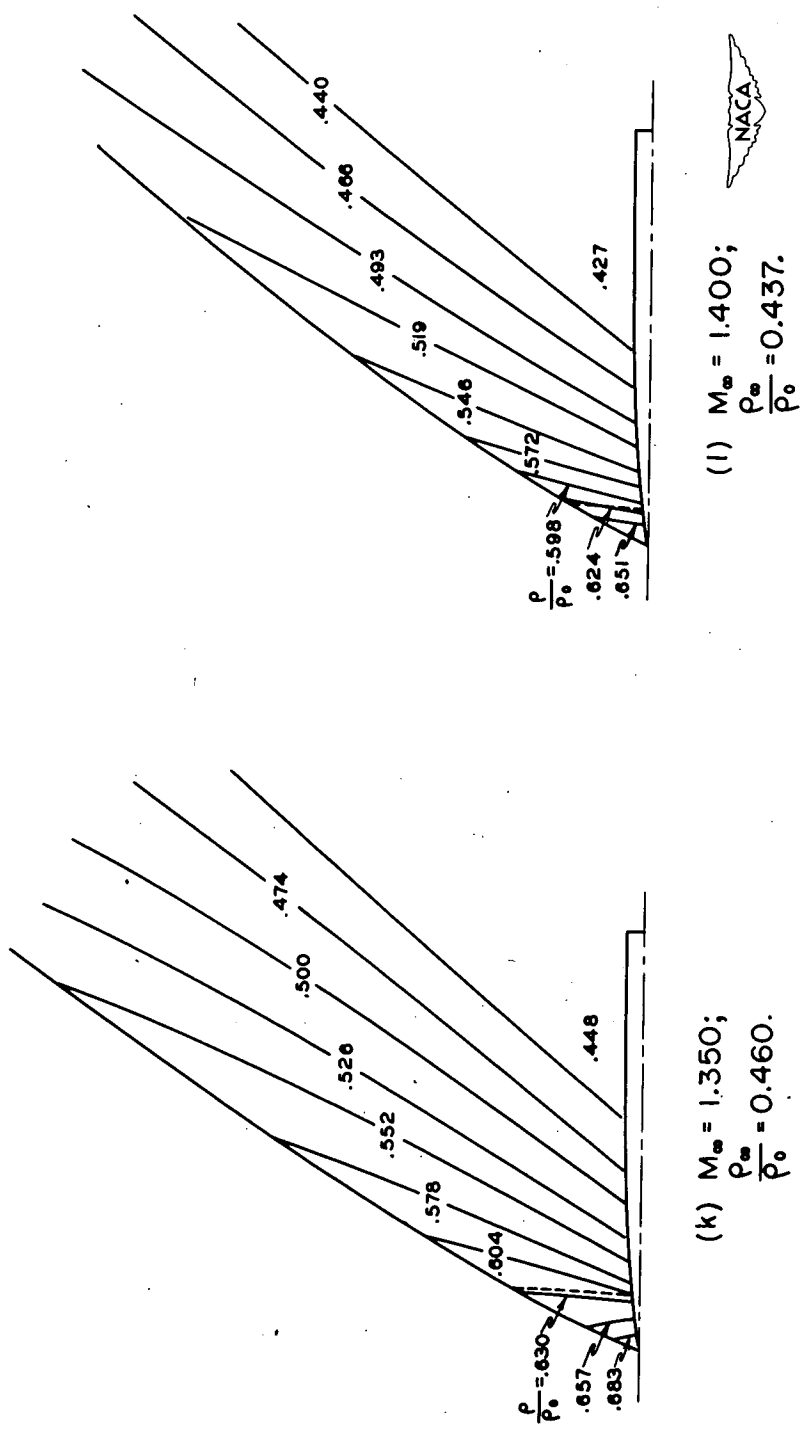


Figure 17.- Continued.

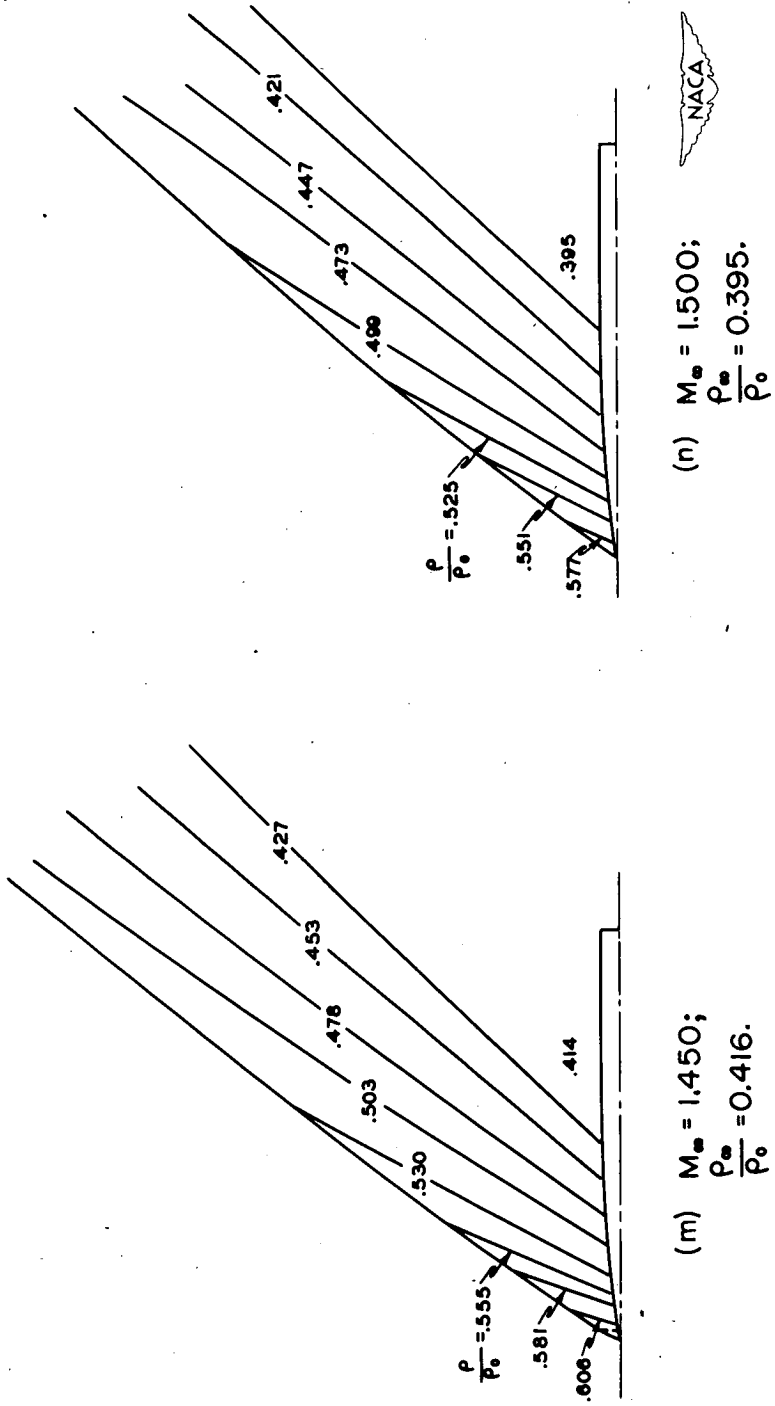


Figure 17.- Concluded.

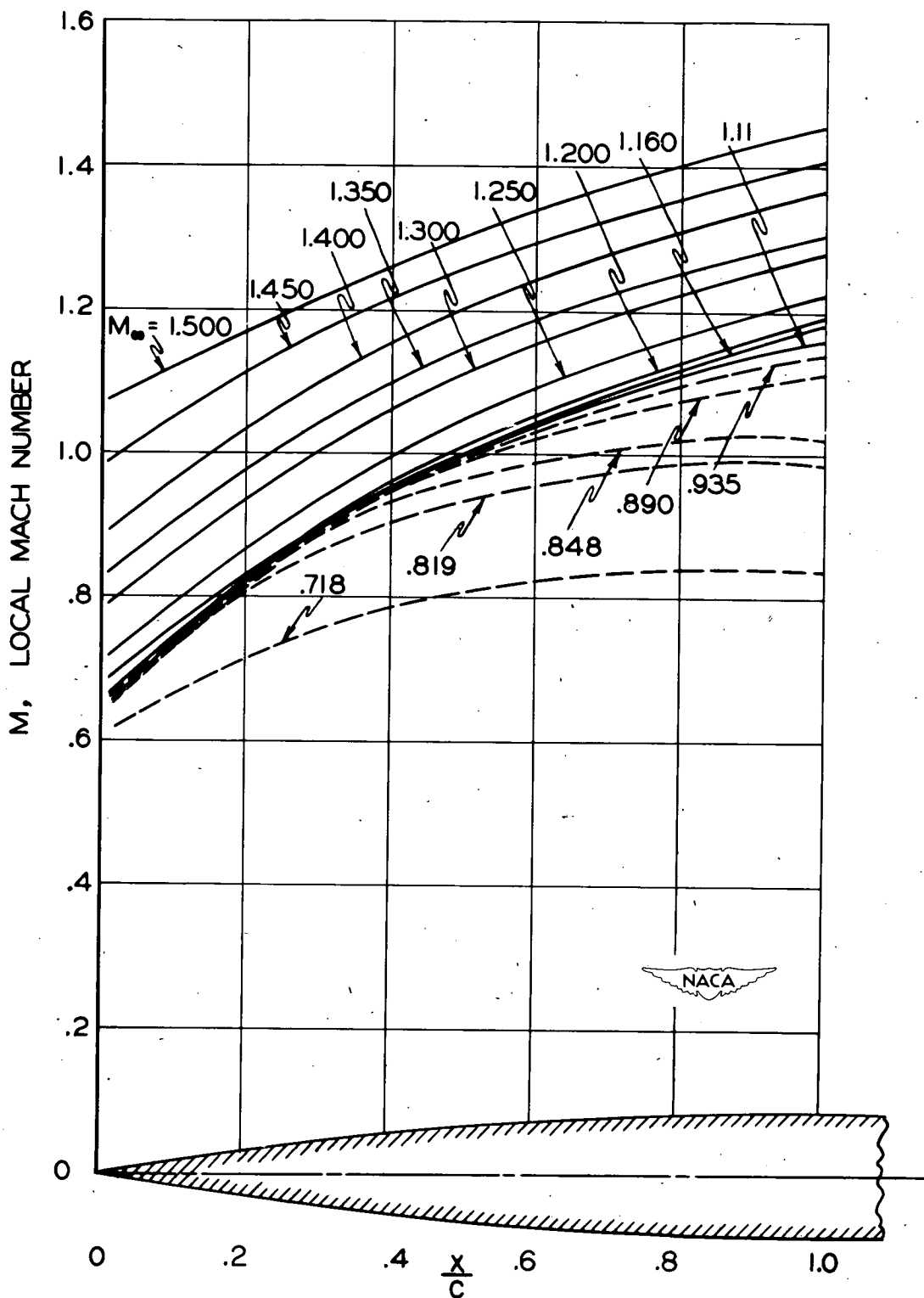


Figure 18.- Local Mach number against x/c for increasing free-stream Mach number. 8.8-percent circular-arc section.

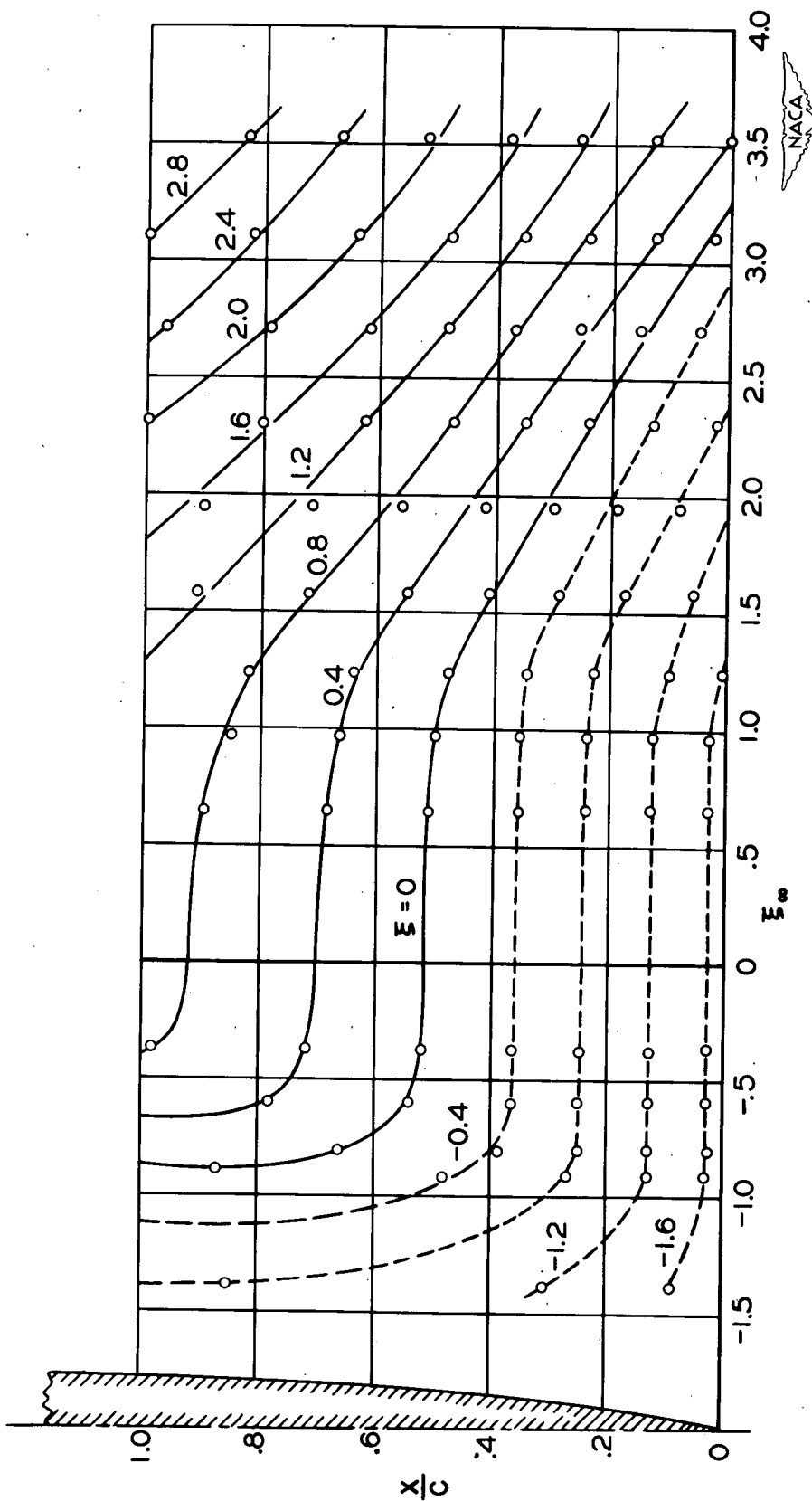
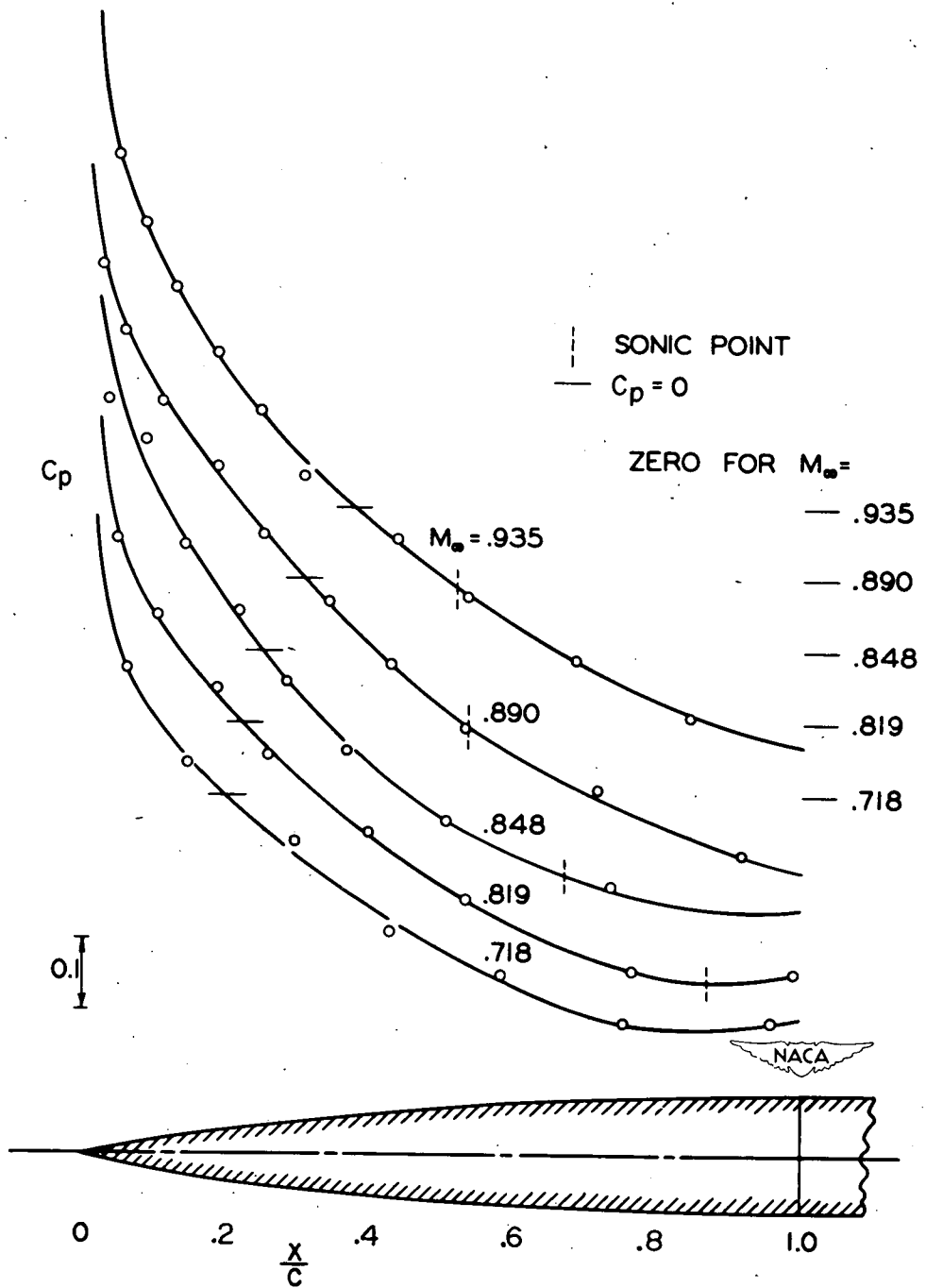
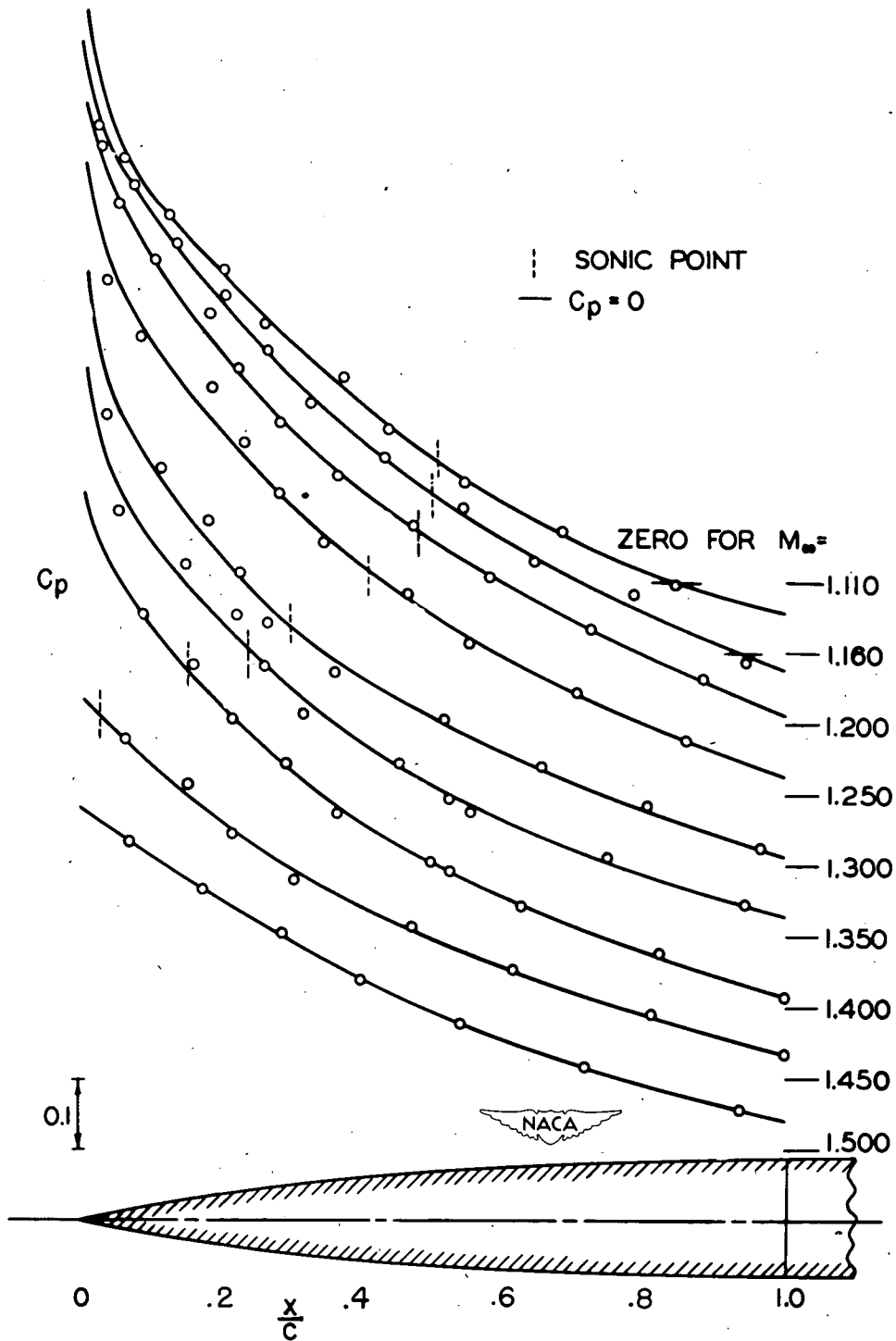


Figure 19.- Variation of reduced local Mach number distributions with reduced free-stream Mach number. 8.8-percent circular-arc section.



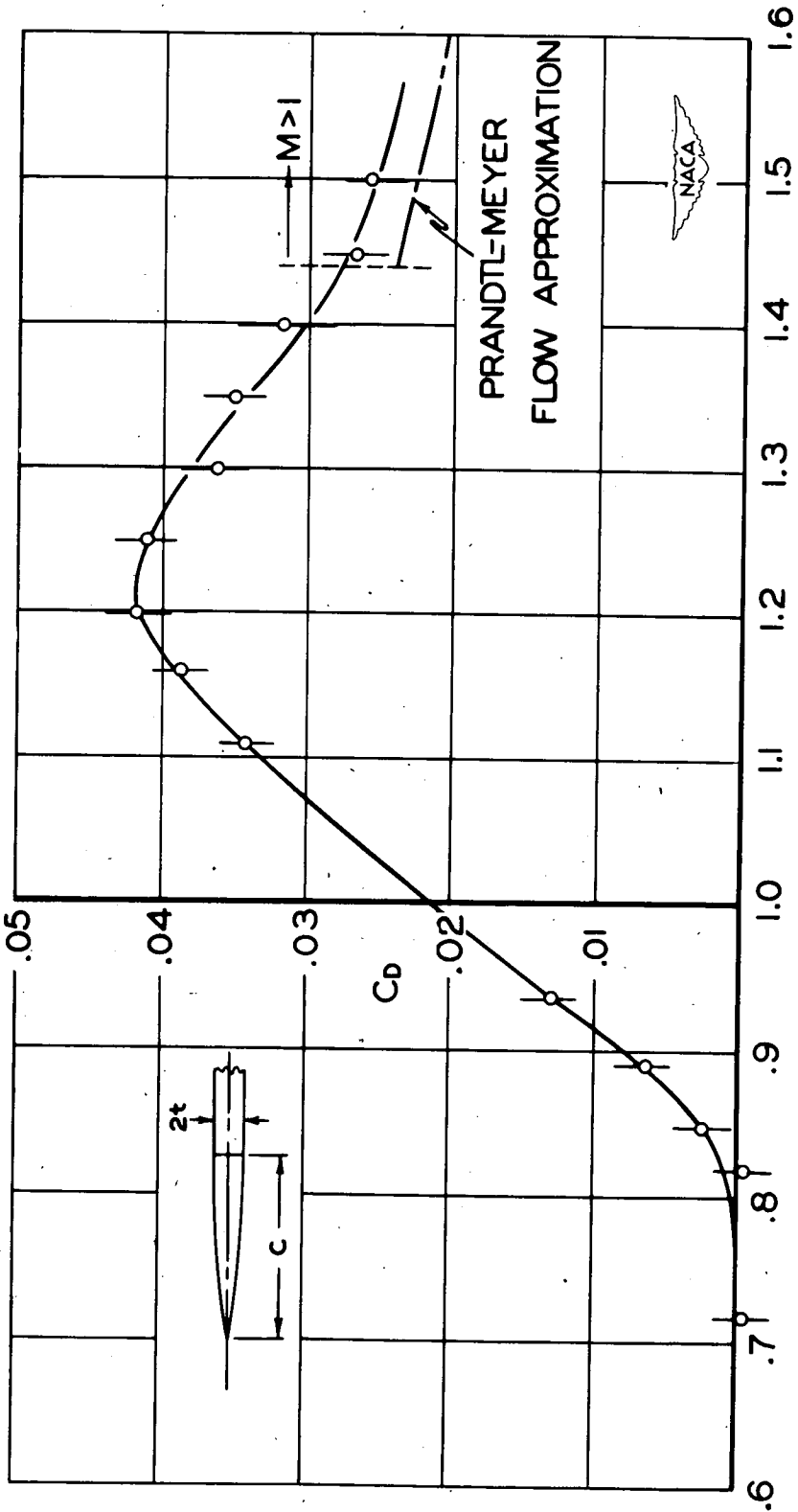
(a) Subsonic.

Figure 20.- Pressure distributions on an 8.8-percent circular-arc section.



(b) Supersonic.

Figure 20.- Concluded.



M_∞ , FREE-STREAM MACH NUMBER

Figure 21.- Drag coefficient against Mach number for 8.8-percent circular-arc section.

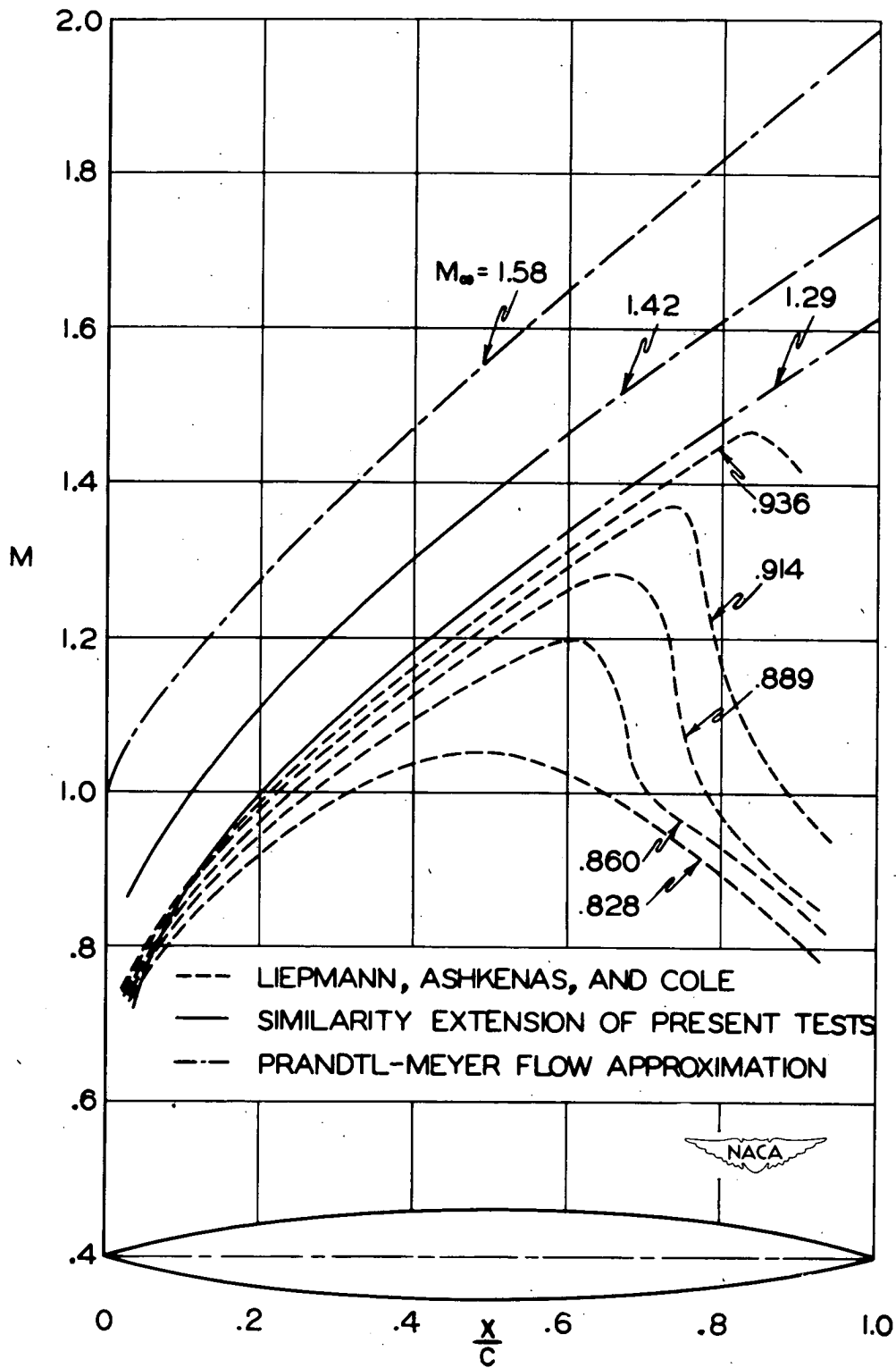


Figure 22.- Local Mach number against x/c for increasing free-stream Mach number. 12-percent biconvex circular-arc airfoil.

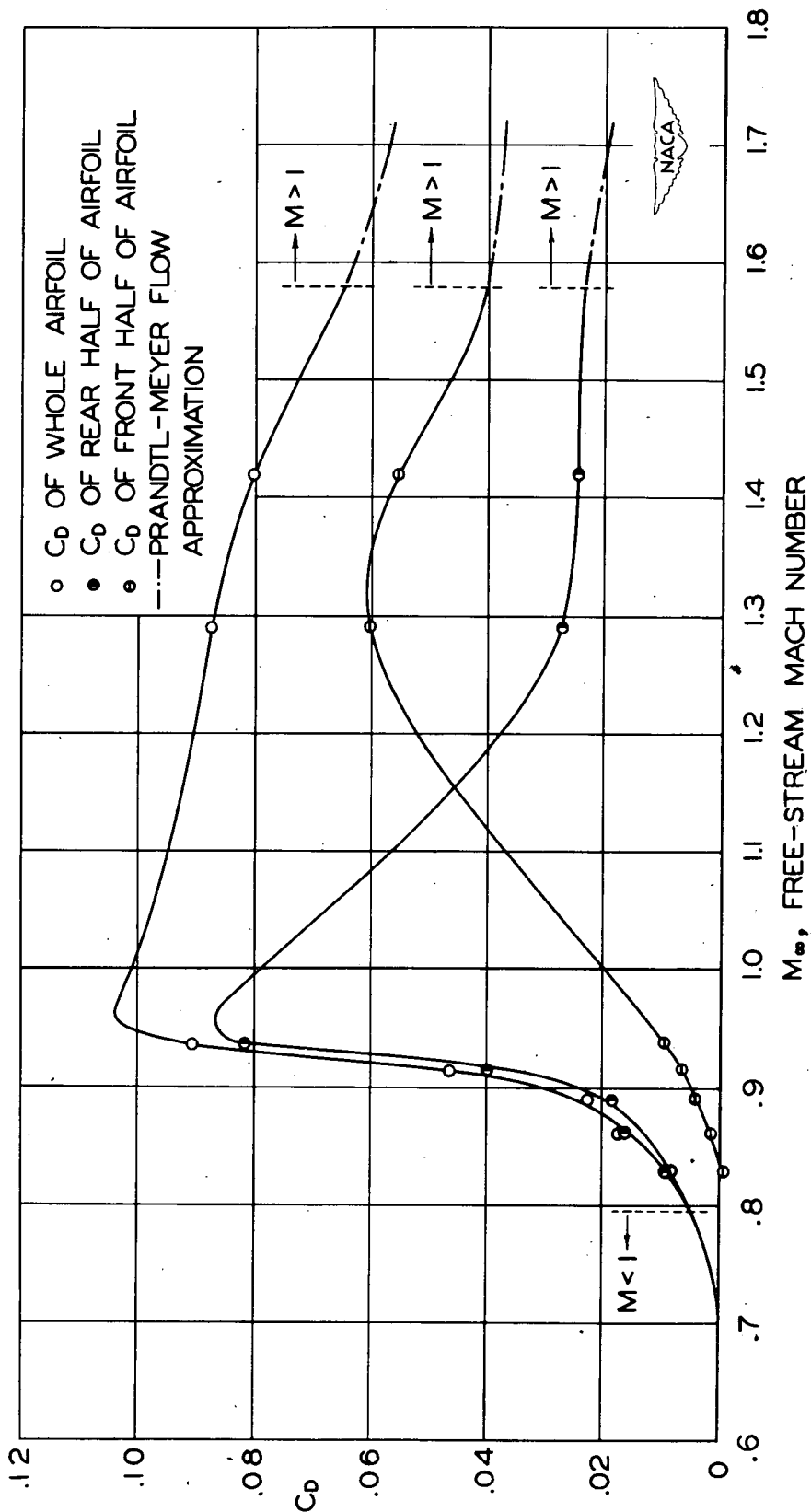


Figure 23.- Drag coefficient against Mach number for 12-percent biconvex circular-arc airfoil. (From data of fig. 22 on basis of constant Mach number distribution from $M_\infty = 0.96$ to 1.20.)